STUDY OF INTERACTIONS BETWEEN DIFFUSION BARRIER LAYERS AND LOW-K DIELECTRIC MATERIALS FOR COPPER/LOW-K INTEGRATION

Jinhong Tong, B.E., M.E.

Dissertation Prepared for the Degree of

DOCTOR OF PHILOSOPHY

UNIVERSITY OF NORTH TEXAS

December 2003

APPROVED:

Jeffry A. Kelber, Major Professor
Paul S. Braterman, Committee Member
Paul Marshall, Committee Member
Teresa D. Golden, Committee Member
Ruthanne D. Thomas, Chair of the Department of Chemistry
Sandra L. Terrell, Interim Dean of the Robert B. Toulouse School of Graduate Studies

Tong, Jinhong, *Study of Interactions Between Diffusion Barrier Layers and Low-κ Dielectric Materials for Copper/Low-κ Integration.* Doctor of Philosophy (Analytical Chemistry), December 2003, 105 pp., 8 tables, 49 illustrations, reference list, 98 titles.

The shift to the Cu/low-κ interconnect scheme requires the development of diffusion barrier/adhesion promoter materials that provide excellent performance in preventing the diffusion and intermixing of Cu into the adjacent dielectrics. The integration of Cu with low-κ materials may decrease RC delays in signal propagation but pose additional problems because such materials are often porous and contain significant amounts of carbon. Therefore barrier metal diffusion into the dielectric and the formation of interfacial carbides and oxides are of significant concern. The objective of the present research is to investigate the fundamental surface interactions between diffusion barriers and various low-κ dielectric materials. Two major diffusion barriers— tatalum (Ta) and titanium nitride (TiN) are prepared by DC magnetron sputtering and metal-organic chemical vapor deposition (MOCVD), respectively. Surface analytical techniques, such as X-ray photoelectronic spectroscopy (XPS), transmission electron microscopy (TEM), and atomic force microscopy (AFM) are employed.

Ta sputter-deposited onto a Si-O-C low dielectric constant substrate forms a reaction layer composed of Ta oxide and TaC. The composition of the reaction layer varies with deposition rate (1 Å-min^{-1} vs. 2 Å-sec^{-1}), but in both cases, the thickness of the TaC layer is found to be at least 30 Å on the basis of XPS spectra, which is corroborated with cross-sectional TEM data. Sputter-deposited Cu will not wet the TaC layer and displays facile agglomeration, even at 400 K. Deposition for longer time at 2 Å-sec^{-1} results in formation of a metallic Ta layer. Sputter deposited Cu wets (grows conformally) on the metallic Ta surface at 300 K, and resists

significant agglomeration at up to ~ 600 K. Cu diffusion into the substrate is not observed up to 800 K in the UHV environment.

Tetrakis(diethylamido) titanium (TDEAT) interactions with SiO_2, Cu and a variety of low-κ samples in the presence (~ 10^{-7} Torr or co-adsorbed) and absence of NH_3 result in different products. TDEAT interactions with SiO_2 are dominated by Ti interactions with substrate oxygen sites, and that Ti oxide/sub-oxide bond formation can proceed with relatively low activation energy. No Ti carbide or Si carbide formation is observed. Co-adsorption of TDEAT and NH_3 on SiO_2 at 120K followed by annealing to higher temperature results in enhanced Ti-N bond formation, which is stable against oxidation up to 900K in UHV. Similarly, continuous exposures of TDEAT on SiO_2 at 500K in the presence of NH_3 exhibit a relatively enhanced Ti-N spectral component. Co-adsorption of NH_3 and TDEAT on Cu (poly) surface at 120K, followed by annealing to 500K, results in complete desorption of Ti, N or C-containing species from the Cu substrate. Reaction of TDEAT with a Cu surface at 500K yields a Ti-alkyl species via a β-hydride elimination pathway. TDEAT/Cu interactions are not observably affected by overpressures of NH_3 of 10^{-7} Torr. TDEAT interaction with a porous carbon doped oxide low-κ substrate at 700K demonstrates undissociated or partly dissociated Ti-NR species trapped in the dielectrics matrix due to its high porosity. In addition, carbide formation is observed from C(1s) XPS spectra. For a hydrocarbon low-κ film, the majority sites (carbon) are highly unreactive towards TDEAT even at higher temperature due to a lack of functional groups to initiate the TDEAT/low-κ surface chemistry.

ACKNOWLEDGMENTS

The author wishes to express her special gratitude to her academic advisor, Professor Jeff Kelber, for his kind guidance and careful instruction. Her appreciation also extends to Dr. Paul S. Braterman, Dr. Paul Marshall, Dr. Teresa D. Golden and Dr. Toh-Ming Lu (Rensselaer Polytechnic Institute) who have served on her doctoral committee. The author appreciates Dr. Moon Kim (Material Science Department) for the TEM data and for enlightening discussions. The author is grateful to her lab-mates at the Surface Science Laboratory of University of North Texas for their helpful assistance. Financial support from the Semiconductor Research Corporation (SRC) and International Sematech are highly acknowledged. Finally, the author would like to thank her husband and parents for their constant encouragement and support.

TABLE OF CONTENTS

LIST OF TABLES

LIST OF ILLUSTRATIONS

CHAPTER 1

INTRODUCTION

As the interconnect linewidths shrink continuously to deep submicron regimes, the rapid increase in resistance-capacitance (RC) delay time is becoming one of the major problems for microelectronic devices. To address these problems, new materials for use as metal lines and interlayer dielectrics (ILD) as well as alternative architectures have been proposed to replace the current Al-SiO_2 based interconnect technology. The transition to copper as the conductor and to a better dielectrics began with IBM's announcement in September 1997. Copper is an attractive substitute for aluminum due to its lower electrical resistivity (1.68 $\mu\Omega$·cm versus 2.66 $\mu\Omega$·cm for Al) and superior resistance to electromigration. Copper has the ability to significantly reduce the number of levels of metal required, while also increasing chip speed, minimizing power dissipation and reducing manufacturing costs. However, the implementation of copper is challenged by fast diffusion of copper into Si or SiO_2 and poor adhesion with these substrates. The presence of copper in silicon results in highly adverse effects, including the formation of deep trap levels that cause serious device degradation and failure. To eliminate the copper diffusion, a diffusion barrier/adhesion promoter material which has fewer grain boundaries, no reaction with copper, good adhesion to Si, SiO_2 and electrical stability in high temperature is needed. At the same time, much attention has been paid to using low-k (dielectric constant) materials instead of conventional SiO_2 to reduce interconnect capacitance and thus address the RC delay problems. Therefore, the possible interaction between diffusion barriers and low-k dielectric materials will be of technical importance, since it is associated with the integrity of the low-k materials, the adhesion and also the metal via poisoning issue in copper/low-k metallization schemes.

This study is intended to investigate the fundamental surface interactions between diffusion barriers and various low-*k* materials. Two major diffusion barrier materials---tantalum and titanium nitride are prepared by DC magnetron sputtering and metal-organic chemical vapor deposition (MOCVD), respectively. Surface analytical techniques, such as X-ray photoelectron spectroscopy (XPS), transmission electron microscopy (TEM), and atomic force microscopy (AFM) are employed. This dissertation consists of four chapters. The current chapter provides background information on the fundamental concepts of the interconnect integration, role of RC delay, diffusion barriers and introduction of low-*k* materials, as well as a review of surface analysis methods used in this research. Chapter 2 presents the studies on Ta metallization of a Si-O-C low-*k* material and Cu metallization of Ta/Si-O-C multilayers. Chapter 3 contains the study of MOCVD of tetrakis(diethylamido) titanium (TDEAT) interactions on SiO_2 and Cu substrates. In Chapter 4, TDEAT interactions with various low-*k* substrates (different carbon concentrations and topographies) are investigated to further understand the barrier films/low-*k* interactions and the strengths and weaknesses of the materials and their processibility.

1.1. THE ROLE OF RC DELAY

The effective measure of device performance or total circuit delay is a combination of the intrinsic gate delay and the interconnect delay (RC delay). As feature size is scaled down below 0.25 μm, the intrinsic gate delay decreases continuously with decreasing size of the transistors and the interconnect delay begins to dominate overall device delay limiting the overall chip performance (1) (shown in Fig.1.1).

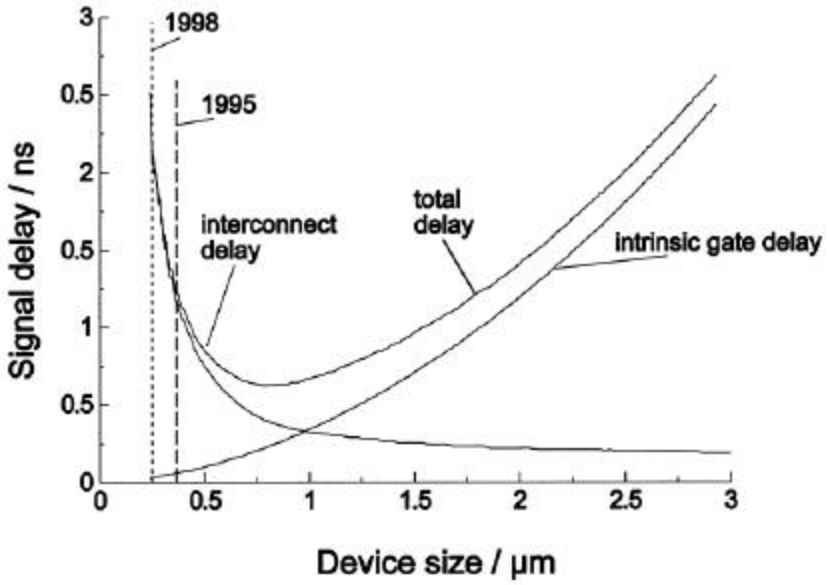

Fig.1.1 Dependence of signal delay time as a function of device size (2). (Reprinted with permission from Elsevier)

The time delay associated with the interconnection is dependent upon two factors: the resistance of the interconnections (metal), and the capacitance associated with the dielectric media. A simple first-order model can be used to estimate interconnect RC delay. Figure 1.2 shows a schematic diagram of a typical multilevel interconnect system (3). Assuming that the minimal pitch (P) equals twice the metal width (W), and assuming that the dielectric thickness above and below a metal line equals the thickness of the metal line (T), the following equation can be used to estimate the RC delay (4-6):

$$RC = 2\rho k\varepsilon_0 (4L^2/P^2 + L^2/T^2) \qquad (1\text{-}1)$$

where ρ is the resistivity of the conductor, k is dielectric constant of the interlevel material and ε_0 is permittivity of free space respectively, L, T are the length and thickness of the conductor, P is the distance between two conducting lines.

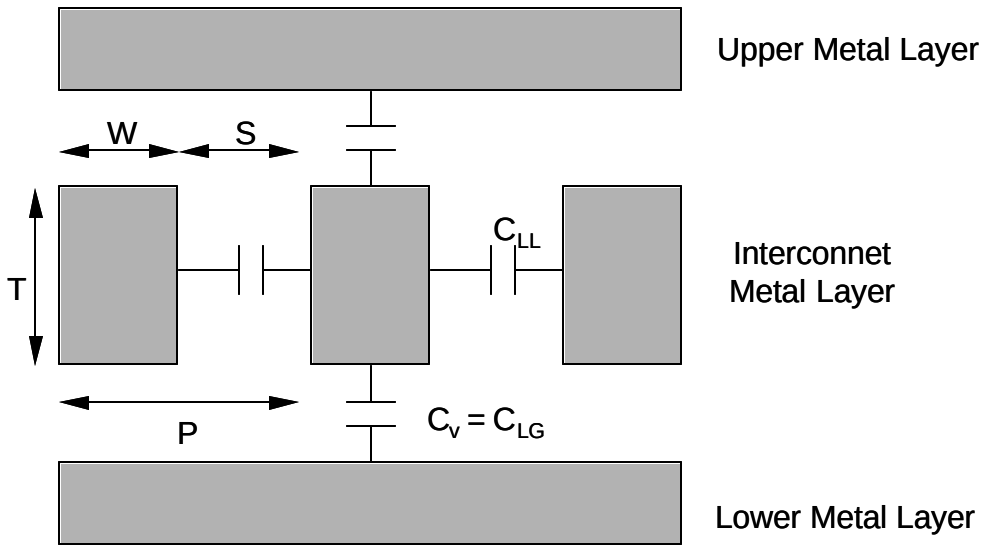

Fig.1.2 Schematic diagram of an interconnect system, where P is the metal pitch, W the metal width, S the space between metals, T the metal thickness, C_{LL} the lateral line-to-line capacitance, C_v the vertical layer-to-layer capacitance, and C_{LG} the line-to-ground capacitance (3).

Based on Eq. (1-1), increased signal speed can be obtained in three ways: (a) changing the layout and/or the ratio of width to thickness for the metal lines, (b) decreasing the specific resistivity ρ of the interconnect metal, and (c) decreasing the dielectric constant k of the interlevel dielectric material. Therefore, the semiconductor industry has recognized the need to introduce low-k dielectric materials (k<3) and a high conductive metal, such as copper, to meet the requirement for future devices as outlined in the National Technology Roadmap (7). It has been reported that replacement of Al by Cu will reduce the RC delay by approximately 35% and the substitution of SiO_2 (k= 4) with air (k=1) will reduce the RC delay about 75% (3).

1.2. DIFFUSION BARRIERS

The interaction between Si and Cu is rapid and detrimental to the electrical performance of Si even at temperatures below 200°C (8, 9). Cu can readily reacts with most silicides such as $CoSi_2$, $CrSi_2$ and $TiSi_2$, at temperatures below 450°C. Cu can also reacts at low temperature with most metal, such as Al, Au and Pd, which are commonly used in microelectronic device. Copper layers exhibit poor adhesion on both SiO_2 and polymer substrate. Annealing a Cu film on a SiO_2 substrate causes the film to peel under tensile stress. When copper contacts a polymer, such as polyimide, Cu forms a weak chemical bond with polyimide and diffuses into it to form agglomerates at low temperature (10). Moreover, copper corrodes easily upon exposure to moisture or oxygen and a technique to passivate the copper surface is essential for multilevel copper interconnection (11). A schematic diagram summarizes the interaction between Cu and contact environments, such as Si, silicide, metal, oxygen, SiO_2 and ploymide (see Fig. 1.3) (10). The relatively low interfacial reaction temperatures for all these system cause a serious thermal stability issue in Cu-based metallization. To avoid abovementioned problems, it is necessary to implement a diffusion barrier layer as well as an adhesion promoter into the Cu metallization scheme and to encapsulate copper conductors from all sides.

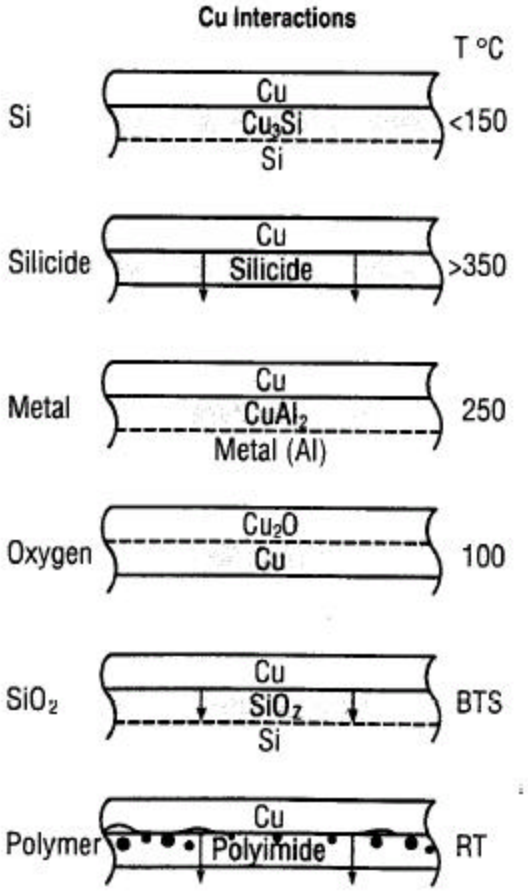

Fig. 1.3 Schematic presentation of the problems related to copper metallizations (10). (Reprinted with permission from MRS)

The interconnect structure of Cu metallization is fabricated using the damascene process (Fig. 1.4) where Cu is deposited into wiring channels patterned into the interlayer dielectric layer (ILD) and then planarized using chemical mechanical polishing (CMP). A barrier is a conductive layer deposited between Cu interconnects and the ILD low-k substrate that blocks the undesired migration of Cu. Selection of such a material starts with an investigation of mutual diffusivity and interactions. Grain boundary and dislocation diffusivities are generally several orders of magnitude higher especially at temperatures that less than half the melting point in degree Kelvin. Since the diffusivity is directly related to melting point of the host material, the best diffusion barriers have the highest melting points (12, 13). The ideal diffusion barrier also needs

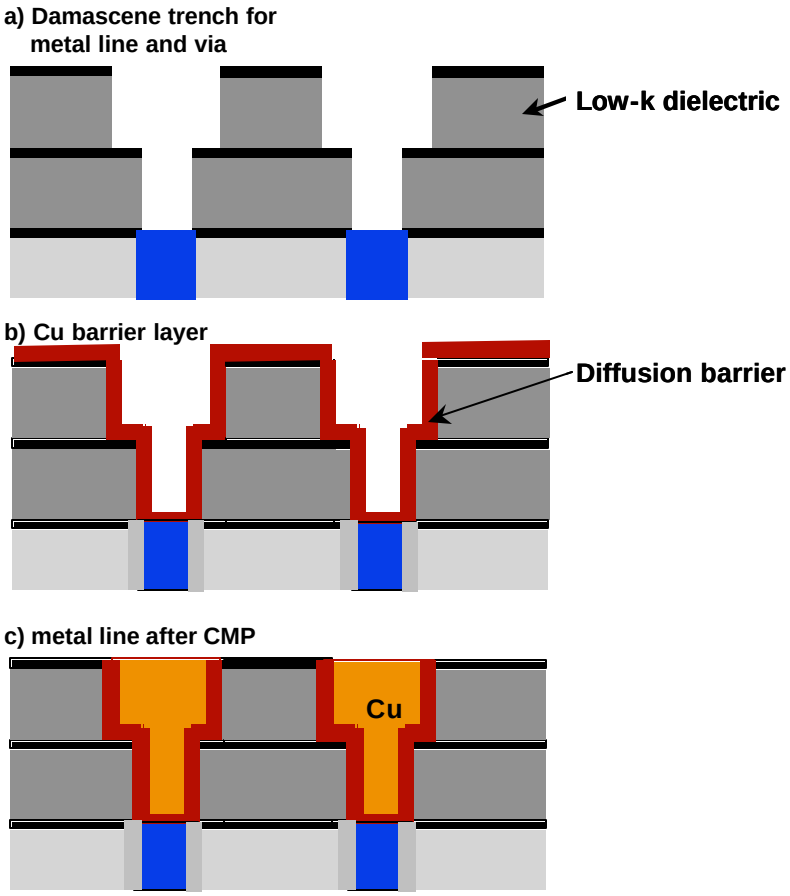

Fig.1.4 Schematic diagram of a basic Cu damascene process interconnect structure

to be chemically stable since purely disperse and relatively weak interactions cannot withstand the mechanical or thermal stress that is encountered under typical processing conditions. Accordingly, refractory metallic systems with characteristically high melting points and chemical inertness serve as viable candidates for diffusion barrier application in Cu-based metallization schemes. In addition of these requirements, the barrier materials must have excellent adhesion to the dielectrics and the copper. Good adhesion is necessary to resist delamination during processing or thermal stressing, and for electromigration. The diffusion barrier must also have good step coverage to minimize cusping and potential voids. It must also

be smooth and free of defects, both of which significantly impact the quality for the subsequent seed layer. The thickness of the barrier is also an important concern since thicker liners increase the effective resistance of the line and, in more aggressive structures, lead to nonuniform Cu nucleation and poor filling.

Various refractory transition metals and their binary and ternary compounds have been suggested for diffusion barrier applications. The corresponding materials systems are classified into six groups (14, 15):

1. Refractory metals such as Ta, Ti, W, Mo, Co, Pd and Nb.
2. Refractory metallic alloys, including Ti_xW_{1-x}, Ni_xMo_{1-x}, and Ir_xTa_{1-x}.
3. Polycrystalline or amorphous refractory metal-silicon alloys or compounds, such as $TiSi_2$, $CoSi_2$, $TaSi_2$, W_xSi_{1-x}.
4. Polycrystalline or amorphous refractory metal-nitrogen, metal-oxygen, metal-carbon, and metal-boron compounds, such as TiN_x, HfN, W_2N, TiC, TaN_x, Mo-O and TiB_2.
5. Amorphous ternary barriers such as TiSiN, WSiN, MoSiN, TaSiN and WBN.
6. Polycrystalline or amorphous carbon-based alloys and compounds, such as diamond-like carbon coatings.

The research presented here will focus on two major barrier materials (Ta and TiN) for Cu/low-*k* system. Tantalum is a single transition metal with a high melting point of 3017 ºC and therefore has high activation energy for both lattice and grain boundary self-diffusion. Cu-Ta phase diagram (14, 16) (Fig.1.5) consists of the following equilibrium phases: (a) the liquid; (b) the fcc terminal solid solution (Cu), with limited solid solubility of Ta; and (c) the bcc terminal solid solution (Ta), with limited solid solubility of Cu. The diagram is characterized by an S-shaped near flat liquids above ~1800°C, which implies the existence of a metastable liquid-liquid

miscibility gap at lower temperatures. Therefore, the Cu-Ta phase diagram indicates that they are almost completely immiscible up to their melting points and do not react to produce any compounds. The reaction of Ta and Si is known to require quite high temperature (650ºC (17)), enabling a reasonable stable Ta/Si interface. Therefore, Ta is a good diffusion barrier candidate compared to other polycrystalline transition metal films (such as Pd, Cr, Co and Ni), which usually react with both Cu and Si at relatively low temperature. Another candidate of barrier material widely employed in aluminum-based interconnect system is titanium nitride (18). TiN served as a diffusion barrier during or after high-temperature Al reflow processing. Ti/TiN are also applied in the contact plug to reduce contact resistance and improve W adhesion, whereas TiN is further used to protect the contact from the fluorine-containing CVD W precursor. As such, the possibility of extending its applicability to copper-based interconnects represents a highly attractive option, both technically and economically. The properties of both barrier candidates are summarized in Table 1.1 (19-21).

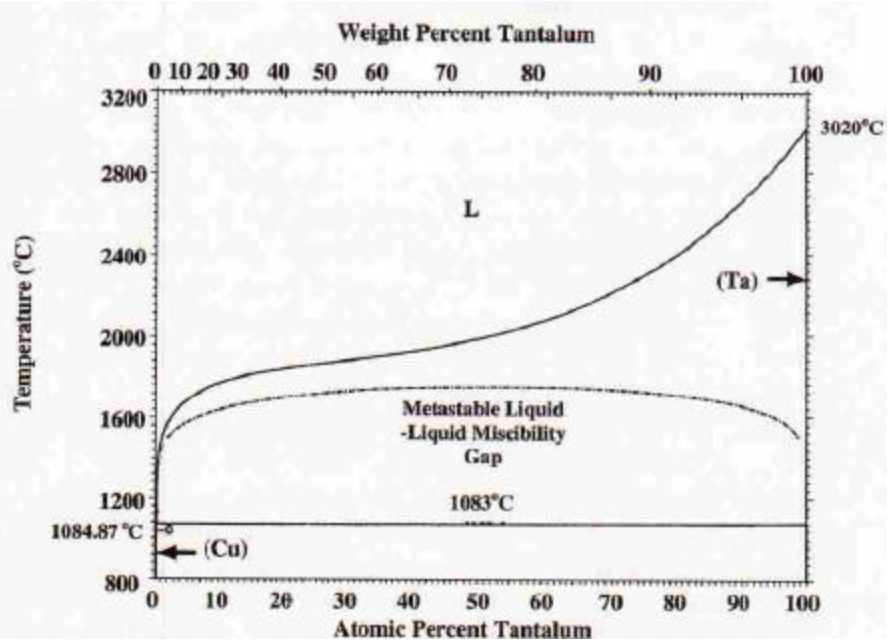

Fig. 1.5 Cu-Ta phase diagram (16) (Reprinted with permission from ASM International)

Table 1.1 Diffusion barrier properties (19-21)

		Ta	TiN
Resistivity (μΩ cm)	bulk	13 [19]	10-30 [20]
	PVD/CVD	100-170 [19]	150-2500 [20]
Melting point (°C)		3017 [19]	2960 [20]
Thermal conductivity (W m^{-1} K^{-1})		57 [19]	19 [20]
Coefficient of thermal expansion (ppm K^{-1})		6.3 [19]	9.3 [20]
Stress (Mpa)		+350 [21]	-750 [21]
Barrier Performance (at/cm^3)*		6 x10^{16} [21]	10^{17} [21]

* Barrier performance is measured by the number of copper (atom) diffused into the dielectrics per unit volume (cm^3)

1.3. LOW-*k* DIELECTRICS

The introduction of low-dielectric-constant (*k*<3) materials as interlayer dielectric has been intensively proposed to address the challenging problem arising from the continuous scaling of device dimensions to less than a quarter micron. In the long run, the use of low-*k* materials seems to be more attractive than the use of low-ρ interconnects, because the capacitance reduction due to the low *k* can affect the device in three ways: (a) to increase device speed by lowering interconnect RC delay; (b) to diminish crosstalk by reducing the capacitance between parallel running lines; (c) to reduce power dissipation because the heat given off is directly proportional to the capacitance (1). For this reason, a considerable number of low-κ dielectric materials are being actively studied.

The dielectric constant (k) is a characteristic quantity of a given dielectric substance, sometimes called the relative permittivity (22). In general, the dielectric constant is a complex constant, with the real part giving reflective surface properties (Fresnel reflection coefficients, ε_r), and the imaginary part giving the radio absorption coefficient. Since the imaginary part may usually be neglected, except at very high frequencies ($>10^{13}$ s^{-1}), the real component (ε_r) is often called the dielectric constant (k) as shown in Eq. (1-2):

$$k = \varepsilon_r = 1 + \chi_e = \varepsilon/\varepsilon_0 \qquad (1\text{-}2)$$

where ε is the electric permittivity of the dielectric, ε_0 is the permittivity of free space, and χ_e is the electric susceptibility. It is an expression describing the tendency of a material to permit an applied electric field to induce dipoles in the material.

In order to reduce the k value relative to that of SiO_2 (k=4), it is necessary (a) to incorporate atoms and bonds that have a lower polarizability, (b) to lower the density of atoms and bonds in the material (23). With respect to the first effect, there are several components to the polarizability that must be minimized in reducing the dielectric constant. The polarization components usually considered are the electronic, atomic, and orientational responses of the materials (24). Single C-C and C-F are among those having the lowest electronic polarizability due to strong electron-withdrawing inductive effects, thus making fluorinated and nonfluorinated aliphatic hydrocarbons potential candidates for low-k applications. The dielectric constant of materials can also be reduced by decreasing the density. The density can be lowered by using lighter atoms and/or by incorporating more free space around the atoms, for example, the incorporation of light, space-occupying groups such as H or CH_3 into the silica network can significantly lower the material density, and therefore the dielectric constant. Introduction of nanometer-sized (2-50 nm) pores into the material is a natural extension of this strategy to

increase the free space and decrease the material density. Because introduction of voids will compromise other material properties such as mechanical strength, the chemical structure of the porous network must be carefully designed to achieve sufficient thermomechanical stability.

In addition to low dielectric constant, candidate ILD dielectrics must satisfy a significant number of requirements in order to be successfully integrated in a ULSI device. These requirements are based on electrical properties (low dielectric constant, low dissipation factor, low leakage current), thermal stability (stability >400°C), mechanical properties (low stresses, minimal Young's modulus and hardness), adhesion and compatibility with other materials, patternability, and chemomechanical polishing (CMP) capability, etc. The desired property requirements of low-k as interlayer-dielectric materials are listed in Table 1.2 (25). So far, the industry has not compiled a standard for low-k materials properties. The requirement may vary from one application to another and depend on the interconnect architecture. Table 1.3 (26) lists the most promising candidates for low-k ILDs, along with key performance parameters. Early winners include hydrogen silsesquioxane (HSQ) and fluorinated oxides delivering k of 3.0 and 3.5, respectively. For k below 3.0, organic polymers such as poly (arylene) ethers (PAE), benzocyclobutene (BCB) and an aromatic hydrocarbon show promise, as do silicon-based CVD films. For ultra low-k (<2.0), feasible spin-on candidates include nonporous silica films (κ=1.3~2.5), porous polymers and polytetrafluoethylene (PTFE)(k=1.9). Low-k materials are typically produced by either chemical vapor deposition or spin-on deposition. Integration of low-k dielectrics into multilevel metallization systems involves a complex tradeoff between chemical, mechanical, thermal and electrical properties as well as cost.

Table 1.2 Requirements for low dielectric constant interlayer-dielectric materials (25)(Used with permission from MRS)

Electrical	Chemical	Mechanical	Thermal
Anisotropy Low dissipation Low leakage current Low charge trapping High electric-field Strength High reliability	Chemical resistance Etch selectivity Low moisture absorption Low solubility in water Low gas permeability High purity No metal corrosion Long storage life Environmentally safe	Thickness uniformity Good adhesion Low stress High hardness Low shrinkage Crack resistance High tensile modulus	High thermal stability Low coefficient of thermal expansion Low thermal shrinkage Low thermal weight loss High thermal conductivity

Table 1.3 Likely low-*k* materials for ULSI interconnects (26)

Dielectric	Dielectric constant (*k*)	Glass transition Tg (°C)	Refractive index	Water absorption (%)	Stress (Mpa)	Gap fill (μm)	Cure Temperature (°C)	Weight loss (% wt) at 450°C
FSG (silicon oxyfluoride)	3.4-4.1	>800	1.42	<1.5	-130	<0.35	No issue	none
HSQ (hydrogen silsesquioxane)	2.9	>500	1.37	<0.5	70-80	<0.1	350-450	<3
PAE (poly arylene ethers)	2.6-2.8	260-450	1.67	<0.4	60	<0.15	375-425	<1.0
DVS-BCB (divinyl siloxane benzocyclobutene)	2.65	>350	1.561	<0.2	30-35	<0.22	300	<1.0
Aromatic hydrocarbon	2.65	>490	1.628	<0.25	55-60	<0.05	400-450	<1.0
Hybrid silsesquioxane	<3.0	T_{melt}>250	1.58	0	30-40	<0.1	450	6
Nanoporous silica	1.3-2.5	>500	1.15	TBD	0	<0.25	400	none
OSG (organosilicate glass, SiOC)	2.7 (variable C content)	>600		<0.2				
PTFE (polytetrafluoroethylene)	1.9	-100	1.34	<0.01	25-27	<0.3	360-390	0.8
Parylene AF4 (aliphatic tetrafluoinated poly-pxylyene)	1.548	T_{melt}>510			100	0.18	420-450	0.5

1.4. EXPERIMENTAL ASPECTS

X-ray photoelectron spectroscopy (XPS) is employed in this study to characterize the surface composition, chemical bond and film growth mode on the various substrates in ultra-high vacuum (UHV) system. Ultra high vacuum is required for most surface science experiments for two principal reasons: (a) To enable atomically clean surfaces to be prepared for study, and such surfaces to be maintained in a contamination-free state for the duration of the experiment; (b) To permit the use of low energy electron and ion-based experimental techniques without undue interference from gas phase scattering. At room temperature, UHV conditions (pressure $<10^{-10}$ Torr) maintain a clean surface (contamination no more than 0.05 atom layers) for long enough (30 min) to conduct experiments according to gas kinetic theory. Tantalum deposition is performed by DC magnetron sputtering deposition. Titanium nitride is deposited by metal organic chemical vapor deposition (MOCVD) using tetrakis(diethylamido) titanium (TDEAT) as precursor. The fundamental principles for each technique are discussed as follows.

1.4.1. X-ray Photoelectron Spectroscopy (XPS)

X-ray photoelectron spectroscopy (XPS) was developed in the mid-1960s by Kai Siegbahn and his research group (27). The phenomenon is based on the photoelectric effect outlined by Einstein in 1905 where the concept of the photon was used to describe the ejection of electrons from a surface when photons impinge upon it. The excitation process of photoelectrons is illustrated in Fig. 1.6. When a beam of light strikes a surface, photons are absorbed by surface atoms, leading to ionization and the emission of core (inner shell) electrons. The kinetic energy E_{kin} of the ejected photoelectron is given by

$$E_{kin} = h\nu - E_B - \Phi_s \qquad (1\text{-}3)$$

where *hν* is the energy of the incident X-rays, and E_B is the binding energy of the atomic orbital from which the electron originates, and Φ_s is the spectrometer work function (a constant for a given analyzer). By measuring the kinetic energy of the photoelectron, the binding energy can be determined using Eq. (1-3) (28).

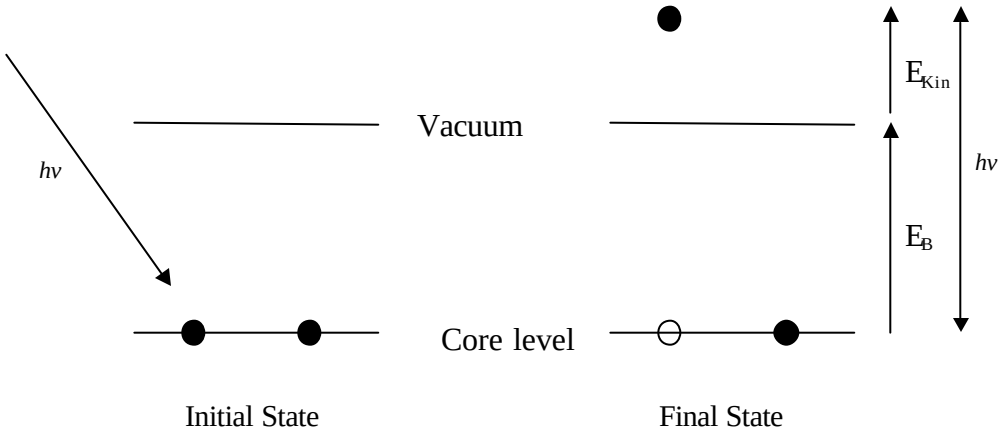

Figure 1.6 Schematic of XPS emission process for a model atom.

For each and every element, there will be a characteristic binding energy associated with each core atomic orbital i.e. each element will give rise to a characteristic set of peaks in the photoelectron spectrum. The exact binding energy of an electron depends not only upon the level from which photoemission is occurring, but also upon the formal oxidation state of the atom and the local chemical and physical environment. Atoms of a higher positive oxidation state exhibit a higher binding energy due to the extra coulombic interaction between the photo-emitted electron and the ion core. This ability to discriminate between different oxidation states and chemical environment is one of the major strength of the XPS technique. Furthermore, the intensity of the peaks is related to the concentration of the element within the sampled region. Thus, the

technique is capable of yielding a quantitative analysis and is sometimes known by the alternative acronym, ESCA (Electron Spectroscopy for Chemical Analysis).

For XPS, Al K_α (1486.6eV) or Mg K_α (1253.6eV) are often the photon energies of choice due to their relatively narrow linewiths and high photon energies. The emitted photoelectrons will therefore have kinetic energies in the range of 0 - 1250 eV or 0 - 1480 eV. Since such electrons have very short inelastic mean free path (IMFP) in solids (tens of angstrom), only those that are very close to the surface can be ejected from the sample. For that reason, XPS is a highly surface-sensitive technique with analysis depths typically less than 100 Å.

The concentric hemispherical analyzer (CHA) is currently the most popular electron energy analyzer used in XPS. The schematic diagram of a CHA is shown in figure 1.7 (29,30). Two hemispheres of radii R_1 (inner) and R_2 (outer) are positioned concentrically with entrance and exit slits of width w_1 and w_2. Potentials $-V_1$ and $-V_2$ are applied to the inner and outer hemispheres respectively, with V_2 grater than V_1. The electron entering through entrance slit with a kinetic energy E will follow the trajectory through the analyzer along the median equipotential surface of radius r_0 and will be focused at the exit slit. The hemispherical analyzer is combined with electron retarding-field input lens to achieve the resolution required for XPS. This combination may be operated in either the fixed analyzer transmission (FAT) mode or constant retard ratio (CRR) mode. In the FAT mode where absolute resolution (ΔE) is constant at all energies in the spectrum, the electrons are retarded to a constant energy, called the pass energy (Ep) before they enter the analyzer. Only the electrons with $E=Ep+\Delta E$ can go through the spectrometer. The chemical shift ΔE is of the order of 0.5~1 eV, limited by the x-ray line widths. Thus, without retardation, an absolute resolution (ΔE) at an energy of 1500 eV requires a relative resolution ($R=\Delta E/E$) of $\sim 10^{-4}$, which is not easy to achieve without constructing an excessively

large analyzer. With retardation, a pass energy of 20 eV for the same ΔE would require a relative resolution of only ~10^{-2}, which is easier to achieve. A complete photoelectron spectrum is recorded by ramping the lens retarding field voltage (V_R) ($E_p = E-V_R$) and plotting a spectrum of electron energy versus electron counts. In the CRR mode, the voltages on the hemispheres of the analyzer (V_1 and V_2) are ramped with the energy of the spectrum so that the ratio of electron kinetic energy to pass energy is a constant; this constant is the retard ratio of the analyzer. This mode of operation is particularly popular for Auger Electron Spectroscopy (AES) as the analyzer transmission is high at high pass energy, thus effectively increasing the low electron yield at the high kinetic energy of the spectrum.

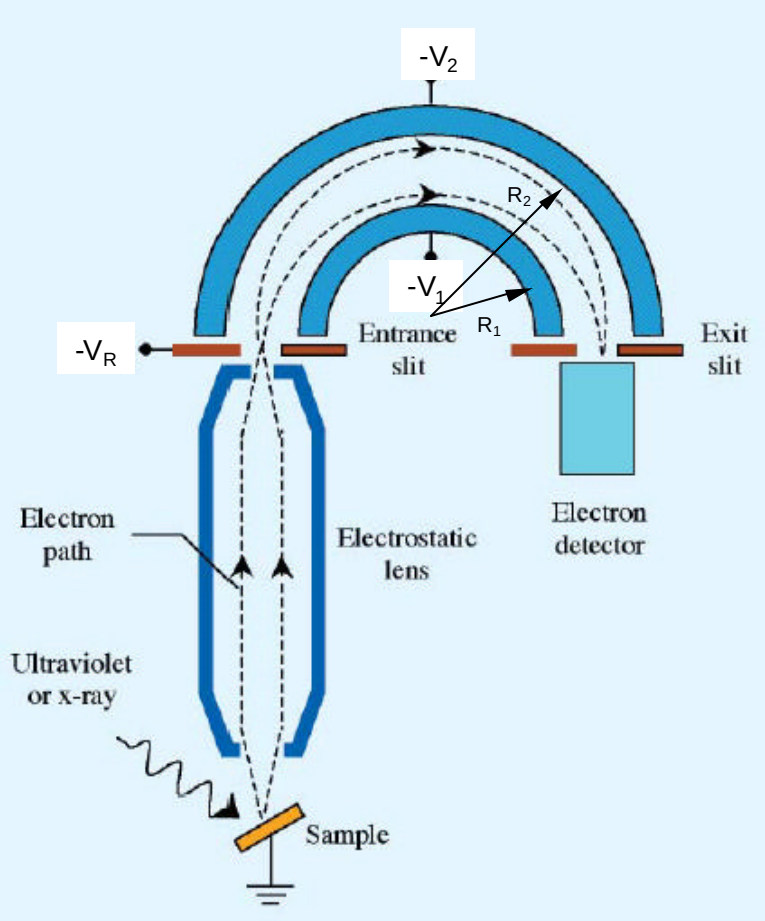

Fig.1.7 Schematic cross-section of a concentric hemisphere analyzer

XPS also has the ability to perform non-destructive analysis of the variation of surface composition with depth (with chemical state specificity). In the case of an idealized homogeneous, semi-infinite, flat-surface specimen, the escape depth λ_e (IMFP) for normal emission ($\vartheta=0°$) decreases as $\lambda_e \cos\vartheta$ for emission at angle ϑ. This technique is called Angle Resolved XPS (31) (Fig.1.8). In this way it is possible, by varying the emission angle ϑ, to get a signal from the first atomic monolayer only. Comparing relative intensities at low and high take off angles indicates whether a species is enriched or depleted in the surface region.

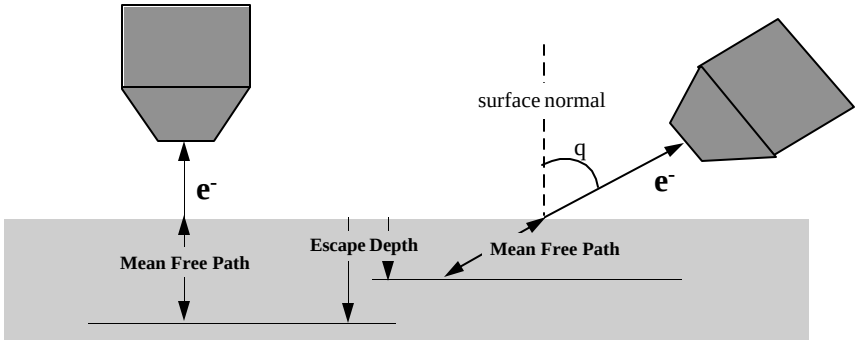

Fig. 1.8 Angle resolved XPS

In addition to the ejection of photoelectrons, X-ray excited Auger electrons may be emitted as a result of the relaxation of the excited ions remaining after the photoemission process. The Auger process (Figure 1.9) involves three energy levels: an empty core level (K-shell) and two higher levels (L or M shells). For an X-ray excited Auger process, the initial empty core level (the electron vacancy with energy E_K) is created with an X-ray. The core level is then filled with an electron from a higher level (with energy, E_{L1}) and the energy liberated in this process is simultaneously transferred to a second electron; a fraction of this energy is

required to overcome the binding energy (E_{L3}) of this second electron, the remainder is retained by this emitted *Auger electron* as kinetic energy.

In contrast to the photoelectron in XPS, the energy of the Auger electron is independent of the mode of the initial ionization and equals to the difference between the energy of the initial ion and the doubly charged final ion. For the KLL transition (Figure 1.9), the kinetic energy (E_{kin}) of Auger electron is given by:

$$E_{kin} = (E_K - E_{L1}) - E_{L3} \qquad (1\text{-}4)$$

where E_K, E_{L1}, and E_{L3} are electron energy at K, L_1, and L_3 levels, respectively. The energy of the Auger electron is characteristic of the element in the sample and in special cases can be used to extract chemical bonding information from Auger peak energy positions and lineshapes.

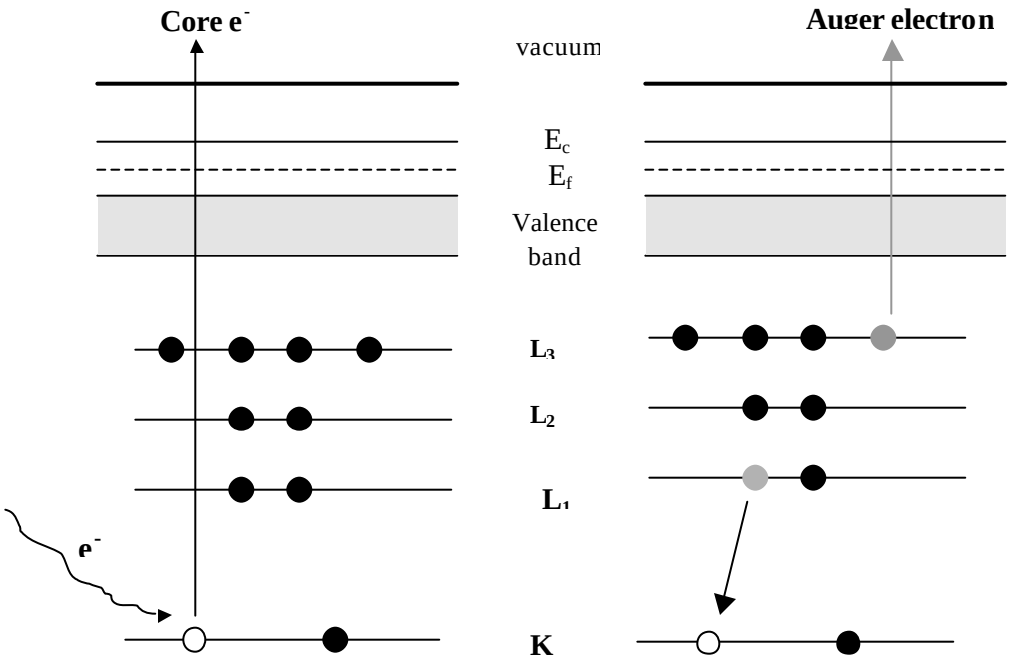

Figure 1.9 Schematic of the Auger process of a model atom. Step (a) is the initial photoelectron process and step (b) is the emission of the Auger electron.

1.4.2. XPS for Nucleation Modes

Different growth modes are possible during the initial stages of the deposition of an adsorbate (in this case a metal) onto a substrate, depending upon the strengths of the interactions between the adsorbate and substrate atoms. The change in adsorbate and substrate XPS (or Auger) intensities with coverage, the so-called "uptake" curve, is frequently used to analyze such modes. Volmer–Weber (VW) growth involves the formation of 3-dimensional small particles on the substrate, which then grow into larger clusters that coalesce. This behavior indicates that the deposited metal-metal interactions are stronger than metal–substrate interactions (M–M > M–S), and that the metal adsorbate does not "wet" the surface. Frank–van der Merwe (FM) growth is layer-by-layer growth of the adsorbed metal, where M–M < M–S. Stranski–Krastanov (S–K) growth exhibits conformal growth for the first 1-3 monolayers (ML), followed by 3-D formation at higher coverages. There are many possible reasons for this mode to occur, and almost any factor which disturbs the monotonic decrease in binding energy, characteristic of layer growth, may be the cause. For example, the lattice parameter of, or symmetry of, or molecular orientation in, the intermediate layer may not be able to be continued into the bulk crystal of the deposit. This results in a high free energy of the deposit-intermediate-layer interface which favors subsequent island formation (32). Typical plots of XPS or AES adsorbate intensity versus deposition time (or estimated overlayer coverage) are shown in Figure 1.10 for the three common growth modes. For VW growth, the uptake curve exhibits near linear or continuous behavior till coalescence sets in, since layer-by-layer attenuation does not occur. The FM growth mode typically has a plot with several segments of changing slope, with each break indicating the attenuation of the intensity of the previous layer by subsequent layers. The plot of SK

growth, though difficult to distinguish from FM mode, has one or two breaks and typically begins to level off at higher coverages (when islanding occurs).

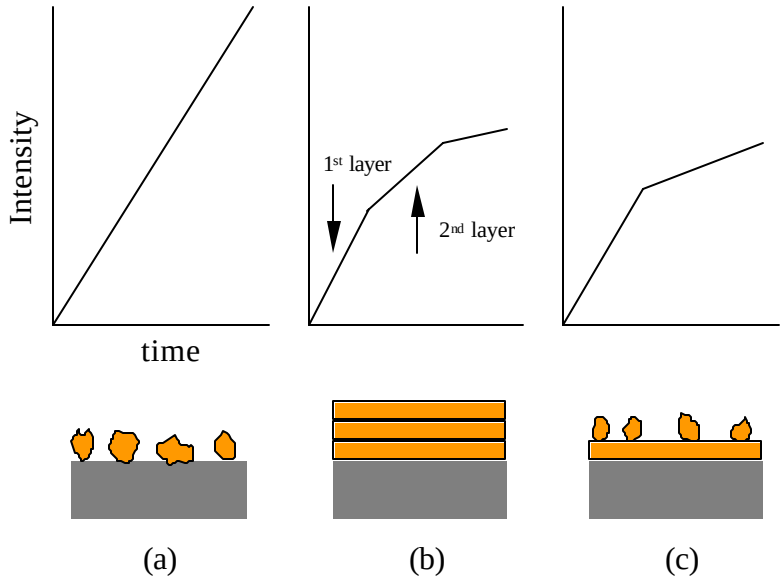

Figure 1.10. Intensity vs. time plots of (a) Volmer–Weber (islanding), (b) Frank–van der Merwe (layer-by-layer), and (c) Stranski–Krastanov growth (monolayer then islanding)

1.4.3. Thin Film Deposition Techniques

1.4.3.1 PVD---DC Magnetron Sputtering

Sputtering, a form of physical vapor deposition (PVD), was discovered in 1852 by Sir William Robert Grave and developed as a thin film deposition technique in the 1920s by Langmuir (33). Sputtering is the act of bombardment of a surface with energetic particles such as accelerated ions. In the process surface atoms of the solid are scattered backward due to the collisions between the surface atoms and the energetic particles. In DC magnetron sputtering (Figure 1.11), a magnetic field is imposed in such a way that the electrons are trapped in a region near target surface. So a gas atom (Ar) entering the electron cloud has a grater probability of

losing electrons and becomes ionized (Ar^+). The ions are instantly attracted to the negatively biased target where they collide with its surface, causing atoms of materials from its surface to be ejected. This so called magnetron action only occurs when the magnetic field (B) and the electric field (E) are normal (at 90°) to each other. This electron trapping results in a greater ionization efficiency of the Ar atoms in the plasma. This improved ionization efficiency has resulted in a technique that allows higher sputtering rates at lower pressures and less gas incorporation into these sputtered films. The operating pressures for DC magnetron sputtering can be performed at pressures as low as 10^{-4} Torr (34).

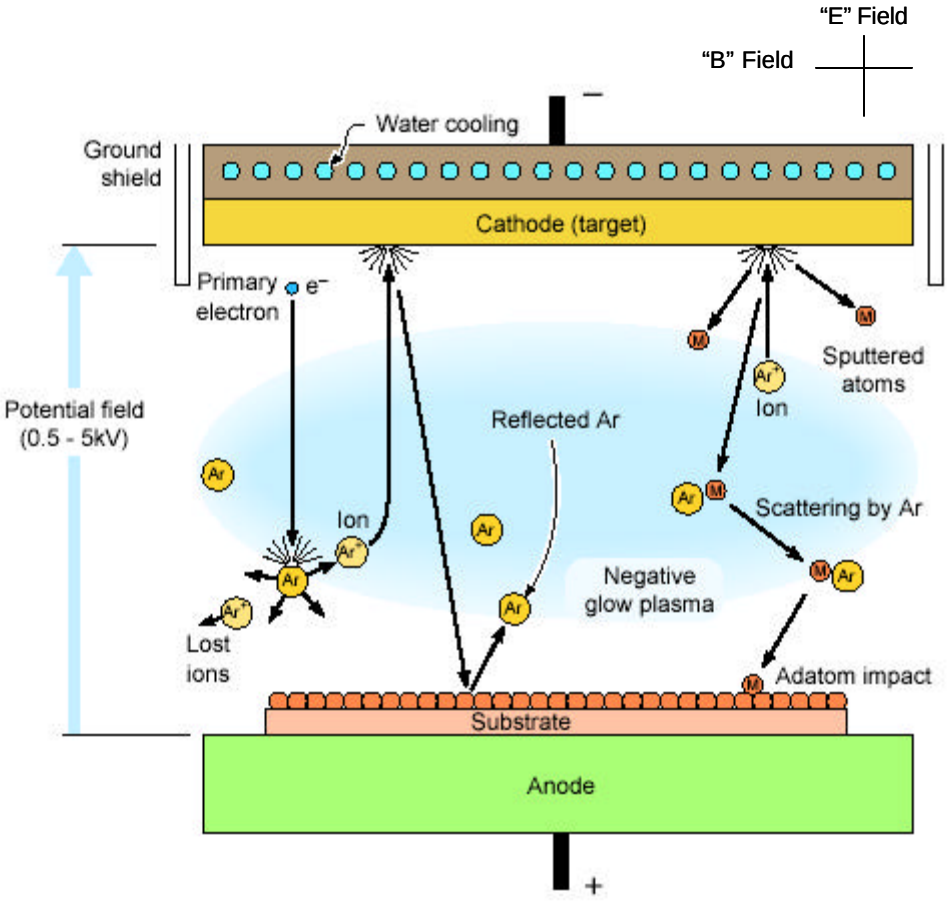

Figure 1.11. The DC magnetron sputtering process.

1.4.3.2 Metal Organic Chemical Vapor Deposition (MOCVD)

As decreasing feature size in ULSI, the further application of PVD process becomes increasingly difficult due to its poor conformality. Therefore the chemical vapor deposition (CVD) has become an attractive alternative to PVD since it can provide more uniform step coverage over high aspect ratio structures (shown in Fig. 1.12). Applications of CVD range from the fabrication of microelectronic devices to the deposition of protective coatings and dielectric films.

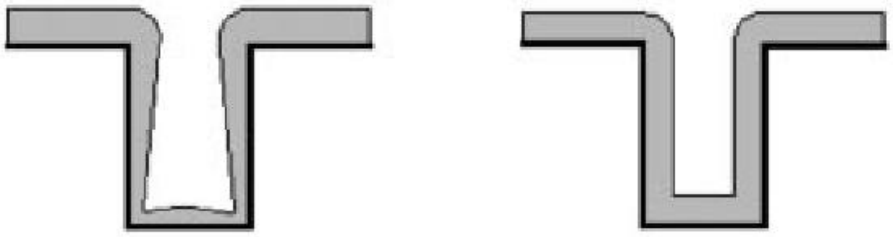

(a) Non-conformal deposition by PVD (b) Conformal deposition by CVD

Fig. 1.12 PVD vs. CVD

In a typical CVD process as shown in Fig. 1.13, reactant gases (often diluted in a carrier gas) at room temperature enter the reaction chamber. The gas mixture is heated as it approaches the deposition surface, heated radiatively or placed upon a heated substrate. Depending on the process and operating conditions, the reactant gases may undergo homogeneous chemical reactions in the vapor phase before striking the surface. Near the surface thermal, momentum, and chemical concentration boundary layers form as the gas stream heats, slows down due to viscous drag, and the chemical composition changes. Heterogeneous reactions of the source gases or reactive intermediate species (formed from homogeneous pyrolysis) occur at the deposition surface forming the deposited material. Gaseous reaction by-products are then

transported out of the reaction chamber. Because the deposition process includes force convection, boundary-layer diffusion, surface adsorption, decomposition, surface diffusion, and incorporation, there are several variables to be controlled. Temperature, pressure, flow rate, position, and reactant ratio are important factors for high-quality films. MOCVD (Metal Organic Chemical Vapor Deposition), also called OMCVD (Organometallic Chemical Vapor Deposition), MOVPE (Metal Organic vapor phase epitaxy), has been used for crystal growth since 1960. MOCVD uses MO (Metal organic) compound as source of the material (precursor).

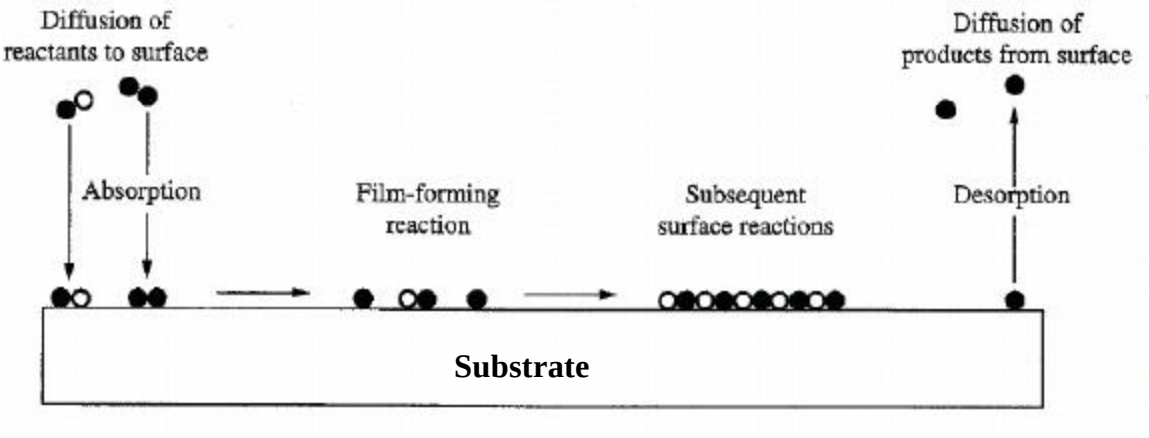

Fig. 1.13 Principle of CVD process

1.5. CHAPTER REFERENCES

(1) Jeng, S.-P.; Havemann, R.; Chang, M. Mater, *Res. Soc. Symp. Proc. 337,* 25. Material Research Society, Pittsburgh, 1994

(2) Maier, G. *Prog. Polym. Sci.* **2001,** *26,* 3.

(3) Lee, W. W.; Ho, P. *MRS Bulletin* **1997,** *22,* 19.

(4) Bohr, M. T. *Solid State Technol* **1996,** *9*, 105.

(5) Treichel, H.; Ruhl, G.; Ansmann, P.; Wurl, R.; Muller, C.; Dietlmeier, M. *Microelectronic Engineering* **1998,** *40*, 1.

(6) Grill, A. *Diamond and Related Materials* **2001,** *10*, 234.

(7) *The National Technology Roadmap for Semiconductors*; Semiconductor Industry Association: San Jose, CA, 1999.

(8) Torres, J. *Appl. Surf. Sci.* **1995,** *91*, 112.

(9) Faupel, F. *Phys. Stat. Sol. (a)* **1992,** *134*, 9.

(10) Li, J.; Mayer, J. W. *MRS Bulletin* **1993,** *18*, 52.

(11) Lakshminarayanan, S.; Steigerwald, J.; Price, D. T.; Bourgwois, M.; Chow, T. P.; Gutman, R. J.; Murarka, S. P. *IEEE Electr. Dev. Lett.* **1994,** *15*, 307.

(12) Murarka, S. P. *Materials Science and Engineering* **1997,** *R19*, 87.

(13) Nicolet, M.-A. *Thin Solid Films* **1978,** *52*, 415.

(14) Kaloyeros, A. E.; Eisenbraun, E. *Annu. Rev. Mater. Sci.* **2000,** *30*, 363.

(15) Wang, S. Q. *Mater. Res. Soc. Bulletin* **1994,** *19*, 30.

(16) Subramanian, P. R.; Laughlin, D. E. *Binary Alloy Phase Diagrams, Second Edition*; William W. Scott, Jr.: Materials Park, Ohio, 1990.

(17) Ottaviani, G. *Thin Solid Films* **1986,** *140*, 3.

(18) Ting, C. Y.; Wittmer, M. *Thin Solid Films* **1982,** *96*, 327.

(19) *http://www.webelements.com*

(20) Pierson, H. O. *Handbook of Refractory Carbides and Nitrides*; Noyes/William Andrew Publishing: NY, 1996.

(21) Shacham-Diamand, Y. *AMC 2000* Tutorial.

(22) Bekefi, G.; Barrett, A. H. *Electromagnetic Vibrations, Waves, and Radiation*; MIT Press: Cambridge, MA, 1987.

(23) Morgen, M.; Ryan, E. T.; Zhao, J.-H.; Hu, C.; Cho, T.; Ho, P. S. *Annu. Rev. Mater. Sci.* **2000,** *30*, 645.

(24) Simpson, J. O.; St.Clair, A. K. *Thin Solid Films* **1997,** *308-309*, 480.

(25) Ting, C. H.; Seidel, T. E. *Mater. Res. Soc. Symp. Proc.* **1995,** *381*, 3.

(26) Peters, L. *Semiconductor International* **1998**.

(27) Siegbahn, K.; Nording, C. N.; Fahlman, A.; Nordberg, R.; Hamrin, K.; Hedman, J.; Johansson, G.; Bermark, T.; Karlsson, S. E.; Lindgren, I.; Linberg, B. *ESCA: Atomic, Molecular and Solid State Structure Studied by Means of Electron Spectroscopy*; Almqvist and Wilksells: Uppsala, 1967.

(28) Moulder, J. F.; Stickle, W. F.; Sobol, P. E.; Bomben, K. D. *Handbook of X-ray Photoelectron Spectroscopy*; Physical Electronics, Inc.: Eden Prairie, Minnesota, 1995.

(29) Briggs, D.; Seah, M. P. *Practical Surface Analysis*, 2nd ed.: Wiley, New York, 1990.

(30) Riviere, J. C.; Myhra, S. *Handbook of Surface and Interface Analysis: Methods for Problem-Solving*; Marcel Dekker: New York, 1998.

(31) Osiceanu, P. *Revue Roumatine de Chimie* **2002,** *47*, 521.

(32) Venables, J. A.; Spiller, G. D. T.; Hanbucken, M. *Rep. Prog. Phys.* **1984,** *47*, 399.

(33) Quirk, M.; Serda, J. *Semiconductor Manufacturing Technology*; Prentice-Hall, Inc.: Upper Saddle River, New Jersey; Columbus, Ohio, 2001.

(34) Wasa, K.; Hayakawa, S. *Handbook of Sputter Deposition Technology, Principles Technology and Applications*; Noyes Publications: Park Ridge, New Jersey, 1992.

CHAPTER 2

Ta METALLIZATION OF Si-O-C SUBSTRATE AND Cu METALLIZATION OF Ta/Si-O-C MULTILAYER

2.1. INTRODUCTION

Tantalum is a promising material as a diffusion barrier layer for Cu metallization, because Ta and Cu are almost completely immiscible (1, 2). Ta has a high melting point (3290 K) and a relatively low resistivity of ~100 μΩ cm (3). The integration of Cu with low-*k* materials may decrease RC delays in signal propagation but pose additional problems because such materials are often porous and contain significant amounts of carbon. Therefore barrier metal diffusion into the dielectric and the formation of interfacial carbides and oxides are of concern. Metal oxides or carbides at the copper/barrier interface inhibit Cu wetting and the formation of adherent, laminar interfaces (4-6). Barrier metal diffusion into the dielectric can raise the dielectric constant, and degrade device electronic properties if diffusion into the Si substrate follows.

Although numerous studies concerning Ta barriers on SiO_2 have been published (7, 8), Ta interactions with low-*k* materials have been less well studied. In this work, XPS has been used to characterize the interfacial chemical reactions between sputter-deposited Ta and a Si-O-C low-*k* substrate, and between sputter-deposited Cu and the Ta overlayer. These results show that Ta reacts with the low-*k* substrate to form Ta oxide and Ta carbide species, but that the specific composition of the interfacial reacted layer varies with the Ta deposition rate. Deposition rates were determined from the attenuation of the substrate Si(2p) signal in XPS. The results were corroborated with cross-sectional TEM of a deposited film. At a "low" deposition rate (~ 1 Å-

min^{-1}), an interfacial layer of predominantly TaC and some Ta oxide is observed. No metallic Ta is present. In contrast, Ta deposition at a "high" rate (~ 2 Å-sec^{-1}) results in the formation of a film of similar total thickness but which is predominantly metallic Ta in nature. The results suggest that the reaction/diffusion of Ta into the substrate competes with the growth of a continuous Ta overlayer.

Cu deposition on a metallic Ta overlayer results in conformal growth, as judged by the evolution of Cu($2p_{3/2}$) XPS intensity vs. deposition time. In contrast, Cu deposition onto a TaC/Ta oxide layer results in 3-d island growth. Annealing of Cu/Ta/Si-O-C interfaces in UHV up to 800 K produces no observable Cu diffusion or additional Ta/low-*k* interfacial reactions.

Experimental methods are discussed in section 2.2. In section 2.3, XPS results are presented for Ta deposition at low and at high deposition rates, and for the sputter deposition of Cu on Ta/Si-O-C substrates. The discussion is contained in section 2.4, while conclusions are contained in section 2.5.

2.2. EXPERIMENT

Experiments were performed in a combined UHV analysis/magnetron sputter deposition system shown in figure 2.1 (9). Working pressures were $1\text{-}5\times10^{-9}$ Torr in the analysis chamber and 10^{-8}-10^{-7} Torr in the sputter deposition chamber. Pressures in both chambers were monitored by nude ion gauges placed out of the line of sight from the sample. Pressures during plasma-induced sputter deposition were monitored with a baratron gauge. XPS spectra were obtained using an unmonochromatized Mg Kα X-ray source (Physical Electronics, PHI model 1427) operated at 15 kV and 300 W and a hemispherical analyzer (VG 100AX) operated at constant pass energy mode (50eV). Take-off angle resolved spectra were obtained by rotating the sample

60° off surface normal, relative to the analyzer. Calibration of the analyzer energy scale was carried out using sputter-cleaned Cu and Au samples according to established techniques (10). XPS data were analyzed using commercially available software (ESCA tools) and Shirley background subtraction. Shirley is an algorithm which assumes that the inelastic tail corresponding to each point in the spectrum is a step function extending from that point to zero kinetic energy. The height of the step function is proportional to the intensity at that point, after correcting for the background (11).

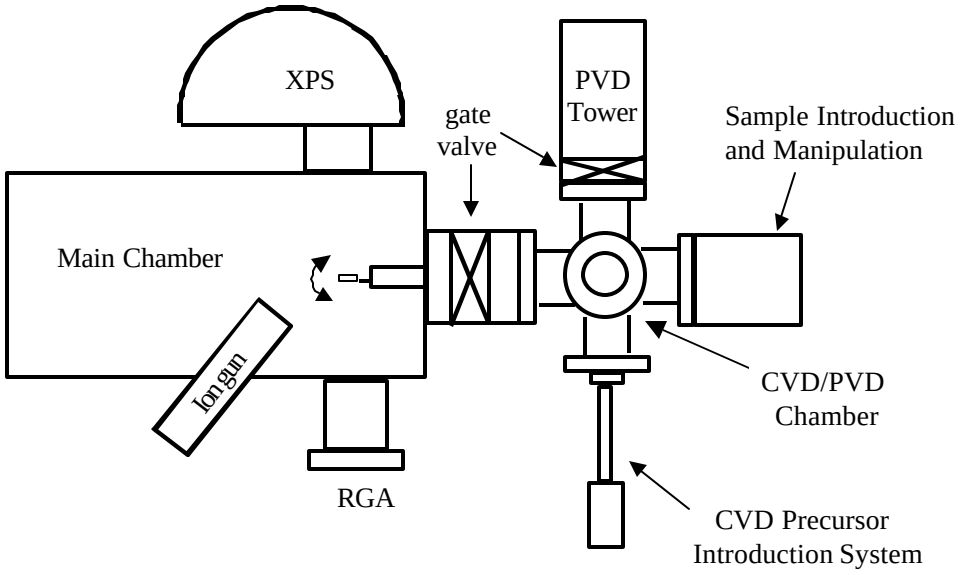

Fig.2.1 Combined XPS and DC Magnetron Sputtering Apparatus

Sputter deposition was carried out using a commercial water-cooled planar dual magnetron source (Minimak) and argon plasma with a pressure of 15 mTorr. Outgassing for the Si-O-C sample was carried out under UHV conditions at temperatures between 300-750 K. Ta was sputter deposited from a 99.999% purity target at different deposition rates of 1.2±0.2 Å-min^{-1} or 1.9±0.2Å-sec^{-1}, with the deposition rate modified by changing target-sample distance

and plasma power levels. Cu was deposited from an oxygen-free high conductivity (OFHC) Cu target at a rate of ~1Å-min^{-1}. All the depositions were performed at the room temperature.

The rate of metal deposition was in both cases calibrated by measuring the attenuation of the Si(2p) substrate signal, according to:

$$I = I_0 \exp(-d/\lambda) \qquad (2\text{-}1)$$

In (Eq.2-1) I and I_0 are the measured and initial absolute Si(2p) core level signal intensities, d is the thickness of the attenuating overlayer, and λ is the calculated electron inelastic mean free path (IMFP) for (in this case) a Si(2p) electron through SiC --25.7 Å (12). Absolute, rather than relative, Si(2p) intensities were measured. The error in the measurement of absolute intensities in this apparatus as been determined by experiment to be < 10%. The calculated film thickness was found to be proportional to deposition time for both low and high deposition rates. In this case, the use of an IMFP appropriate to SiC is an obvious approximation in the calculation of absolute film thicknesses and deposition rates. An additional assumption is that substrate Si will not be incorporated to any significant degree in the deposited Ta reactive layer. Therefore, a sputter deposited film was cross-sectioned and examined by TEM to corroborate estimated and actual film thicknesses and deposition rates. Cross-sectional Ta/Si-O-C interface structures were characterized by using a CM200 FEG transmission electron microscope (TEM). Cross sectional samples were prepared by standard methods.

The Si-O-C low-k material used in this study was provided by Sematech and consisted of a 1000Å thick film with dielectric constant below 2.7, grown on a SiO_2 wafer. Each wafer was cut into multiple pieces ~ 1 cm^2 for surface science studies. Samples were rinsed with deionized water prior to being mounted on a Ti sample holder in the vacuum system. A combination of liquid-nitrogen cooling and resistive heating of the sample holder permitted a variation of sample

temperature between 100 and 1300K. Temperatures were monitored by a K-type chromel – alumel thermocouple spot-welded at the edge of the sample holder.

2.3 RESULTS

2.3.1. Sample Composition Analysis

XPS spectra were acquired with the analyzer normal to the sample surface (normal emission) and at 60° with respect to surface normal (grazing emission). The compositions of the low-*k* films were calculated using the following equation:

$$C_x = \frac{I_x/SF_x}{\sum_i I_i/SF_i} \qquad (2\text{-}2)$$

where C is the number of atoms of the element x per unit volume, *I* is the intensity of photoelectron signal detected per second, and SF is the atomic sensitivity factor appropriate to the analyzer (13). Experimental results from the low-*k* material are shown in Table 2.1. The data indicate that the sample is a Si-O-C material with minor F and N contamination and a stoichiometry of $Si_{3.5}OC_{4.5}$. Annealing the sample in UHV at temperatures < 800 K revealed negligible changes in surface composition.

Table 2.1 Atomic compositions of Si-O-C substrates

Sample	T(K)	C%	Si %	O%	F%	N%
Surface Normal	300	46.27	36.24	10.31	3.34	3.84
60^0 grazing emission		46.54	31.26	14.24	3.90	4.06
Surface Normal	750	44.62	38.68	9.58	3.13	3.99
60^0 grazing emission		43.24	35.72	12.76	3.92	4.36

2.3.2. Ta Deposition

2.3.2.1 Ta Deposition Using a Low Deposition Rate (~1 Å-min^{-1})

Ta was sputter-deposited onto the Si-O-C film in sequential depositions of 4 min each using a low deposition rate (1.2±0.2 Å-min^{-1}). Fig.2.2 (a-d) displays the Si(2p), O(1s), C(1s) and Ta(4f) XPS spectra before and after 32 minutes Ta deposition (average total thickness ≈ 36Å). The observed binding energies were affected by sample charging during acquisition, which is common in XPS studies of insulating materials. The Si(2p) binding energy of Si-C was set to 100.5 eV (14) and used as a reference for the calibration of other peak positions. After 32 minutes Ta deposition, the total Si(2p) signal (Fig.2.2a)is significantly attenuated, and no change in peak width is observed, indicating negligible Si reaction during the deposition process. In contrast, the O(1s) signal (Fig. 2.2b) exhibits a significant increase in intensity, and a shift in binding energy from 532.1 eV, characteristic of SiO_2 (15) to 530.7eV, attributable to Ta oxide formation (16). The experimental C(1s) spectrum of the clean Si-O-C (Fig.2.2c, bottom) is well fit with a FWHM of 2.2eV at binding energies of 283.3eV and 284.7eV, consistent with Si-C (14) and C-C (10) bonding environments, respectively. Ta deposition (32 min, 1 Å-min^{-1}) results in the formation of a new feature at a lower binding energy of 282.4eV (Fig.2.2c, top), which indicates Ta-C formation (17). Additionally, the total C(1s) intensity is significantly attenuated by the Ta deposition, but to a lesser degree than is the Si(2p) intensity. Fig.2.2d (top) indicates that the deposition process has resulted in the formation of a broad Ta(4f) feature. The Ta(4f) spectra include both the Ta($4f_{7/2}$) and the Ta($4f_{5/2}$) photoelectron lines, which are present in a 4:3 intensity ratio, respectively, with a 1.9 eV separation (10). Each doublet is well fit with a FWHM of 2.2 eV for each component. The decomposition of the features into individual TaC(23.3 eV)(18), Ta suboxide(24.8 eV) (19) and Ta_2O_5(26.7 eV)(20) is a complex process. The

observed spectrum, however, indicates an absence of metallic Ta, which would exhibit a feature at 22.1 eV binding energy (10).

The change in Ta(4f)/O(1s), Ta(4f)/C(1s) and Ta(4f)/Si(2p) intensity ratios with Ta deposition time at 1 Å-min^{-1} (the uptake curve) is shown in Fig.2.3. Also displayed in figure 2.3 is the surface charging, as indicated by the difference in binding energy of the observed Si substrate peak and the literature value of 100.5 eV(14). A significant decrease in surface charging after t=16 min deposition indicates the formation of a continuous layer of conductive or moderately conductive material. No metallic Ta is observed in the Ta ($4f_{7/2}$) XP spectrum (Fig.2.2d, top), therefore the decrease of charging could not be due to the Ta layer itself. Since Ta_2O_5 is insulating, the formation of TaC is possible. The possibility of TaC formation is also inferred from the position of 23.3 eV in Ta(4f) corresponding to TaC formation(18) and from the formation of a new feature at 282.4 eV in the C(1s) spectrum (Fig.2.2c). Further evidence of TaC formation is the preferential attenuation of the Si(2p) intensity compared to the C(1s) intensity shown in Fig. 2.3 (i.e., the Ta/Si intensity ratio increases more quickly with Ta deposition time than the Ta/C ratio). This behavior is not attributable to mean free path effects since the Si(2p) photoelectron kinetic energy is higher than that of the C(1s) photoelectron kinetic energy, resulting in a longer escape depth for the Si(2p) photoelectron vs. the C(1s). Similar considerations apply to the Si(2p) vs. O(1s) photoelectron intensities. If the Si, O and C core level signals were being attenuated by a Ta overlayer, one would expect more rapid attenuation of the C(1s) and O(1s) signals than of the Si(2p) signal. i.e., Ta/C and Ta/O atomic ratios would increase more quickly than Ta/Si ratio. However, the data yield the opposite result. (Fig. 2.3). Ta oxides as well as Ta carbides are incorporated in the growing film, as the evolution of the Ta(4f)/O(1s) signal intensity vs. Ta deposition time is comparable to that of the Ta(4f)/C(1s)

intensity ratio. The Ta(23.3 eV)/C(282.4 eV) atomic ratio is calculated as 1.4. The data in Fig.2.2 and Fig.2.3 therefore indicate the interaction of sputter deposited Ta on a Si-O-C substrate results in the formation of a layer primarily composed of TaC and oxidized Ta species.

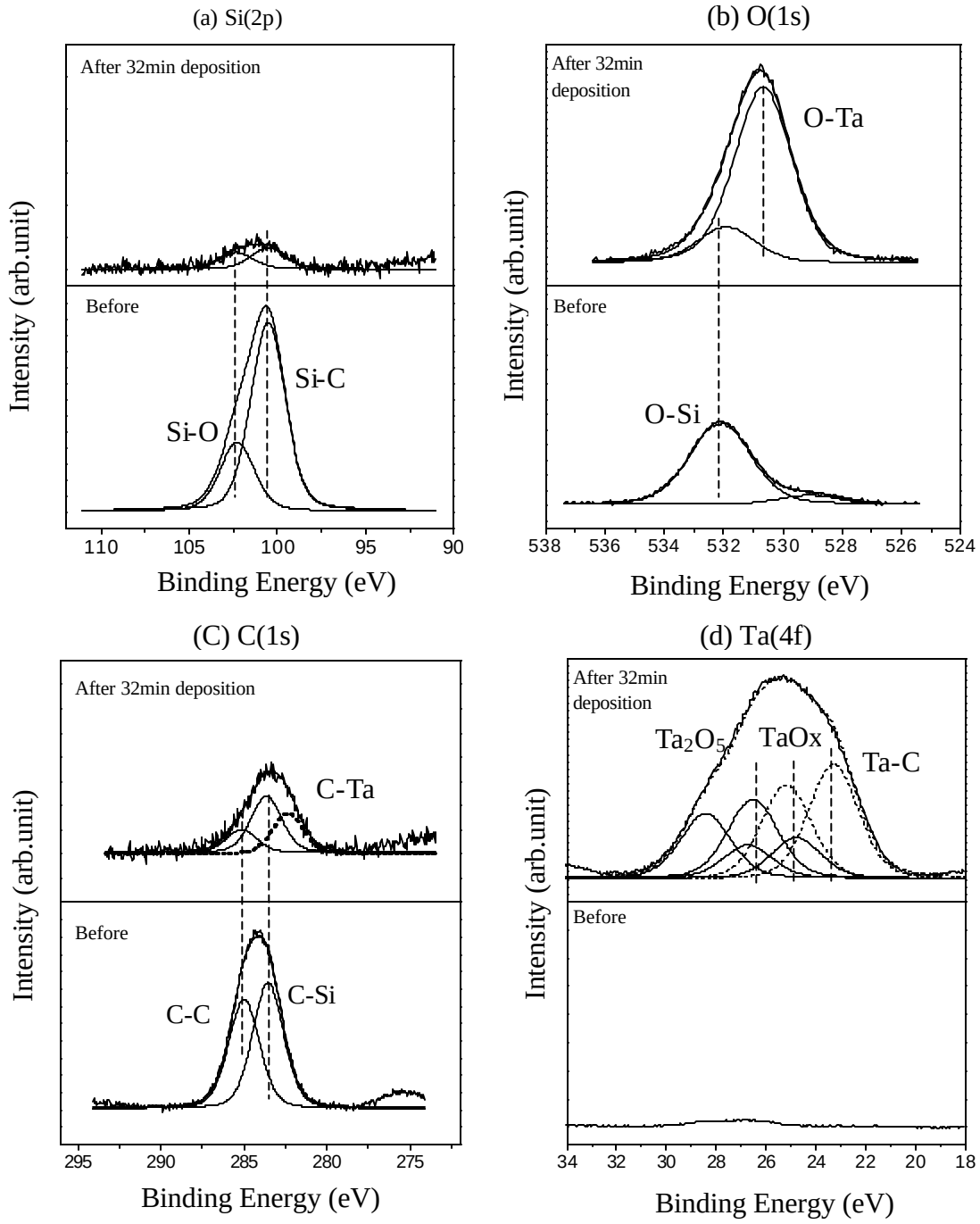

Fig. 2.2 XPS spectra for clean Si-O-C substrate and after 32minutes Ta deposition on Si-O-C at 300K by using a low deposition rate ~1 Å-min^{-1}. (a) Si(2p); (b)O(1s); (c)C(1s); (d)Ta(4f).

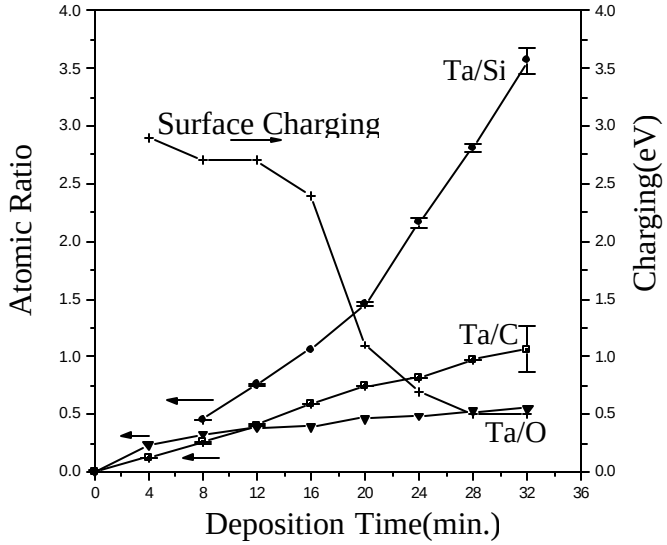

Fig. 2.3 XPS atomic ratios (Ta/Si, Ta/C and Ta/O) and surface charging as a function of Ta deposition time on Si-C-O substrate at a deposition rate of ~1 Å-min^{-1}.

2.3.2.2 Ta Deposition Study on Si-O-C by Using a Higher Deposition Rate (~2 Å-sec^{-1})

By decreasing the distance between the sample and the sputtering target, and altering plasma conditions to maintain a steady discharge, a consistent Ta deposition rate of 1.9±0.2 Å-sec^{-1} was achieved. XPS core level spectra are displayed in Fig.2.4(a-c) for the Ta film resulting from 15 sec deposition at the higher rate (average total thickness ≈35Å). The film is roughly the same thickness as that deposited by 32 minutes deposition time at the lower Ta deposition rate (average thickness ≈36Å). A comparison of the Ta(4f) spectra (Fig.2.5) for the two films indicates that the film deposited at the higher deposition rate has a prominent feature at 22.1 eV, due to metallic Ta, whereas no metallic Ta is observable for the film deposited at the lower deposition rate. Furthermore, TaC appears to comprise a higher relative proportion of the total deposited Ta for the film deposited at a low Ta deposition rate. The relative percentage of total Ta intensity attributable to TaC is summarized in Table 2.2 for films of approximately equal average thickness (~30 Å) deposited at 1 Å-min^{-1} vs. 2 Å-sec^{-1}. Results are shown for spectra

acquired at both normal take-off angle and grazing take-off angle. Conclusions based on such data are limited by the unknown roughness of the surface compared to Si or SiO_2, but the data indicate that TaC comprises a substantially greater percentage of total Ta in the film deposited at the lower deposition rate. Further, in the film deposited at the lower deposition rate, the relative TaC composition is enhanced at grazing takeoff angle, while in the film deposited at the higher Ta deposition rate, there is no difference in relative TaC composition at normal vs. grazing take-off angle. Ta(4f) XPS spectra are displayed in Fig. 2.6 for films deposited at the higher rate for 15 sec (~ 30 Å thick) vs. 120 sec (~240 Å thick). The data demonstrate that deposition for longer time at this rate results in the formation of metallic Ta, and the attenuation of signal from carbide or oxide species. Annealing of the thicker Ta film in UHV up to 800 K for a period of 30 minutes resulted in only a slight broadening of the Ta(4f) spectrum (not shown), undoubtedly due to reaction with residual H_2O or O_2 gas in the chamber. No other changes were observed by XPS.

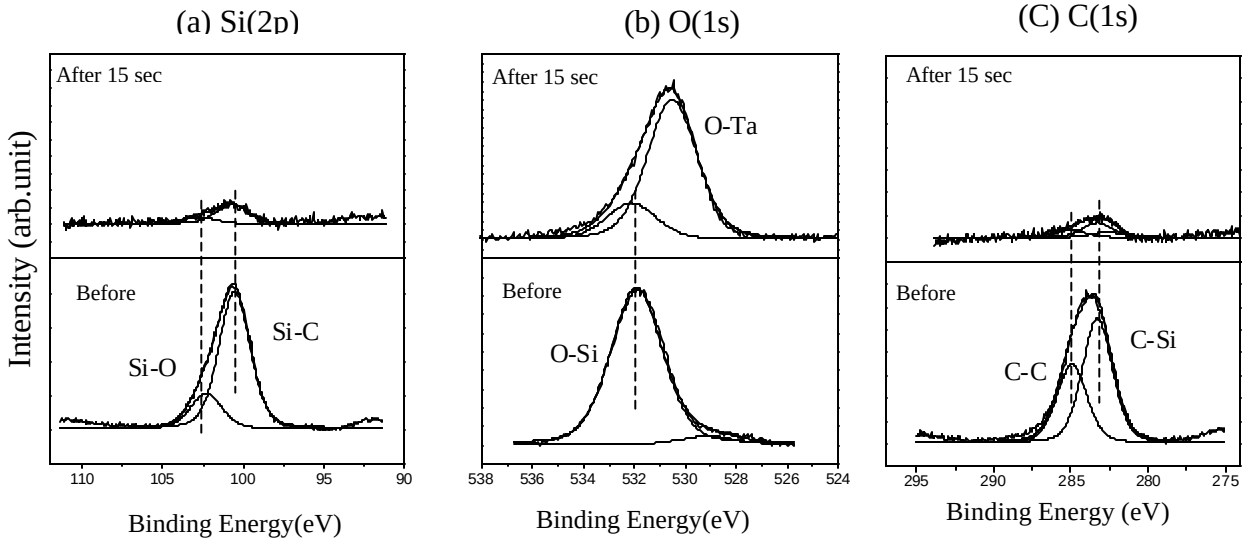

Fig. 2.4 XPS spectra for clean Si-O-C substrate and after 15 sec Ta deposition on Si-O-C at 300K by using a high deposition rate ~2 Å-sec^{-1}. (a) Si(2p); (b)O(1s); (c)C(1s).

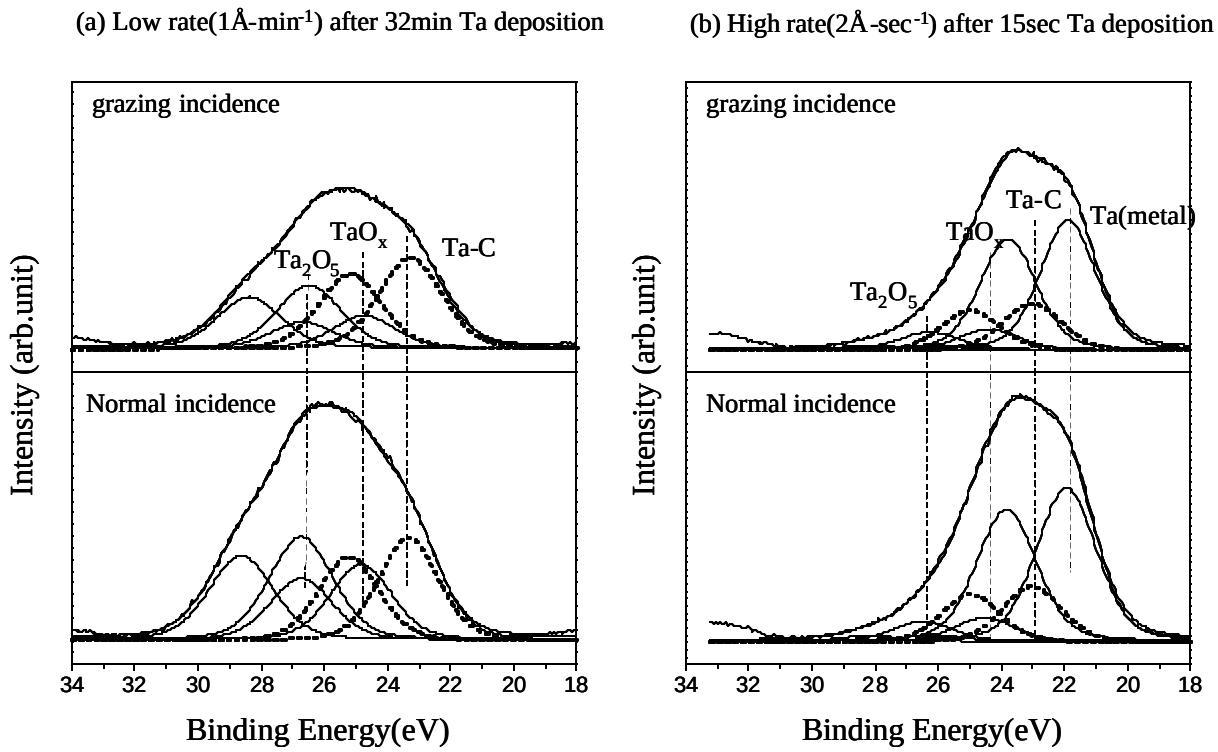

Fig. 2.5 Ta(4f) spectra acquired at normal and grazing emission for Ta/Si-O-C films of similar average thickness but deposited at different deposition rates: (a)after 32 minutes deposition(1 Å-min^{-1}); (b) after 15 sec deposition(~2 Å-sec^{-1}).

Table 2.2 $Intensity_{Ta\text{-}C}$ / $Intensity_{total\ Ta}$ ratios for Ta deposition at different rates

	after 32 min at 1 Å-min^{-1}	after 15 sec at 2 Å-sec^{-1}
Normal emission	0.35	0.24
60º grazing emission	0.49	0.23

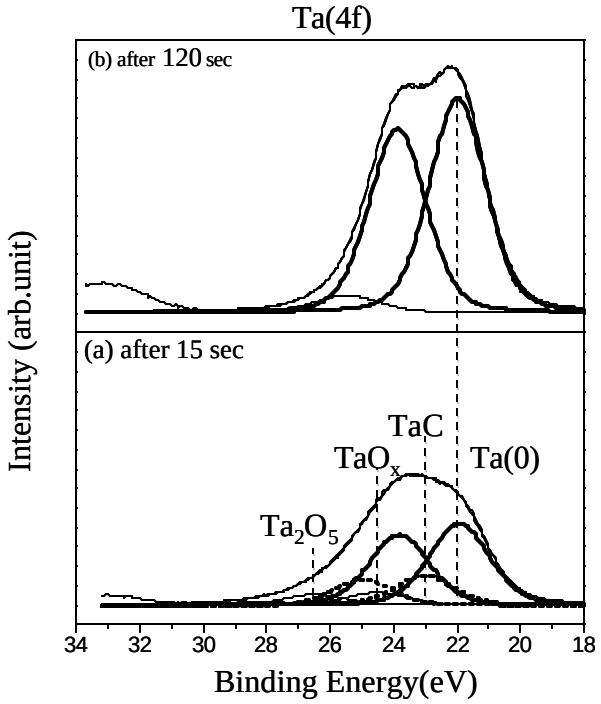

Fig. 2.6 Ta(4f) XPS spectra after Ta deposition at a rate of ~2 Å-sec^{-1}: (a) after 15 sec deposition; (b) after 120 sec deposition.

2.3.2.3 TEM Results for Ta Deposition Study on Si-O-C by Using a Higher Deposition Rate (~2 Å-sec^{-1})

In order to more accurately calibrate the thicknesses of the deposited films as estimated from XPS data, a cross-sectional sample of a film deposited at the higher deposition rate for 120 sec was analyzed by TEM. The TEM image is shown in Figure 2.7. The results indicate that the cross-sectioned film has a total thickness of 240 Å-260 Å (the topography is rough), in very good agreement with estimates from sputtering rates derived from attenuation of Si(2p) XPS signal during Ta deposition. The degree of agreement between the TEM data and the thickness estimated from XPS–derived sputtering rates indicates that the assumptions made in calculating film thickness based on XPS data (no incorporation of Si into the growing film, and an electron

inelastic mean free path appropriate to SiC) are valid. The TEM shows the existence of a continuous light gray layer approximately 40 Å thick on top of a thick darker layer which is evidently inhomogeneous. The light gray surface film is Ta oxide, formed by exposure of the sample to air prior to TEM sample preparation and imaging. The darker gray region has a higher Ta content, consistent with Ta formation. The inhomogeneities evident in the dark gray region are consistent with a polycrystalline material. The boundary between the darker Ta–rich layer and the Si-O-C substrate is marked by a thin light gray region, which may indicate some Ta diffusion into the substrate, but could also be induced by the sample preparation procedure.

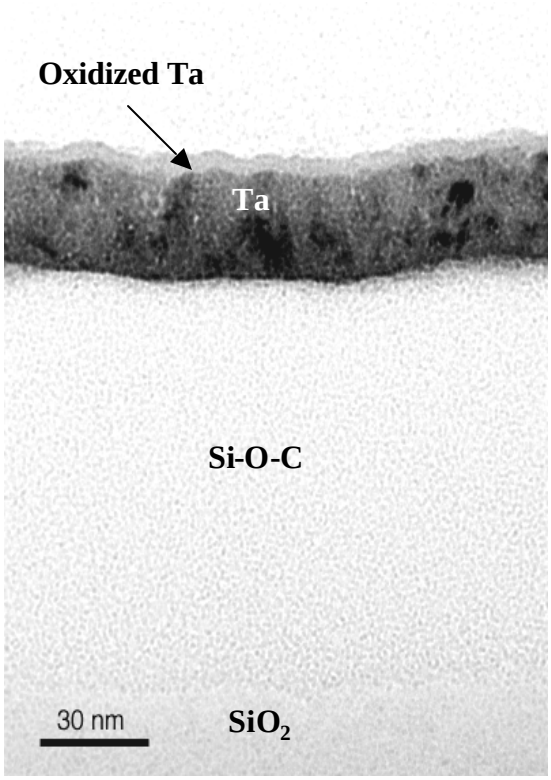

Fig. 2.7 Cross-sectional TEM image of a thick Ta/Si-O-C sample

2.3.3. Cu Growth Mode on Ta Film on Si-O-C

In order to characterize Cu interaction with Ta/Si-O-C films, Cu was sputter deposited onto two different substrates: a "thick" Ta/Si-O-C film formed by 120 sec deposition of Ta at a rate of ~2 Å-sec^{-1}; and a "thin" film formed by 15 sec Ta deposition at the same rate. As discussed above, the thick film consisted only of metallic Ta, while TaC and Ta oxide species were detected by XPS of the thin Ta film. The Cu sputter deposition rate was 1 Å-min^{-1} as determined by the attenuation of the Ta(4f) XPS signal intensity during Cu deposition onto a Ta foil substrate.

Cu was deposited sequentially at sputtering times of one minute. After each deposition, the sample was transferred from the sputter deposition chamber to the UHV chamber for XPS analysis, and then back to the sputter deposition chamber for additional deposition. The growth mode of the sputter deposited Cu on the substrate can be characterized by plotting the increase in the Cu($2p_{3/2}$) intensity (relative to Ta ($4f_{7/2}$)) ratio as a function of deposition time (shown in Fig.2.8).

For the thick Ta film, the uptake curve exhibits linear behavior with a change in slope at 2 minutes deposition time, which indicates the conformal growth of Cu (21). Ta/Cu XPS intensity error bars arising from the deviations from the average of the intensities are determined to be less than 5%. The surface thickness of Cu (d_{Cu}) present at the break in the uptake curve is estimated from Eq.2.1, where λ_{Ta} is the mean free path length for Ta (4f) —20.2 Å (12). The calculated d_{Cu} is ~2.5 Å, which is close to the atomic diameter of Cu (2.6 Å) (21). For Cu deposition on the thin Ta film, no break in the uptake curve is observed, consistent with non-wetting (3-D island formation).

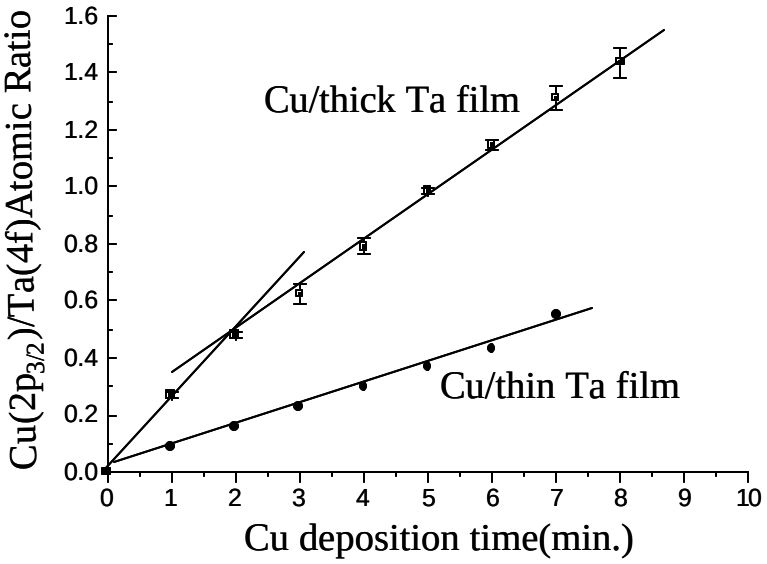

Fig. 2.8 Variation of $Cu(2p_{3/2})/Ta(4f)$ intensity ratio with Cu deposition time on a "thick" Ta/Si-O-C substrate (120 sec Ta deposition at 2 Å-sec^{-1}) compared to Cu deposition on a "thin" Ta/Si-O-C substrate (15 sec Ta deposition at 2 Å-sec^{-1})

2.3.4.Thermal Stability of Cu/Ta/Si-O-C Interface

Cu was sputter deposited at 300 K onto a thick (120 sec Ta deposition at 2 Å-sec^{-1}) Ta/Si-O-C substrate until an average Cu thickness of 8Å was achieved. Cu was similarly deposited onto a thin (15 sec at 2 Å-sec^{-1}) Ta/Si-O-C film. Each Cu/Ta/Si-C-O sample was annealed in UHV in 100K increments starting from 300K to 800K at a period of 30 minutes for each temperature. The Cu/Ta/Si-O-C sample was then cooled down to room temperature to allow for XPS measurement. The $Cu(2p_{3/2})/Ta(4f_{7/2})$ and $Cu(3p)/Cu(2p_{3/2})$ intensity ratios are presented as a function of annealing temperature in Fig.2.9. A decrease in the Cu/Ta intensity ratio could result from either Cu diffusion into the substrate, or dewetting from the Ta surface (formation of 3-D Cu islands). A useful method for examining Cu diffusion consists of plotting the $Cu(3p)/Cu(2p_{3/2})$ intensity ratio as a function of temperature. (The total Cu(3p) intensity is used

here, due to the failure to fully resolve the 3/2-1/2 spin orbit splitting under these experimental conditions.) The inelastic electron mean free paths in the Ta film for the Cu($2p_{3/2}$) and Cu(3p) transitions are calculated to be 15.9 Å and 38.8 Å(12), respectively. Therefore, the onset of substantial diffusion of Cu into the substrate film—enough to affect XPS signal intensities—would be marked by a preferential attenuation of the more surface-sensitive Cu($2p_{3/2}$) transition. Such a measurement of Cu diffusion is certainly less sensitive than appropriate electrical measurements, since typical XPS sensitivities are ~ 10^{13} atoms-cm^{-2}. Such measurements can, however, indicate whether apparent decreases in relative Cu($2p_{3/2}$) signal intensity are due to Cu agglomeration on the surface or diffusion away from the surface region. The degree of attenuation (At) of a XPS signal of Cu that is covered by an overlayer of thickness d can be calculated using the following equation:

$$At = 1 - I/I_0 \qquad (2\text{-}3)$$

where I/I_0 is defined in Eq.2-1. If Cu is covered by a 10 Å overlayer after it has diffused into the Ta films, the Cu($2p_{3/2}$) and Cu(3p) signals are attenuated by ~46.7% and ~22.7%, respectively. Thus, significant Cu diffusion into the bulk would be indicated by a decrease in the Cu($2p_{3/2}$) /Ta(4f) ratio and an increase in the Cu(3p)/Cu($2p_{3/2}$) ratio. On the other hand, a decrease in the Cu($2p_{3/2}$) /Ta(4f) ratio with little or no change in the Cu(3p)/ Cu($2p_{3/2}$) ratio would indicate that the change in relative Cu/Ta intensities is due primarily to dewetting (23, 24).

For 8 Å of Cu on a thick Ta(240 Å) interface (Fig.2.9a), a stable Cu(3p)/Cu($2p_{3/2}$) is observed for the temperature range of 300-800K. The Cu($2p_{3/2}$)/Ta($4f_{7/2}$) atomic ratio remains stable from 300K to 600K and begins to decrease monotonically at higher temperatures. Therefore, the decrease in the Cu/Ta ratio in this region is attributed to Cu de-wetting. De-wetting of Cu at 600 K has previously been observed for multilayer coverage of Cu on clean Ta

foil(25) and is attributable to the formation of 3-D Cu islands on top of an interfacial Cu layer strongly bound to Ta. For Cu on the thin Ta film (30 Å, Fig.2.9b), the $Cu(2p_{3/2})/Ta(4f)$ ratio starts to decrease at 400K. Since the $Cu(3p)/Cu(2p_{3/2})$ does not change significantly during the annealing period, it demonstrates the Ta oxidation and carbide formation enhance the tendency of Cu to agglomerate on this surface. In both cases, diffusion of Cu into the bulk was not observed up to 800K.

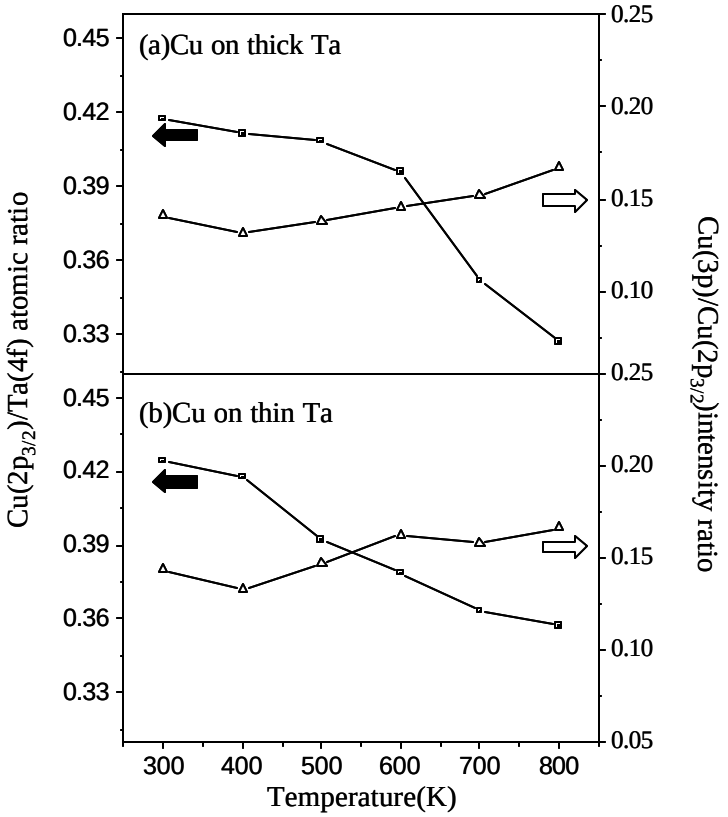

Fig. 2.9 Variation of XPS-derived $Cu(2p_{3/2})/Ta(4f_{7/2})$ atomic ratio and $Cu(3p)/Cu(2p_{3/2})$ intensity ratio with annealing temperature for a 8 Å average thickness Cu overlayer on (a) thick Ta film (120 sec Ta deposition at 2 Å-sec^{-1}); (b) thin Ta film (15 sec Ta deposition at 2 Å-sec^{-1}). The filled squares and open triangles represent the $Cu(2p_{3/2})/Ta(4f_{7/2})$ atomic ratio and the $Cu(3p)/Cu(2p_{3/2})$ intensity ratio, respectively.

2.4. DISCUSSION

The data presented here demonstrate that sputter deposited Ta will react with a Si-O-C substrate to form both Ta oxide and Ta carbide. The extent of this interfacial reaction region, however, is strongly affected by the rate of Ta deposition. Deposition at a rate of 1 Å-min^{-1} (after 32 minutes deposition time) results in a film consisting of both Ta-oxide and TaC (Fig. 2.2). The Si(2p) signal is rapidly attenuated by continued Ta deposition, while the Ta/C and Ta/O intensity ratios increase only slowly (Fig. 2.3). Since the Si(2p) photoelectron mean free path is longer than that of C(1s) or O(1s), the slower change in the Ta/C and Ta/O intensity ratios indicates carbon and O incorporation in the growing film, but not Si. This Ta oxide/TaC layer is ~ 30 Å average thickness, based on the attenuation of the Si(2p) substrate signal. While a Ta-oxide film of this thickness could be ascribed to oxidation of deposited Ta during prolonged periods in the sputter deposition chamber, this does not explain the formation of a TaC film of such a thickness. (No carbide formation was observed as a result of prolonged sample residence in the introduction chamber.) Since the prospect of diffusion of TaC through Ta at 300 K is unlikely, the formation of a TaC layer of 30 Å average thickness must be ascribed either to a highly irregular and convoluted topography for this Si-O-C surface, or to significant mass transport within the interfacial region during the Ta deposition/reaction process. If a convoluted topography were the only explanation, however, Ta deposition would result in a similar evolution of the Ta(4f)/C(1s) and Ta(4f)/Si(2p) intensity ratios during the Ta deposition process. The data in Fig. 2.3 demonstrate that this is certainly not the case, and one must therefore conclude that TaC formation does not occur simply at the surface of the substrate film, but involves mass transport—either Ta diffusion into the substrate or the movement of Si-O-C components from the bulk to the reaction region—during the Ta deposition and reaction process.

Deposition of Ta at a rate of 2 Å-sec^{-1} results in a film of thickness similar to that deposited at the slower rate, but predominantly metallic Ta, and with a lower relative TaC content than the film deposited at the slower rate (Fig. 2.5, Table 2.2). The lower Ta oxide content of the film deposited at the faster rate is consistent with a shorter time of exposure to trace amounts of O_2 or H_2O in the sputter deposition chamber. This alone would not, however, account for the much smaller proportion of TaC to total Ta ($I_{TaC}/I_{Ta\ total}$) observed for the film deposited at the higher rate. The data in Fig.4b indicate that during Ta deposition, (at least) two competing processes occur: Ta reaction with C sites to form TaC; and the formation of a metallic Ta ad-layer. The constant value of $I_{TaC}/I_{Ta\ total}$ at both grazing and normal takeoff angles for the film deposited at the higher rate (Table 2.2) demonstrate that TaC is present at the surface of the film, as well as in the sub-surface region, and this is corroborated by the fact that PVD Cu will not wet this film at 300 K (Fig.2.8) or resist agglomeration even at mildly elevated temperatures (Fig. 2.9b)—expected behavior for Cu on a TaC surface (25). As Ta deposition continues, isolated Ta nuclei and coalesce to form a continuous film, blocking any further reaction between depositing Ta adatoms and carbon sites at the substrate. Once the continuous Ta overlayer is formed, further Ta deposition results in the growth of a metallic Ta layer on top of the carbide layer, as evidenced by the data in figure 2.6b. The Ta(4f) of TaC signal from the thicker film is highly attenuated, as is the corresponding C(1s) signal (not shown).

The formation of a Ta oxide/carbide reaction layer for Ta sputter deposited onto a carbon-containing low dielectric constant substrate at 300 K has significant implications for Cu/low-*k* integration. In order to form an adherent, thermally stable interface, the Ta substrate should be free of carbides and oxides, as demonstrated by the wetting and thermal stability of sputter-deposited Cu on Ta/Si-O-C films (Figs. 2.8 and 2.9). The thickness of this Ta

oxide/carbide reaction layer is at least 30 Å under the fastest deposition rate (2 Å-sec^{-1}) employed here, and indicative of the occurrence of mass transport during TaC formation. Therefore, the minimum thickness of a Ta layer on a carbon-containing low-dielectric material would seem to be at least 30 Å and perhaps much more, depending upon such factors as the porosity and density of the dielectric material.

It is of practical interest to compare the thermal stability of the Cu/Ta/Si-O-C interface (Fig. 2.9) with recently published (26) XPS results for Cu interaction with ultrathin silicate films formed by Ta interaction with SiO_2 substrates, or by oxidation of TaSi surfaces (9). The thermal stability of the Cu/Ta-silicate interface is limited to < 900 K in UHV conditions, due to the decomposition of the Ta silicate layer (26). In contrast, electrical (sheet resistance) measurements (27, 28) of Cu/Ta/SiO_2 annealed under oxygen-free conditions indicate a limiting temperature for interfacial stability of ~ 923 K (650° C). Above this temperature, interlayer diffusion and oxide formation result degradation of the Cu sheet resistance. The thermal stability becomes rather more limited (< 673 K) in the presence of a low partial pressure (< 10^{-2} mbar) of oxygen, due to interlayer oxidation (8). The correspondence between XPS (26) and sheet resistance (27, 28) indicates that the Cu/Ta/SiO_2 interface is more stable against thermal annealing than the Cu/Ta/Si-O-C interface characterized in this report, but that the thermal difference (~800 K vs. 900 K as a rough thermal limit) is hardly overwhelming, particularly since many low-dielectric constant materials may exhibit thermal decomposition or other changes in mechanical properties in this temperature range. Neither XPS nor sheet resistance measurements, however, directly sample the diffusion of small amounts of Cu into the bulk dielectric substrate, and detailed current-voltage and capacitance-voltage measurements would be of interest in this respect.

2.5 SUMMARY AND CONCLUSIONS

XPS data demonstrate that Ta sputter-deposited onto a Si-O-C containing low dielectric constant substrate forms a reaction layer composed of Ta oxide and TaC, but not Ta silicides. The composition of the reaction layer varied with deposition rate (1 Å-min^{-1} vs. 2 Å-sec^{-1}), but in both cases, the thickness of the TaC layer was found to be at least 30 Å on the basis of XPS spectra. Sputter-deposited Cu will not wet the TaC layer and displays facile agglomeration, even at 400 K. Deposition for longer time at 2 Å-sec^{-1} results in formation of a metallic Ta layer. Sputter deposited Cu wets (grows conformally) the metallic Ta surface at 300 K, and resists significant agglomeration at up to ~ 600 K. Cu diffusion into the substrate is not observed up to 800 K in the UHV environment.

2.6 CHAPTER REFERENCES

(1) Stavrev, M.; Fischer, D.; Preub, A.; Wenzel, C.; Mattern, N. *Microelectronic Eng.* **1997,** *33*, 269.

(2) Holloway, K.; Fryer, P. M. *Appl. Phys. Lett.* **1990,** *57*, 1736.

(3) Kaloyeros, A. E.; Eisenbraun, E. *Annu. Rev. Mater. Sci.* **2000,** *30*, 363.

(4) Wu, Y.; Garfunkel, E.; Madey, T. E. *J. Vac. Sci. Technol.* **1996,** *A 14*, 1662.

(5) Baumer, M.; Freund, H.-J. *Progress in Surface Science* **1999,** *61*, 127.

(6) Chen, L.; Ekstrom, B.; Kelber, J. *Mat. Res. Soc. Symp. Proc*. **1999**, 511, 287, Materials Research Society, San Francisco, CA, Spring 1999

(7) Lee, Y. K.; Latt, K. M.; JaeHyung, K.; Osipowicz, T.; K.Lee *Mater. Sci. Eng.* **1999,** *B68*, 99.

(8) Yin, K.-M.; Chang, L.; Chen, F.-R.; Kai, J.-J.; Chiang, C.-C. *Thin Solid Films* **2001,** *388,* 27.

(9) Shepherd, K.; Kelber, J. *Appl. Surf. Sci.* **1999,** *151*, 287.

(10) Moulder, J. F.; Stickle, W. F.; Sobol, P. E.; Bomben, K. D. *Handbook of X-ray Photoelectron Spectroscopy*; Physical Electronics: Eden Prarie, 1992.

(11) Slaughter, J. M.; Weber, W.; Guntherodt, G.; Falco, C. M. *MRS Bulletin* **1992,** *December,* 39.

(12) Powell, C. J.; Jablonski, A.; Tilinin, I. S.; Tanuma, S.; Penn, D. R. *J. Electr. Spectrosc. Relat. Phenom.* **1999,** *98-99,* 1.

(13) Seah, M. P. In *Auger and X-ray Photoelectron Spectroscopy*; Briggs, D., Seah, M. P., Eds.: New York, 1990; Vol. 1, pp 201.

(14) Chourasia, A. R. *Surf. Sci. Spec.* **2001,** *8,* 45.

(15) Sprenger, D.; Bach, H.; Meisel, W.; Gutlich, P. *J. Non-cryst. Solids* **1990,** *126*, 111.

(16) Thomas, J. H.; Hammer, L. H. *J. Electrochem. Soc.* **1989,** *136,* 2004.

(17) Kim, K. S.; Jang, Y. C.; Kim, H. J.; Quan, Y.-C.; Choi, J.; Jung, D.; Lee, N.-E. *Thin Solid Films* **2000,** *377-378,* 122.

(18) Ramqvist, L.; Hamrin, K.; Johansson, G. *J. Phys. Chem. Solids.* **1970,** *31*, 2669.

(19) Atnassova, E.; Spassov, D. *Appl. Surf. Sci.* **1998,** *135,* 76.

(20) Nefedov, V. I.; Firsov, M. N.; Shaplygin, I. S. *J. Electron Spectrosc. Relat. Phenom.* **1982,** *26,* 65.

(21) Ekstrom, B. M.; Lee, S.; Magtoto, N.; Kelber, J. A. *Appl. Surf. Sci.* **2001,** *171*, 275.

(22) http://*www.webelements.com*.

(23) Tong, J.; Martini, D.; Magototo, N.; Pritchett, M.; Kelber, J. *Appl. Surf. Sci.* **2002,** *187,* 253.

(24) Chen, J. G.; Coloanmi, M. L.; Weinberg, W. H.; Yates, J. T. *Surf. Sci.* **1992,** *279,* 223.

(25) Chen, L.; Magtoto, N.; Ekstrom, B.; Kelber, J. *Thin Solid Films* **2000,** *376,* 115.

(26) Zhao, X.; Magtoto, N. P.; Leavy, M.; Kelber, J. A. *Thin Solid Films* **2002,** *415,* 308.

(27) Li, S.; Dong, Z. L.; Latt, K. M.; Park, H. S.; White, T. *Appl. Phys. Lett.* **2002,** *80,* 2296.

(28) Latt, K. M.; Lee, Y. K.; Osipowicz, T.; Park, H. S. *Materials Science & Eneineering B* **2002,** *94*.

CHAPTER 3

TETRAKIS(DIETHYLAMIDO) TITANIUM (TDEAT) INTERACTIONS WITH SiO_2 AND COPPER SUBSTRATES

3.1. INTRODUCTION

Titanium nitride films have been widely employed as diffusion barriers in semiconductor manufacturing due to the material's characteristic properties: high thermal stability, low resistivity and good adhesion to Si and SiO_2 films (1, 2). TiN is commonly deposited by physical vapor deposition (PVD) methods (3). The continual shrinkage of ULSI circuits, however, has greatly increased interest in chemical vapor deposition (CVD), in order to achieve good conformal coverage. Much effort has been devoted toward CVD of TiN using $TiCl_4$ and NH_3, but several issues limit the application of $TiCl_4$, including high deposition temperature (> 600°C) and Cl incorporation in the film (4, 5). Currently, considerable attention is being focused on various tetraamido titanium MOCVD precursors, including tetrakis(dimethylamido) titanium (TDMAT) (6, 7) and tetrakis(diethylamido) titanium (TDEAT) (8). TDEAT has been found to have a higher deposition effiency and slower reaction kinetics than the related TDMAT compounds. The lower reactivity of TDEAT due to the steric bulk of the ethyl ligands leads to improved conformality (9, 10).

The mechanism of TDEAT decomposition, initially proposed by Fix, et al (11), and confirmed by FTIR gas phase measurements (12) is shown schematically in figure 3.1. In the absence of ammonia, decomposition occurs by β-hydride elimination (Fig.3.1(a)) followed by titanium insertion into a carbon-hydrogen bond to form a metallocycle (Fig.3.1(b)). The latter process may account for the increase in carbon content observed (13) for films deposited in the absence of NH_3. In the presence of NH_3, Dubois (12) confirmed that NH_3 could alter the reaction

chemistry by transaminating the metal complex (Fig.3.1(c)). Ti-amino oligomers can form in the gas phase (12) (Fig.3.1(d)), and these may degrade CVD step coverage and selectivity. Studies of $Ti(NR_2)_4/NH_3$ interaction at reactive, oxide-free, metal surfaces have been carried out under UHV conditions (6). Those studies showed that transamination reactions occur at such surfaces, and that the absence of NH_3 can result in carbide formation.

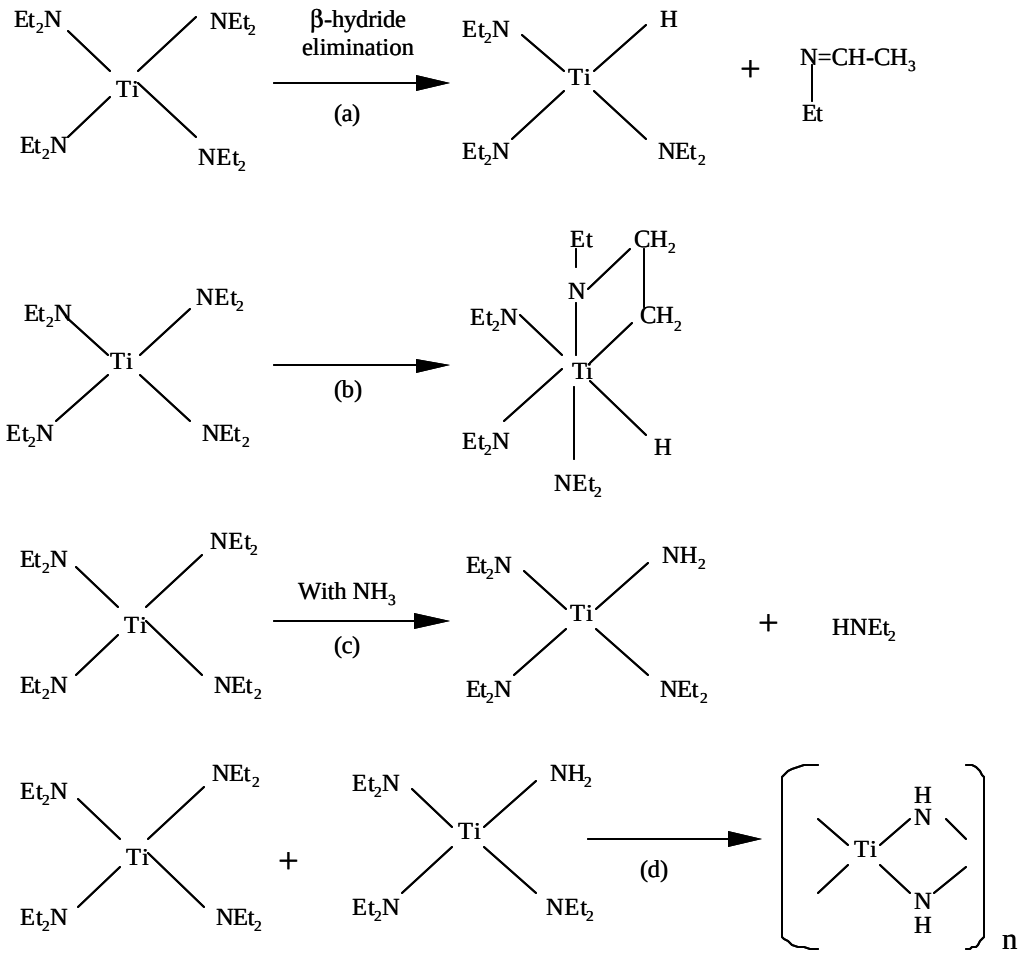

Fig. 3.1 Decomposition pathways for TDEAT. (a) β-hydride elimination; (b) Ti-C bond formation in the absence of NH_3; (c) transamination process in the presence of NH_3; (d) oligomers formation in the gas phase.

Current MOCVD processes using TDEAT deposition involve moderate to atmospheric pressure (14, 15), where the process is driven by rapid reactions in the gas phase. Although a high pressure CVD process is desirable for high deposition rate, extensive reactions can result in undesirable side effects, such as particle formation and poor conformality. In addition, there has been little direct investigation of TDEAT interactions with SiO_2 or Cu surfaces, even though such chemistry may critically impact film nucleation and adhesion. The purpose of this work is therefore to study the interactions of TDEAT with SiO_2 and with Cu surfaces under controlled ultra-high vacuum (UHV) conditions, where gas-phase chemical reactions may be neglected. The products of precursor/substrate interactions (in the presence or absence of NH_3) have been characterized by using X-ray photoelectron spectroscopy (XPS).

3.2. EXPERIMENT

Experiments were carried out in a surface analysis system (Fig. 3.2) that has been described previously in detail (16). The base pressure of the UHV chamber was 3×10^{-10} Torr after bakeout, and working pressures were in the 5×10^{-10} Torr – 5×10^{-9} Torr range. Chamber pressure was monitored by a nude ion gauge placed out of the line of sight from the sample. XPS spectra were acquired using a commercial hemisphere analyzer equipped with a mutichannel plate detector. MgK_α X-ray radiation was obtained from a commercial, unmonochromatized dual anode X-ray source operated at 15 kV and 300 W. XPS spectra were acquired in constant pass energy mode (22.5 eV), with the sample aligned normal to the analyzer lens axis (normal emission) and at 60^o with respect to the normal (grazing emission). Spectra were corrected for sample charging by assigning a binding energy of 103.4 eV to the Si(2p) peak for SiO_2 (17). In cases when the energy of the Si(2p) component could not be determined unambiguously, the

C(1s) binding energy of adventitious carbon was set at 285.0 eV (18) and used as a secondary reference. Peak fitting was accomplished using Gaussian-Lorentzian functions and Shirley background subtraction (19, 20). Atomic concentrations were calculated with atomic sensitivity factors specific for the hemispherical analyzer (21).

SiO_2 samples used in this study were provided by Sematech and consisted of 4000Å thick SiO_2 grown on a Si(100) wafer. Samples (~ 1 cm^2) were cut from the wafer, and were cleaned by sonication in acetone, methanol and deionized water consecutively prior to being mounted on a Ta sample holder. SiO_2 samples were annealed in UHV without sputtering, so as to avoid the creation of surface defects. Commercial oxygen free high conductivity Cu foil (99.995% purity) was used for Cu samples. Cu samples ~ 1 cm^2 were cleaned by repeated cycles of room temperature Ar ion bombardment at 2 keV and 25 mA followed by annealing to 700 K in UHV. A combination of liquid-nitrogen cooling and resistive heating of the sample holder permitted a variation of sample temperature between 120 and 1000 K. Sample temperatures were monitored by a K-type thermocouple, spot-welded at an edge of the sample holder and bent so that the junction was in contact with the sample surface. TDEAT (>99.999%) was supplied in a stainless steel container by a commercial source (ATMI) and used directly without further purification. Electronic grade NH_3 (purity 99.999%) was also obtained from a commercial source (Scott specialty gases). TDEAT and NH_3 were introduced into the main chamber through separate stainless steel doser tubes and controlled with a manual leak valve. Gas exposures are reported here in terms of Langmuir (L), with 1 L=10^{-6} Torr · s. Exposures have not been corrected for flux to the sample or variations in ion gauge sensitivity.

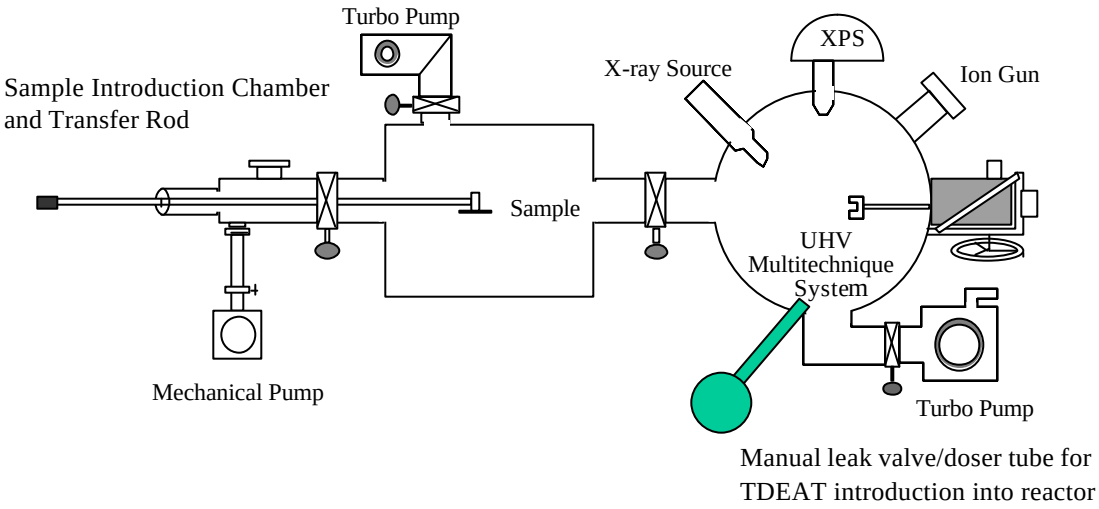

Fig. 3.2 Schematic diagram of the CVD/XPS system

3.3. RESULTS

3.3.1. TDEAT/SiO_2 Interaction

3.3.1.1 In the Absence of NH_3

a. Low temperature condensation at 120K

SiO_2 was exposed to 10^{-8} Torr TDEAT precursor in the main chamber for 100 second (1L) at the temperature of 120 K. After XPS analysis, the sample was annealed in 100 K increments starting from 300 K to 900K for a period of 10 minutes at each temperature. At 120K, the Ti(2p) XPS spectrum (Fig.3.3 a) displays a binding energy of 455.5 eV, consistent with undissociated TDEAT (18, 22). The Ti:N:C atomic ratio, derived from XPS intensities, is 1:7:30, indicative of some precursor dissociation during the dose process. As the sample is

annealed to higher temperature, the Ti(2p) spectrum shifts to higher binding energy, consistent with Ti suboxide and TiO_2 formation. The Ti(2p) spectra include both the Ti($2p_{3/2}$) and Ti($2p_{1/2}$) photoelectron lines, which are present in a 2:1 intensity ratio, respectively, with a 6.0 eV separation (18). Each Ti($2p_{3/2}$) doublet is well fit with FWHM of 1.9 eV for each component. The binding energies at 457.3 eV, and 458.8 eV correspond to reported literature values for TiOx ($x< 2$)(457.5 eV) (23) and TiO_2(458.8 eV) (18). A small feature at 455.5 eV is indicative of a Ti-N chemical environment (18), and it will be referred to as Ti(455.5 eV). During the same procedure, the N(1s) spectrum (Fig.3.3 b) decreases significantly in intensity relative to that of the Si(2p) from the substrate. At 120 K, the N(1s) binding energy value of 396.9 eV is characteristic of undissociated TDEAT (9, 24). The component at about 398.1 eV is consistent with oxynitride formation (SiO_xN_y) (25). Upon annealing to 500 K and above, the total N(1s) intensity decreases sharply, indicating some nitrogen-containing species which are bound to the surface are desorbed at elevated temperature. The O(1s) XPS spectrum is displayed in Fig.3.3 c. Upon annealing to 500 K or above, a new component appears at a binding energy of 530.5 eV, lower than the main O-Si peak binding energy (532.5 eV). The emergence of this component coincides with the growth of a Ti oxide phase (26). The C(1s) intensity (Fig.3.3 d) decreases significantly above 500 K. No evidence of any carbide formation, with a binding energy < 283 eV (7) is observed. There is no binding energy shift in the Si(2p) spectrum(Fig.3.3 e), which indicates that Ti silicide is not formed since its binding energy is at 98.8 eV (27).

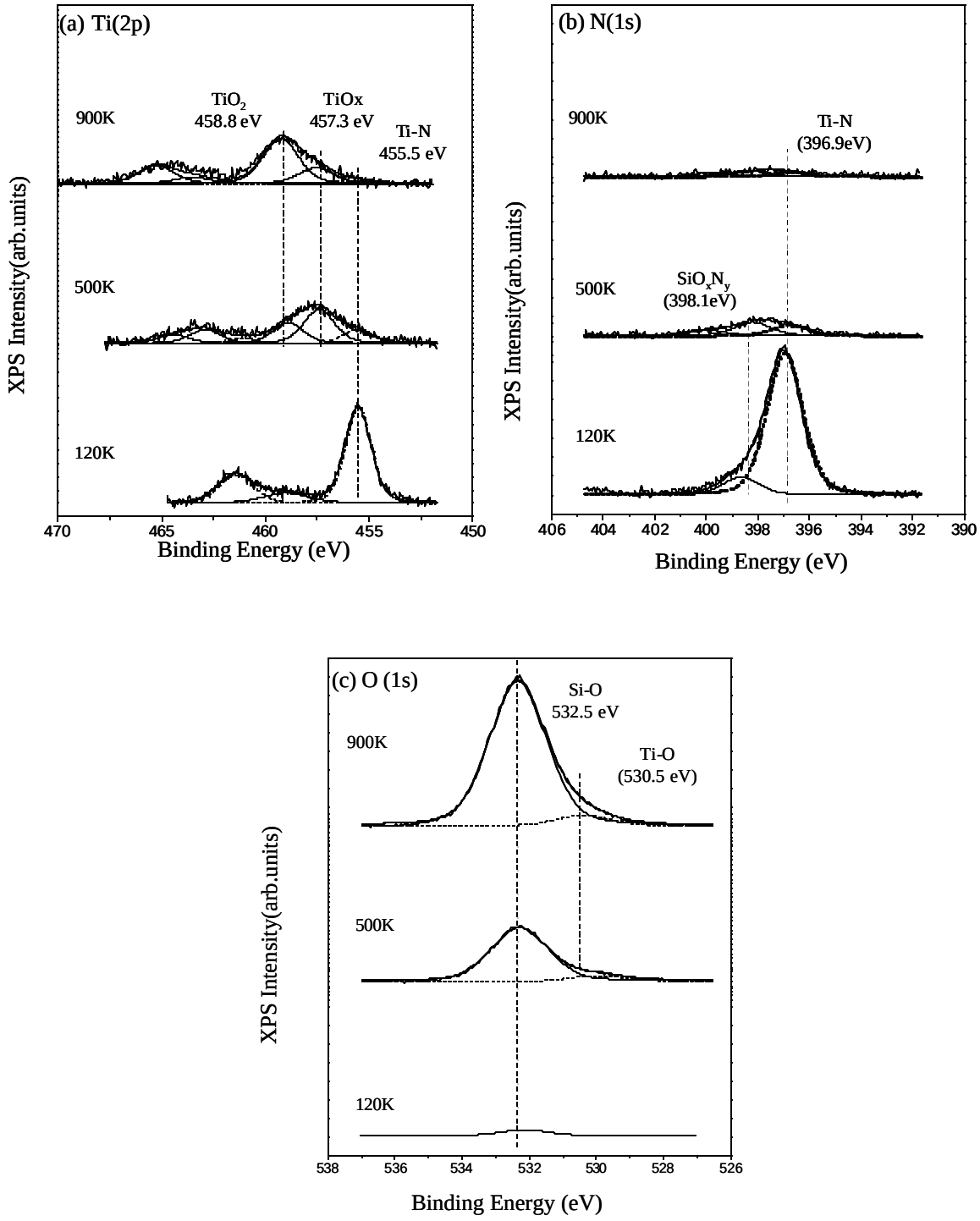
(a) Ti(2p)
900K
TiO2
458.8 eV
TiOx
457.3 eV
Ti-N
455.5 eV
500K
120K
XPS Intensity(arb.units)
Binding Energy (eV)
(b) N(1s)
900K
Ti-N
(396.9eV)
500K
SiOxNy
(398.1eV)
120K
XPS Intensity(arb.units)
Binding Energy (eV)
(c) O (1s)
Si-O
532.5 eV
900K
Ti-O
(530.5 eV)
500K
120K
XPS Intensity(arb.units)
Binding Energy (eV)

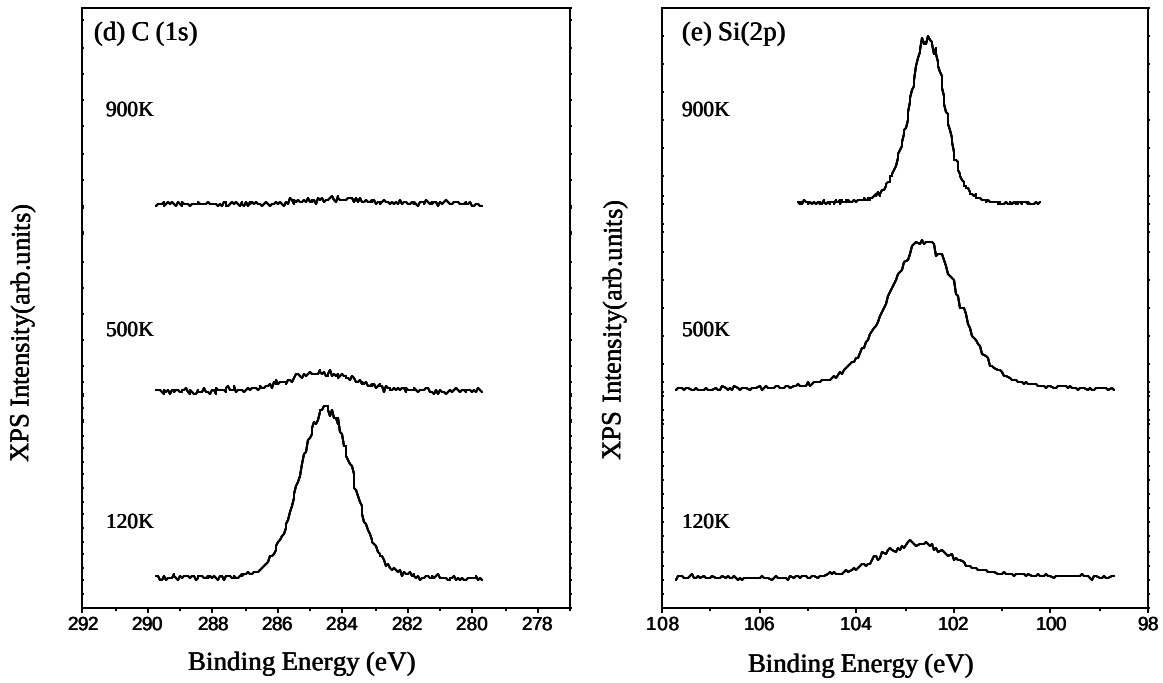

Fig.3.3 XPS spectra for 1L of TDEAT adsorbed on SiO_2 substrate in the absence of NH_3 at 120K followed by annealing to 500 K and 900 K. (a) Ti(2p); (b)N(1s); (c) O(1s);(d) C(1s); (e)Si(2p);

The variations with annealing temperature of the intensities of the various Ti(2p) components – Ti-N(455.5 eV), TiO_x(457.3 eV), and TiO_2(458.8 eV) - are summarized in Fig. 3.4 a. The results indicate that both Ti-N bonded species and Ti sub oxides decrease as the sample temperature increases above 300 K, while TiO_2 intensity increases continuously during the annealing procedure. At 900 K, the dominant product is TiO_2. Only a small amount of Ti-N remains at 900 K. The calculated N(397 eV)/Ti(455.5 eV) atomic ratio varies from 6 (at 120 K) to 1.2 (at 900 K), which indicates that Ti-N bonded species observed at or below 700 K is a partially dissociated precursor intermediate instead of an actual nitride phase. Fig.3.4 b shows the

effect of the annealing temperature on the intensity ratio of Ti(455.5 eV)/Ti(2p total), where Ti(2p total) equals the integrated intensity of $Ti(2p_{3/2})$ over all Ti chemical components. A comparison of normal emission and 60º grazing emission results indicates that the Ti-N species is preferentially located at the precursor/SiO_2 interface instead of at the outer surface of the overlayer film.

These data indicate that TDEAT reacts with SiO_2 at temperature or above, resulting in Ti-N bond dissociation and predominantly Ti-O formation. No Ti-C or Ti-silicide formation is observed.

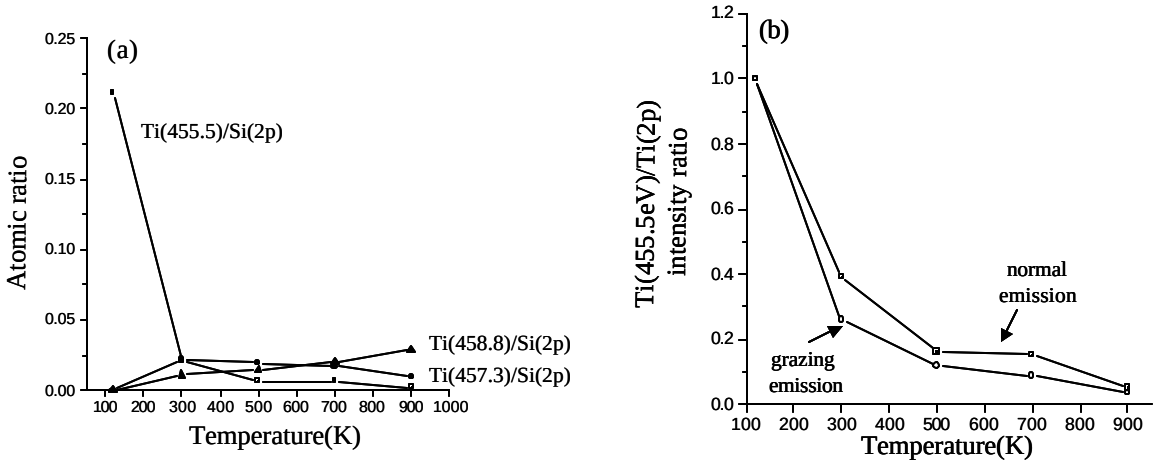

Fig.3.4 (a) The variations in relative $Ti(2p_{3/2})$ XPS intensity (normalized to Si(2p) substrate intensity) corresponding to different Ti bonding environments – Ti-N, TiO_x, and TiO_2 -- as a function of annealing temperature; (b)Ti(455.5 eV)/Ti(2p) XPS intensity ratios at normal emission and 60º grazing emission as a function of annealing temperature.

b. High temperature sequential dose at 500 K

Successive exposures of TDEAT were performed on a SiO_2 surface that was maintained at a constant temperature of 500 K in UHV. The evolutions of the Ti, N and C XPS core level

spectra with precursor exposure are displayed in figure 3.5 (a-c). Ti(2p) spectrum is present at binding energies characteristic of TiO_2, Ti sub-oxide, and TiN.

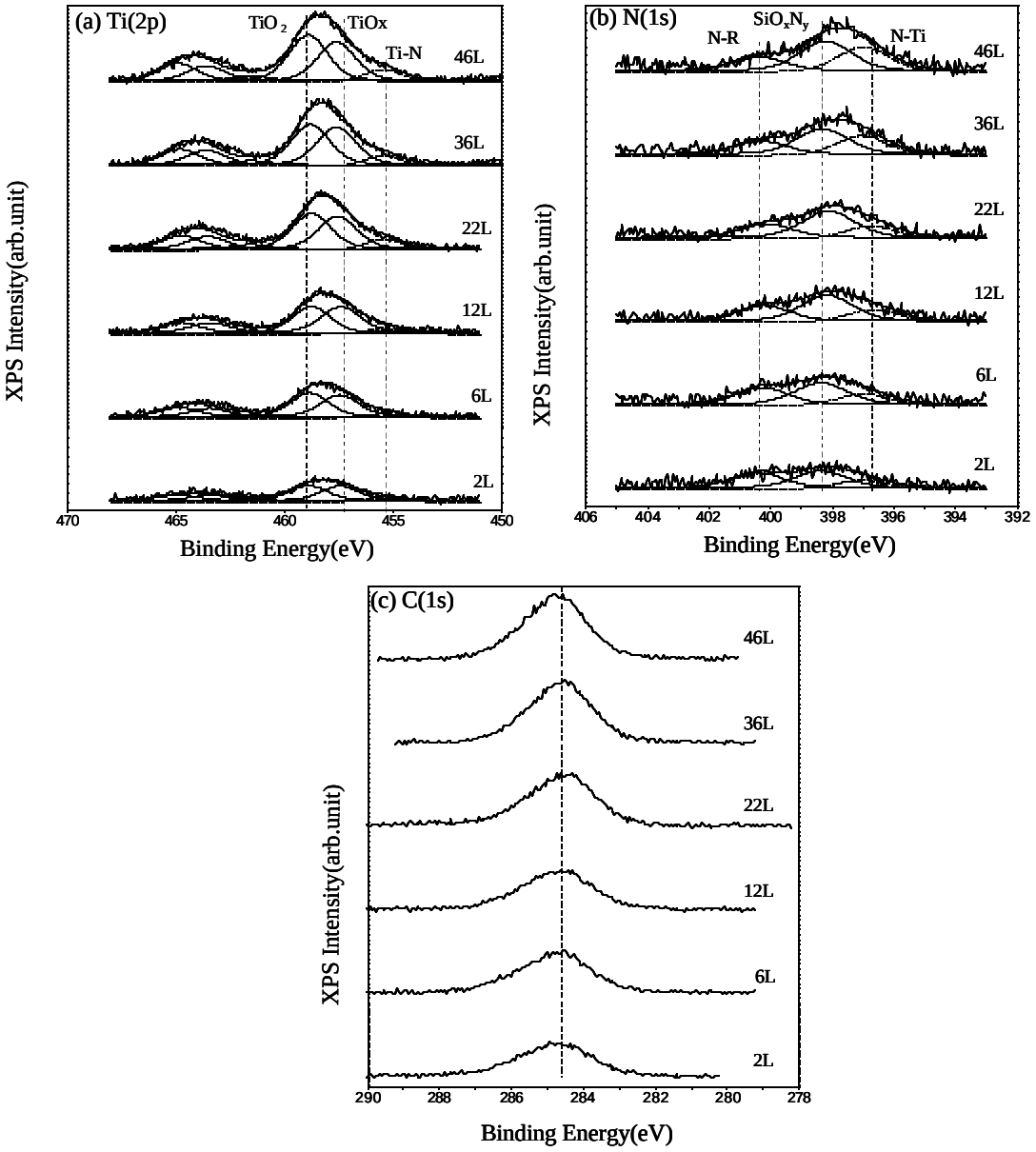

Fig.3.5 XPS spectra for progressive exposures of TDEAT on SiO_2 surface held at a constant temperature of 500 K. (a) Ti(2p); (b)N(1s); (d) C(1s)

The changes in relative XPS intensity (normalized to Si(2p) substrate intensity) with TDEAT exposure of the various Ti(2p) spectra are plotted in Fig.3.6. The results demonstrate that Ti is present predominantly as an oxide or sub-oxide after all exposures at 500 K. The calculated relative Ti(455.5 eV)/Ti(2p total) XPS intensity ratios at normal emission and 60º grazing emission are 0.17 ± 0.01 and 0.11 ± 0.01, and do not vary significantly with TDEAT exposures. The higher relative Ti(455.5 eV)/Ti(2p total) XPS intensity ratio at normal emission indicates that Ti-N species are located preferentially near the film/SiO_2 interface, while the outer region of the Ti film is predominantly oxide or sub-oxide. The C(1s) XPS spectrum (Fig.3.5c) shows only one singe peak with the binding energy ~284.5 eV, which is associated with hydrocarbon groups(CH_3 or CH_2CH_3) (18) from the precursor. There is no significant C(1s) intensity at binding energies at < 283 eV (Fig. 3.5c), indicating that neither Ti carbide nor Si carbide is formed during TDEAT reactions with the surface at 500 K. The amount of hydrocarbon increased, however, during the sequential exposure of TDEAT on SiO_2.

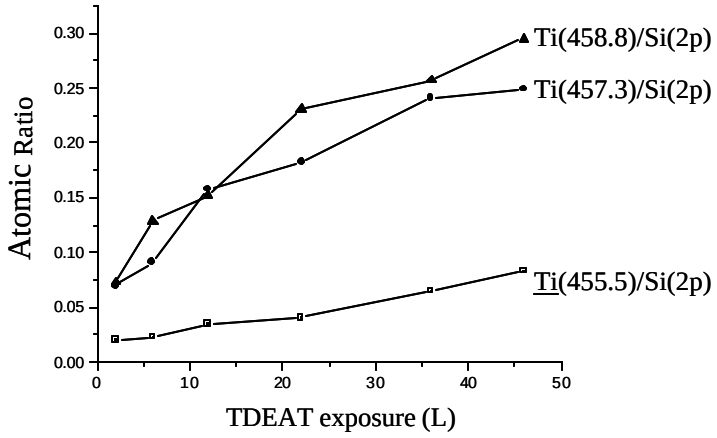

Fig.3.6 The variations in relative Ti($2p_{3/2}$) XPS intensity (normalized to Si(2p) substrate intensity) corresponding to different Ti bonding environments – Ti-N, TiO_x, and TiO_2 -- as a function of TDEAT exposure to a SiO_2 surface held at a constant temperature of 500 K.

3.3.1.2. TDEAT/SiO_2 in the Presence of NH_3

a. Low temperature condensation

Similar TDEAT exposure experiments were carried out on SiO_2 substrate in the presence of NH_3. NH_3 (exposure=2 L) and TDEAT (exposure=1 L) were sequentially co-adsorbed on a clean SiO_2 surface at 120K, followed by progressive annealing to 300 K, 500 K, 700 K and 900 K. The results are summarized in figure 3.7(a-c). In the Ti(2p) spectrum (Fig.3.7a), the relative intensity of the peak associated with Ti-N formation increases upon high temperature annealing. Further evidence of Ti-N formation is also deduced from the N(1s) spectrum (Fig. 3.7b), which displays a peak binding energy of 397 eV in agreement with the literature values for TiN (9). A comparison of the results in Fig. 3.7 with those observed upon physisorption/annealing in the absence of ammonia (Fig.3.3) indicates that the presence of ammonia substantially increases the amount of Ti-N incorporated in the film. This is corroborated by the variations of Ti(455.5eV)/Ti(2p total) intensity ratios with annealing temperature for both physisorbed TDEAT and co-physisorbed TDEAT + NH_3 (Fig. 3.8). At 500 K and above, the concentration of Ti-N species is significantly higher for TDEAT+ co-absorbed NH_3. The intensity of carbon decreases sharply at higher temperature. No carbide formation is observed from C(1s) spectrum (Fig.3.7c), which is the similar result as that observed in the absence of NH_3.

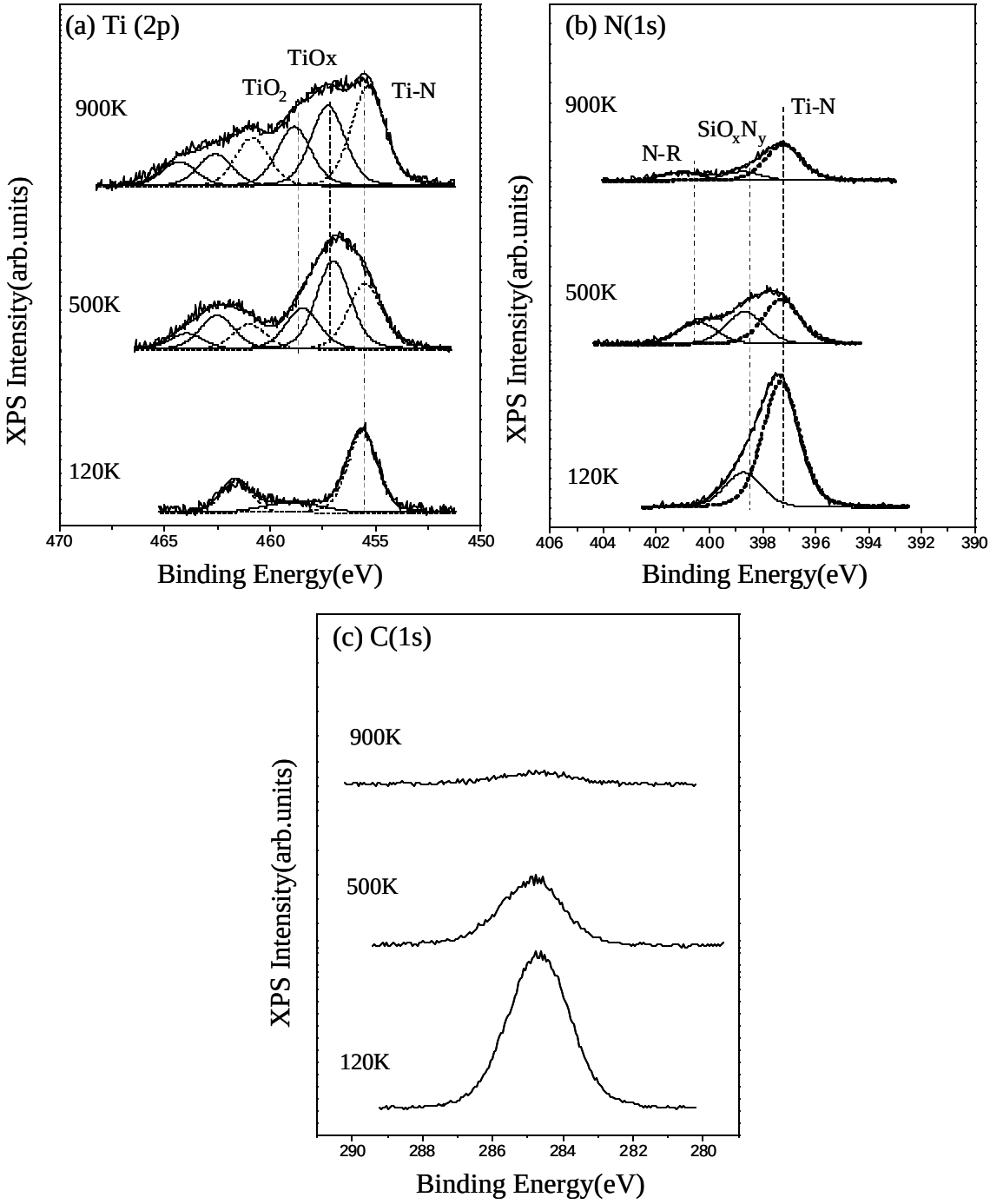

Fig.3.7 XPS spectra for 1L of TDEAT co-adsorbed with NH_3 (2L) on SiO_2 substrate at 120 K followed by annealing to 500 K and 900 K. (a) Ti(2p); (b)N(1s); (c)C(1s);

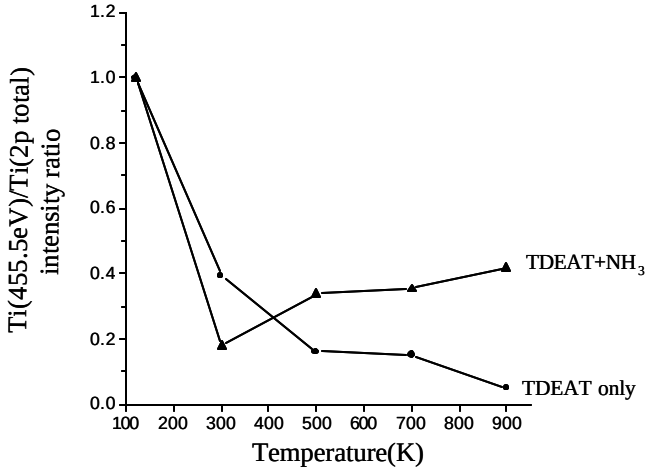

Fig.3.8 Ti(455.5 eV)/Ti(2p total) XPS intensity ratios for 1L TDEAT adsorbed on SiO_2 substrate as a function of annealing temperature in the presence and absence of NH_3 (2 L).

b. High temperature sequential exposure

Successive exposures of TDEAT on the heated SiO_2 surface (T=500 K) were also carried out in the presence of NH_3. The experiment results (Fig.3.9(a-b)) are similar to that obtained with NH_3 co-condensation at low temperature (Fig. 3.7). TiN formation was enhanced in the presence of NH_3 with the background pressure around 10^{-7} Torr. The variations in relative Ti($2p_{3/2}$) XPS intensity (normalized to Si(2p) substrate intensity) corresponding to different Ti bonding environments – TiN, TiO_x, and TiO_2 -- as a function of TDEAT exposure amount are summarized in Fig. 3.10a. Compared with the results shown in Fig.3.6, the intensity of TiN increases with continuous TDEAT dose and becomes the dominant feature at higher exposure. The relative Ti(455.5 eV)/Ti(2p total) XPS intensity ratios continuously increase (from 0.18 to 0.45) with cumulative TDEAT exposure (from 2 L to 36 L) and remains constant at both normal emission and 60º grazing emission geometries (shown in Fig.3.10b). This indicates that the relative concentration of Ti-N is uniformly distributed through the film, in contrast to what is observed in the absence of NH_3. The calculated N(397 eV)/Ti(455.5 eV) atomic ratios with and

without NH_3 treatments are displayed and compared in Table 3.1. The co-exposure of NH_3 results in an N(397 eV)/Ti(455.5 eV) average atomic ratio to 1.2:1, close to the stoichiometry of Ti nitride (TiN). In the absence of NH_3, the N(397 eV)/Ti(455.5 eV) intensity ratio is significantly higher (2.4:1). This might seem counterintuitive. The absence of ammonia, however, results in a much lower relative intensity for the Ti(455.5 eV) feature in the Ti(2p) spectrum (Fig.3.3a). The data summarized in Fig.3.10 and in Table 3.1 therefore indicate that the presence of NH_3 during TDEAT reaction with the SiO_2 surface favors the formation of a TiN film, while the absence of NH_3 results in the presence of a smaller amount of partially unreacted Ti-amino precursors.

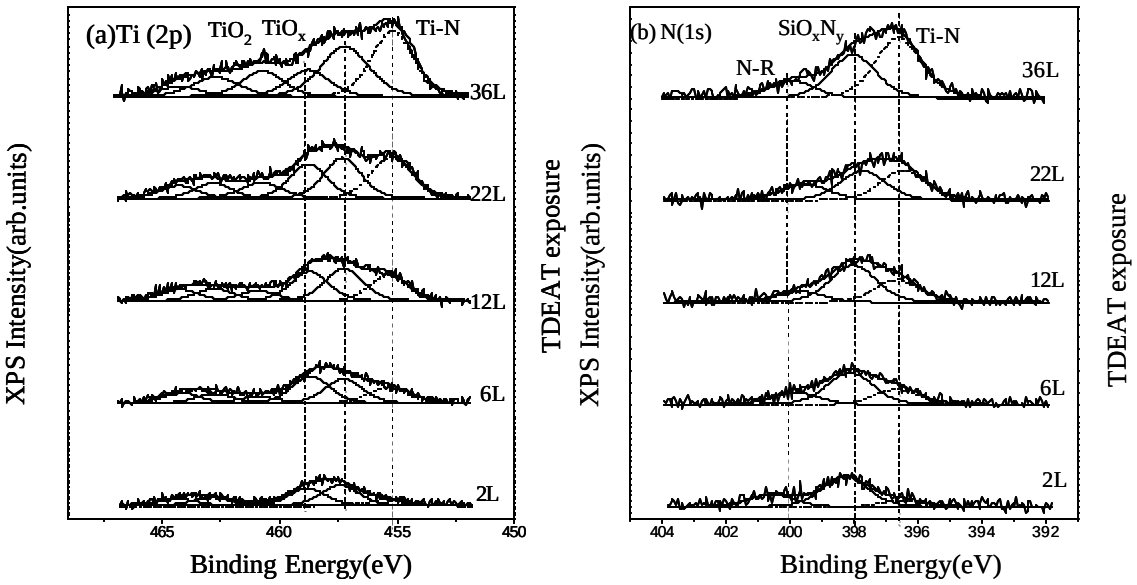

Fig.3.9 XPS spectra for progressive exposures of TDEAT on SiO_2 surface held at a constant temperature of 500 K in the presence of ~10^{-7} Torr NH_3. (a) Ti(2p); (b)N(1s).

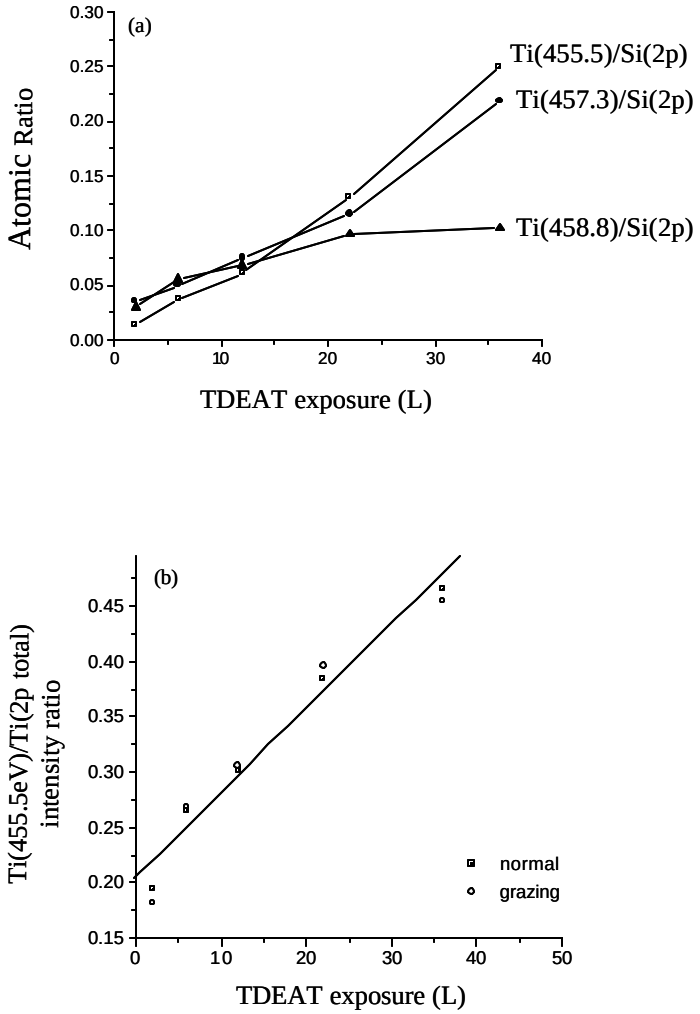

Fig.3.10 (a) Summary of Ti core level spectra for increasing TDEAT exposure to a SiO_2 surface held at a constant temperature of 500 K in the presence of NH_3. (b) Ti(455.5 eV)/Ti(2p) XPS atomic ratios at normal emission and 60º grazing emission as a function of TDEAT exposure.

Table 3.1 N(397 eV)/Ti(455.5 eV) atomic ratios for TDEAT sequential dose on SiO_2 surface at 500 K in the absence and presence of NH_3 treatment (~10^{-7} Torr).

TDEAT exposure (L)	2	6	12	22	36	46	average
TDEAT dose only	2.58	3.00	2.44	2.16	2.21	2.27	**2.4**
TDEAT+NH_3	1.18	1.23	1.23	1.12	1.19		**1.2**

3.3.2. TDEAT/Cu Interaction

3.3.2.1 In the Absence of NH_3

XPS core level spectra resulting from the physisorption of TDEAT (10^{-8} Torr, 100 s, 1 L) on a Cu (poly) substrate at 120 K, followed by annealing to high temperature in UHV, are displayed in Fig.3.11(a-c). The features in Ti(2p) spectra observed before TDEAT exposure(Fig. 10a bottom) and after annealing to 500 K(Fig. 3.11a top) are due to the background signal from Ta sample holder (Ta($4p_{1/2}$)). The data indicate TDEAT is molecularly adsorbed at 120 K (Fig.3.11a middle) on the Cu substrate (BE = 455.5 eV). Annealing to 500 K results in desorption of Ti-containing species from the surface. Neither N(1s) nor C(1s) signal (Fig.3.11 b-c) is observed after 500 K annealing. (The peak with the binding energy centered at 407 eV in the N(1s) spectrum for the clean Cu substrate is due to Cu (LMM) Auger transition.)

Sequential exposures of TDEAT (10^{-8} Torr) on Cu(poly) held at a constant temperature of 500 K resulted in precursor dissociation. Ti(2p) and C(1s) XPS spectra are displayed in Fig.3.12(a-b). The evolution of the Ti(2p) spectrum with TDEAT exposure at 500 K (Fig.3.12a) is marked by a dominant feature with a binding energy of 454.8 eV, which can be attributed to either TiC or Ti-alkyl species (28, 29). The corresponding growth of a dominant feature at 284.8 eV binding energy in the C(1s) spectrum (Fig.3.12b) is indicative of alkyl groups at the surface, and the Ti(2p) feature is therefore assigned to the formation of Ti-alkyl species. A new shoulder also appears at a lower binding energy of 282.8 eV in the C(1s) spectrum (7) corresponding to metal carbide formation. A minor component at 286.3 eV associated with C-O bond formation (26), may be due to the contamination from the chamber. No N peak is observed (not shown).

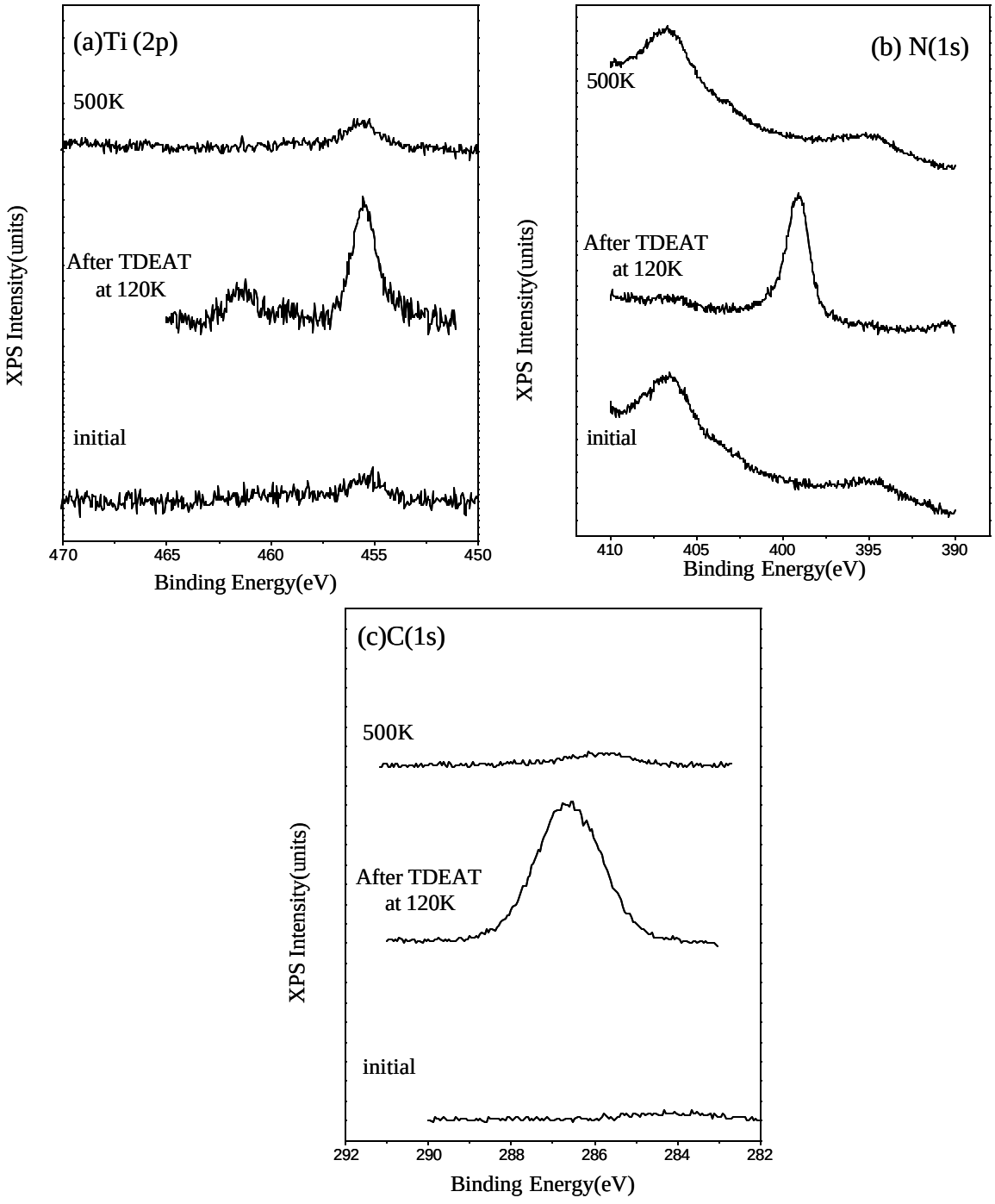

Fig.3.11 XPS spectra for TDEAT (1 L) physisorbtion on Cu substrate in the absence of NH_3 followed by annealing to 500 K. (a) Ti(2p); (b)N(1s); (c) C(1s).

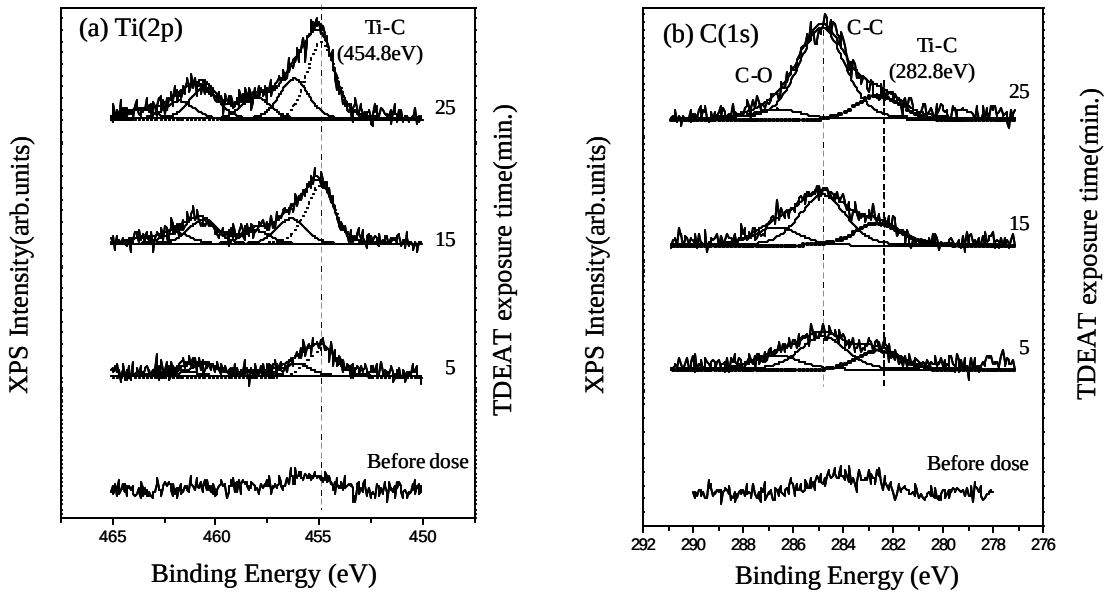

Fig.3.12 XPS spectra for successive exposure of TDEAT (10^{-8} Torr) on Cu substrate at a constant temperature of 500 K. (a) Ti(2p);(b)C(1s).

3.3.2.2 In the Presence of NH_3

Co-adsorption of TDEAT and NH_3 on Cu at 120 K, followed by annealing to high temperature yields identical results to those observed in the absence of NH_3—molecular adsorption at 120 K followed by desorption from the surface at or below 500 K. Exposures of both TDEAT and NH_3 on Cu at 500 K exhibit the similar results as exposure to TDEAT only.

3.4. DISCUSSION

The data reported here demonstrate that TDEAT physisorbed on SiO_2 at 120 K followed by annealing will react at temperatures below that required for precursor desorption, resulting in Ti-O bond formation at or below 500 K (Fig. 2a) and in increasing TiO_2 formation upon annealing to higher temperatures in UHV. A similar reaction pathway is observed upon TDEAT

exposure to a SiO_2 surface held at a constant temperature of 500 K. In both cases, TDEAT interactions with SiO_2 are dominated by Ti interactions with substrate oxygen sites, and that Ti oxide/sub-oxide bond formation can proceed with relatively low activation energy. A comparison of Ti-O, Ti-N and Ti-C bond enthalpies (Ti-O 672 kJ/mol, Ti-N 476 KJ/mol, Ti-C 423 kJ/mol) (30) explains the predominance of Ti oxide over nitride formation and lack of Ti-C bond formation due to a much larger Ti-O bond enthalpy. The co-adsorption of NH_3 and TDEAT at 120K followed by annealing, results in enhanced Ti-N formation and higher stability above 500K than is observed without co-adsorbed NH_3 (Fig.3.8). Similarly, reaction of TDEAT with SiO_2 at 500 K in the presence of NH_3 exhibits a relatively enhanced Ti-N spectral component. The Ti(455.5 eV)/Ti(2p total) intensity ratio is the same at both grazing and normal emission, (Fig. 3.10b). In contrast, the absence of co-adsorbed NH_3 results in a preferential concentration of Ti-N species near the film/SiO_2 interface. Additionally, film produced with co-adsorbed NH_3 and TDEAT has a N/Ti stoichiometry of 1.2, consistent with nitride formation. In the absence of NH_3, an anomalous N(397 eV)/Ti(455.5 eV) atomic ratio of 2.4 indicates the presence of partially unreacted precursor rather than true nitride formation.

TDEAT dissociation on polycrystalline Cu has a higher activation energy than dissociation on SiO_2 as evidenced by the fact that molecular adsorption at low temperatures followed by annealing results in no precursor reaction with the surface. Dissociative chemisorption is observed only upon reaction with a heated Cu substrate (500 K). The observation of a Ti-alkyl reaction product under these conditions indicates that the β-hydride elimination reaction observed in the gas phase in the absence of NH_3 (Fig. 3.1b) also occurs under these conditions. The presence of NH_3 at the partial pressures possible in a UHV chamber ($\sim 10^{-7}$ Torr) would not be expected to alter this result, since negligible gas phase interaction

leading to transamination should occur under controlled high vacuum conditions. These results differ from those reported for the TDEAT/NH_3 reaction on reactive metal surfaces such as Ti, W and Ta (6). Those studies show that transammination reactions occur at such surfaces, and that the absence of NH_3 can result in metal carbide formation. The data presented here (Fig.3.12) reveal that a thin film containing Ti-alkyl species on the Cu surface, following reaction with TDEAT at elevated temperatures. This might pose a problem for the adhesion of subsequently deposited metals (31), unless the alkyl adlayer can be removed before or during subsequent deposition processes.

3.5 SUMMARY AND CONCLUSIONS

XPS studies have been carried out on the chemical vapor deposition of TDEAT [$Ti(NEt_2)_4$] on SiO_2 and Cu substrate in the presence (~ 10^{-7} Torr or co-adsorbed) and absence of NH_3. The results include the following:

(1) TDEAT interactions with SiO_2 in the absence of NH_3 are dominated by Ti interactions with substrate oxygen sites, and that Ti oxide/sub-oxide bond formation can proceed with relatively low activation energy. No Ti carbide or Si carbide formation is observed. Co-adsorption of TDEAT and NH_3 on SiO_2 at 120 K followed by annealing to higher temperature results in enhanced Ti-N bond formation, although Ti sub oxide and Ti oxide are present. The Ti-N species is stable against oxidation up to 900 K in UHV. Continuous exposures of TDEAT on SiO_2 at 500 K yield similar results–Ti nitride formation is enhanced by the presence of NH_3 (~ 10^{-7} Torr).

(2) Co-adsorption of NH_3 and TDEAT on Cu (poly) surface at 120 K, followed by annealing to 500 K, results in complete desorption of Ti, N or C-containing species from the Cu

substrate. Reaction of TDEAT with a Cu surface at 500 K yields a Ti-alkyl species via a β-hydride elimination pathway. TDEAT/Cu interactions are not observably affected by overpressures of NH_3 of 10^{-7} Torr.

3.6 CHAPTER REFERENCES

(1) Wittmer, M. *J. Vac. Sci. Technol.A* **1984,** *2*, 273.

(2) Murauka, S. P. *Metallization: Theory and Practice for VLSI and ULSI*; Butterworth-Heinemann: Boston, 1993.

(3) Cerio, F.; Drewery, J.; Huang, E.; Reynolds, G. *J. Vac. Sci. Technol. A* **1998,** *16*, 1863.

(4) Yokoyama, N.; Hinode, K.; Homma, Y. *J. Electrochem. Soc.* **1991,** *138*, 190.

(5) Hedge, R. I.; Fiordalice, R. W.; Travis, E. O.; Tobin, P. J. *J. Vac. Sci. Technol. B* **1993,** *11*, 1287.

(6) Truong, C. M.; Chen, P. J.; Corneille, J. S.; Oh, W. S.; Goodman, D. W. *J. Phys. Chem.* **1995,** *99*, 8831.

(7) Zhao, J.; Garza, E. G.; Lam, K.; Jones, C. M. *Appl. Surf. Sci.* **2000,** *158*, 246.

(8) Yun, J.-Y.; Park, M.-Y.; Rhee, S.-W. *J. Electrochem.Soc.* **1999,** *146*, 1804.

(9) Endle, J. P.; Sun, Y.-M.; White, J. M.; Ekerdt, J. G. *J. Vac. Sci. Technol. A* **1998,** *16*, 1262.

(10) Xiao, S. Q.; Tobe, R.; Suzuki, K.; Xu, X. B.; Sekiguchi, A.; Doi, H.; Okada, O.; Hosokawa, N. *Mat. Res. Soc. Symp. Proc.* 2000, 295, Advanced Metallization Conference, Orlando, FL, September 28-30, 1999

(11) Fix, R. M.; Gorden, R. G.; Hoffman, D. M. *Chem. Mater.* **1990,** *2*, 235.

(12) Dubois, L. H. *Polyhedron* **1994,** *13*, 1329.

(13) Ruhl, G.; Rehmet, R.; Knizova, M.; Merica, R.; Vepek, S. *Chem. Mater.* **1996,** *8*, 2712.

(14) Yun, J.-Y.; Rhee, S.-W. *Thin Solid Films* **1998,** *312*, 24.

(15) Boo, J.-H.; Heo, C. H.; Cho, Y. K.; Han, J.-G. *J. Vac. Sci. Technol. A* **2000,** *18*, 1590.

(16) Garza, M.; Magtoto, N. P.; Kelber, J. A. *Surf. Sci.* **2002,** *519*, 259.

(17) Barr, T. L. *J. Vac. Sci. Technol. A* **1991,** *9*, 1793.

(18) Moulder, J. F.; Stickle, W. F.; Sobol, P. E.; Bomben, K. D. *Handbook of X-ray Photoelectron Spectroscopy*; Physical Electronics: Eden Prarie, 1992.

(19) Shirley, D. A. *Phys. Rev.* **1972,** *B 5*, 4709.

(20) Sherwood, P. M. A. *J. Vac. Sci. Technol. A* **1995,** *14*, 1424.

(21) Electronics, P. *PC-EXPLORER Software manuals*, 1998.

(22) Briggs, D.; Seah, M. P. *Practical Surface Analysis*, 2nd ed.: Wiley, New York, 1990.

(23) Lu, G.; Bernasek, S. L.; Schwartz, J. *Surf. Sci.* **2000,** *458*, 80.

(24) Chourasia, A. R.; Chopra, D. R. *Thin Solid Films* **1995,** *266*, 298.

(25) Guimon, C.; Gonbeau, D.; Guillouzo, G. P.; Dugne, O.; Guette, A.; Naslain, R.; Lahaye, M. *Surf. Interface Anal.* **1990,** *16*, 440.

(26) Jouan, P.-Y.; Peignon, M.-C.; Cardinaud, C.; Lemperiere, G. *Appl. Surf. Sci.* **1993,** *68*, 595.

(27) Peto, G.; Zsoldos, E.; Guczi, L.; Schay, Z. *Solid State Commun.* **1986,** *57*, 817.

(28) Miller, S.; Berning, G. L. P.; Plank, H.; Roth, J. *J. Vac. Sci. Technol. A* **1997,** *15*, 2029.

(29) Rats, D.; Vandenbulcke, L.; Herbin, R.; Benoit, R.; Erre, R.; Serin, V.; Sevely, J. *Thin Solid Films* **1995,** *270*, 177.

(30) Kerr, J. A. *CRC Handbook of Chemistry and Physics 1999-2000 : A Ready-Reference Book of Chemical and Physical Data (CRC Handbook of Chemistry and Physics)*, 81st ed.; CRC Press: Boca Raton, Florida, 2000.

(31) Tong, J.; Martini, D.; Magtoto, N.; Kelber, J. *J. Vac. Sci. Technol. B* **2003,** *21(1)*, 293.

CHAPTER 4

TDEAT INTERACTION WITH LOW-DIELECTRIC SUBSTRATES

4.1. INTRODUCTION

As integrated circuit sizes decrease below 0.25 microns, device performance will no longer improve at the same rate as for past generations because of RC interconnect delay, which becomes significant as compared to the intrinsic gate delay. One approach to address this is to use a lower resistance metal. For example: copper instead of aluminum. Another approach is to use a new material with a dielectric constant (k) significantly lower than that of SiO_2 ($k \approx 4$).

In order to prevent Cu diffusion, barrier films are needed to be deposited on the low-k dielectrics. The integration of TiN and TiSiN diffusion barriers with low-k dielectrics is an issue of technological significance, since undesirable interfacial chemistry can affect Cu wetting/adhesion, and the diffusion of various precursor species into the bulk of the dielectric. Characterization of barrier films/low-k interactions at the atomic and molecular levels will yield insight into the strengths and weaknesses of the materials and their processibility.

In this work, the interactions between CVD TiN by using tetrakis(diethylamido) titanium $Ti[N(C_2H_5)_2]_4$ (TDEAT) precursor and low-k dielectric materials are investigated by using X-ray photoelectron spectroscopy (XPS) and atomic force microscopy (AFM). Detailed interfacial chemistry will be provided and compared with three different low-k materials.

4.2. EXPERIMENT

Experiments were performed in a combined UHV analysis/chemical vapor deposition (CVD) system, which has been already described in chapter 3 (1). The surface morphologies and roughness of the different low-k substrates were examined by atomic force microscopy (AFM)

(Nanoscope-4, Digital Instruments) with contact mode. In order to minimize AFM tip-induced deformation of the substrate during direct contact measurements, a mechanically soft AFM tip (Nanoscope Pt/Ir) was used for these measurements.

Experiments were of two types. The first type involved physisorption of TDEAT on the low *k* material at <120 K, followed by XPS acquisition upon annealing at higher temperatures. The second type involved exposure of TDEAT vapor to the low-*k* substrate while the substrate was maintained at a constant, elevated temperature (e.g.,700 K). Both types of experiments were carried out in the presence and absence of NH_3. As shown in the energy diagram (Fig.4.1), the first type of experiment (physisorption at low temperature) provides information on surface reaction pathways with low activation energies. If an activation barrier to a chemical reaction is less than the heat of adsorption of the molecularly adsorbed precursor, then the precursor/substrate chemical reaction will proceed. Conversely, if an activation barrier is greater than the precursor heat of desorption, the precursor will desorb before activation barrier can be surmounted. A comparison of products from the first type of experiment with those of the second type will reveal which products result from reactions with high activation barriers at temperatures relevant to industrial practice.

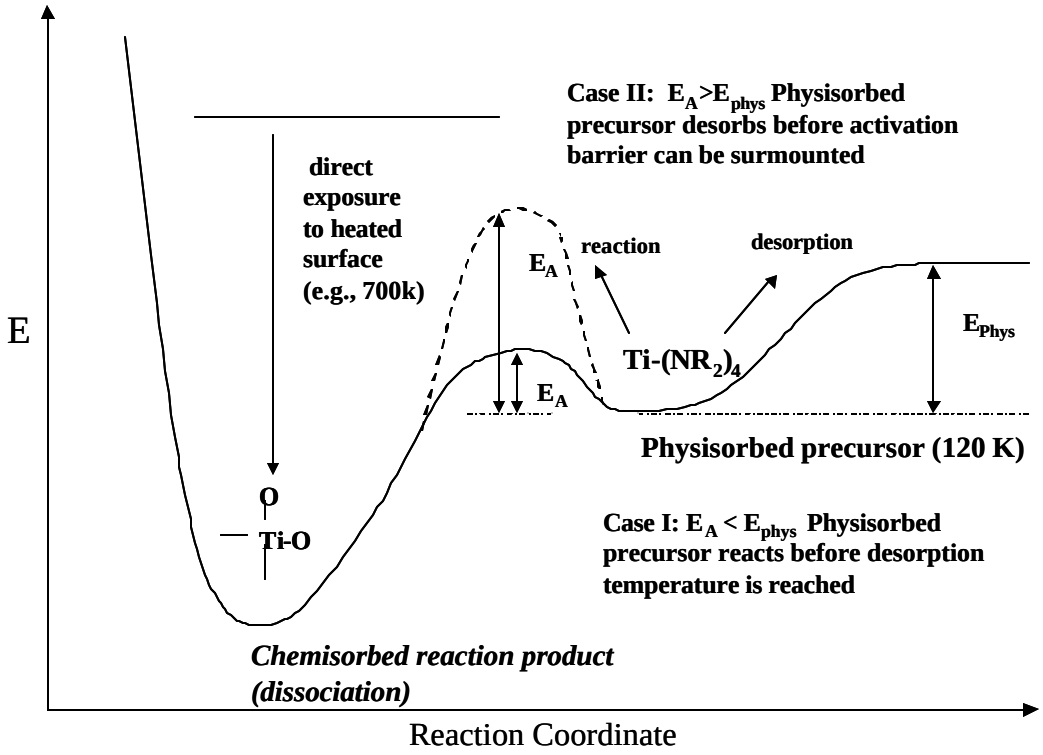

Fig. 4.1 The reaction energy diagram

4.3. RESULTS

4.3.1. Low-*k* Sample Composition Analysis

X-ray photoelectron spectroscopy (XPS) was used to characterize the chemical composition of three different low-*k* substrates (designated low *k*-1, low *k*-2 and low *k*-3). The characteristics of low-*k* samples are summarized in Table 4.1. The composition of the sample was calculated using the following equation:

$$C_x = \frac{I_x/SF_x}{\sum_i I_i/SF_i} \qquad (4\text{-}1)$$

where C is the number of atoms of the element x per unit volume, *I* is the intensity of photoelectron signal detected per second, and SF is the atomic sensitivity factor appropriate to the analyzer.

Table 4.1. XPS characterization of different low-*k* substrates

Low-*k*		BE(eV)	bond	atom (%)	stoichiometry
Low*k*-1	Si	103.3	Si-O	27.5	
		102.2	O-Si-C		
	O	532.5	O-Si	53.6	$SiO_2C_{0.7}$
		531.5	O-Si-C		
	C	285.0	C-C	18.9	
		283.9	C-Si		
Low*k*-2	Si	103.2	Si-O	30.9	
	O	532.5	O-Si	63.1	$SiO_2C_{0.2}$
	C	285.0	C-C	6.0	
Low*k*-3	C	285.0	C-C	98	hydrocarbon
	O	533.6		2	

Si(2p), O(1s) and C(1s) XPS spectra of three low-*k* samples are shown in figure 4.2(a-c). The Si(2p) spectrum of low *k*-1 sample is well fit with a FWHM of 1.9 eV at binding energies of 103.3 eV and 102.2 eV, respectively. The peak at 103.3 eV can be assigned as Si-O bond (2), while the feature at 102.2 eV indicates a different chemical environment, which can be assigned as O-Si-C bond formation (3, 4). O(1s) spectrum can be fit with a FWHM of 1.8 eV at binding energies of 532.5 eV and 531.5 eV, consistent with O-Si (2) and O-Si-C (5) bonding environments, respectively. In C(1s) spectrum, the peak at binding energy of 283.9 eV is in agreement with C-Si bond (6), and the feature at 285 eV is the adventitious C-C or C-H formation (7). The data indicate that low *k*-1 sample is a carbon doped silicon oxide with a

stoichiometry of $SiO_2C_{0.7}$. The individual core level XPS spectra for low *k*-2 sample are also illustrated in Fig. 4.2 (b) for comparison. The specific FWHMs for Si(2p),O(1s) and C(1s) are fixed during the peak fitting procedure. The single peak in the individual core level spectrum indicates the low *k*-2 sample has only Si-O bond with little C content (3-6 at.% C). For low *k*-3 sample, silicon peak is not observed and C(1s) is the dominant feature(98 at. % C), indicating it is probably an aromatic hydrocarbon material.

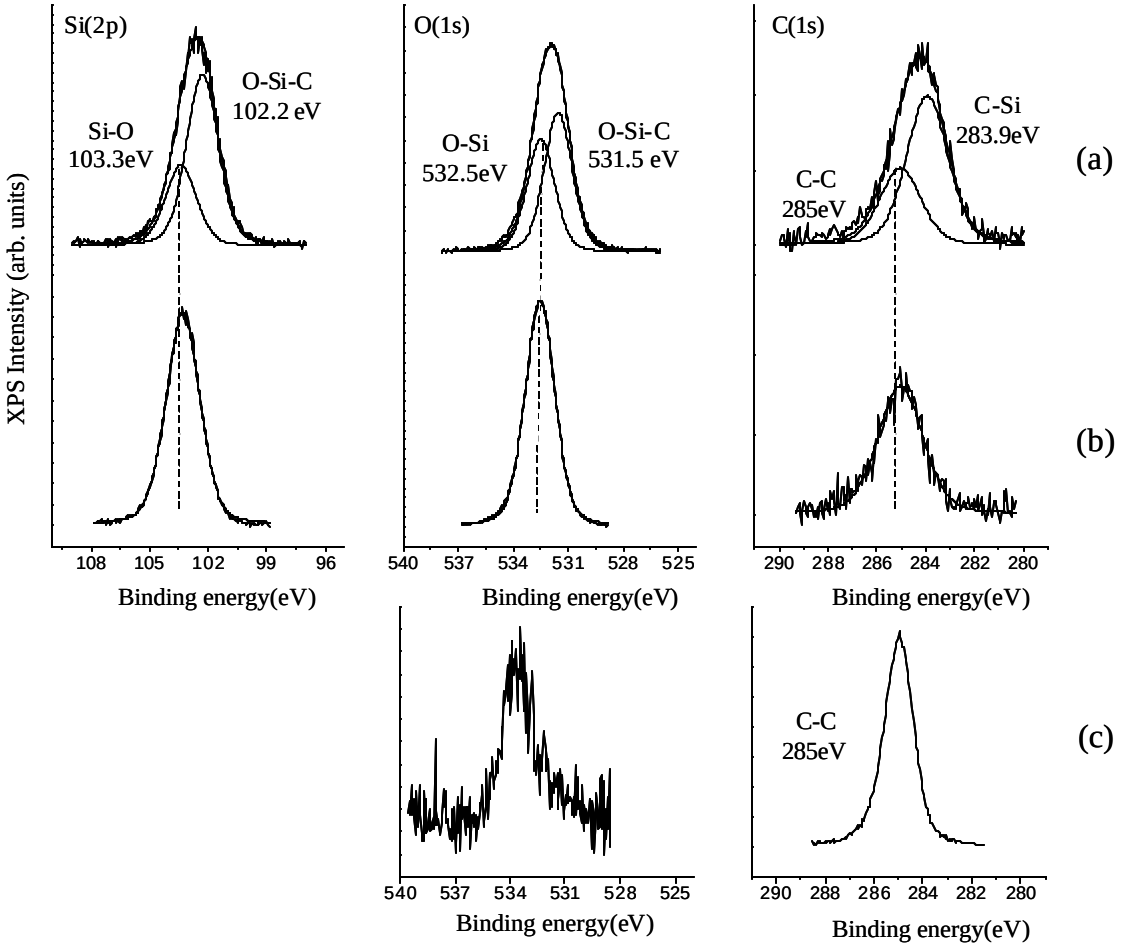

Fig.4.2 Si(2p), O(1s) and C(1s) XPS spectra for clean low-*k* substrates: (a)low *k*-1; (b)low *k*-2; (c)low *k*-3

The AFM images of surface morphologies of different samples are shown in Fig.4.3 (a-c). The data indicate the low *k*-1 ($SiO_2C_{0.7}$) shown in Fig. 4.3(b) is quite rough and porous compared with SiO_2 (Fig. 4.3(a)), while the low *k*-2 sample (Fig. 4.3c) has the similar topography as SiO_2 surface. The root-mean-square (rms) roughness is 0.37 nm for low *k*-1, 0.21 nm for low *k*-2 and 0.19 nm for SiO_2.

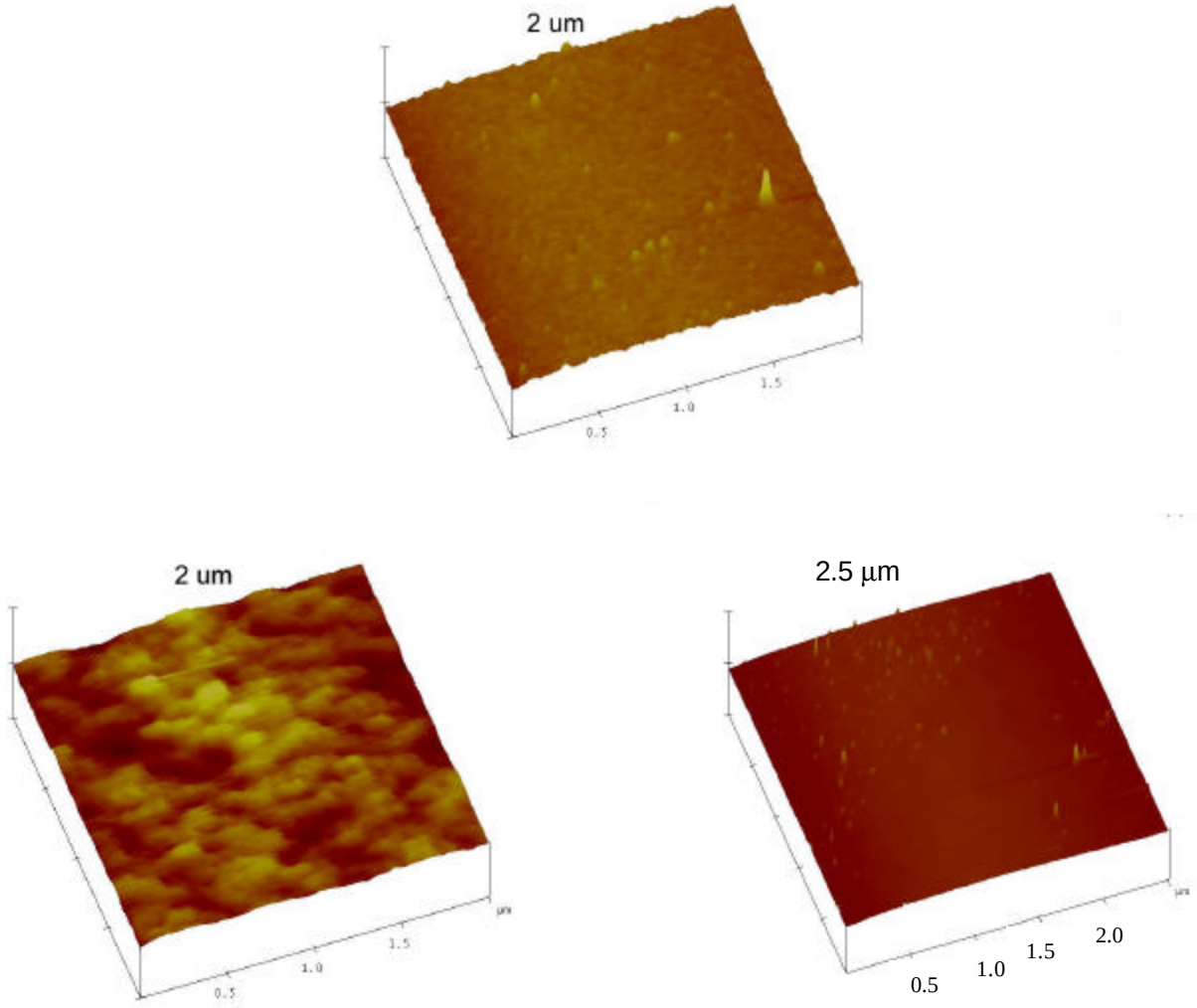

Fig.4.3 Atomic force microscopy (AFM) images of clean dielectric substrates. (a) SiO_2; (b) low *k* -1($SiO_2C_{0.7}$); (c) low *k*-2 ($SiO_2C_{0.2}$)

4.3.2. Reactions of TDEAT with Low-*k* Substrates at 120 K

The low-*k* samples were exposed to 5×10^{-9} ~1×10^{-8} Torr TDEAT precursor in the main chamber for 10 min (3 L~6 L) at the temperature of 120 K. After XPS analysis, the samples were annealed in 100 K increments starting from 300 K to 900 K for a period of 10 minutes at each temperature.

4.3.2.1 Low k-1($SiO_2C_{0.7}$)

Ti(2p),N(1s), O(1s) and C(1s) XPS spectra are shown in Fig. 4.4(a-d). At 120 K, the Ti(2p) feature(Fig.4.4a) at 455.5 eV is indicative of the undissociated $Ti(NEt_2)_4$ binding energy (7). The main peak at 397.4 eV of N(1s)(Fig.4.4 b) peak is characteristic of a Ti-N bond (8, 9). The presence of a shoulder at higher binding energies (>399 eV) is characteristic of amino group adsorption on the substrate surface, indicating some precursor dissociation during the dosing process. As the sample is annealed to higher temperature under UHV conditions, the Ti(2p) spectrum shifts to higher binding energies and the intensity becomes very negligible. The intensity of the main N(1s) peak decreases significantly, indicating dissociation of Ti-N bonds as well as some TDEAT desorption from the surface. The O(1s) spectra (Fig.4.4c) indicates that as the temperature increases, the intensity of oxygen increases while the peak features stay consistent. No significant Ti oxide formation is observed from O(1s) spectra, which has a lower binding energy of 530.5 eV (10). The intensity of C(1s)(Fig.4.4d) decreases very little after higher temperature annealing. No evidence of TiC formation—which would be indicated by C(1s) spectrum at binding energies < 283 eV(11), is observed.

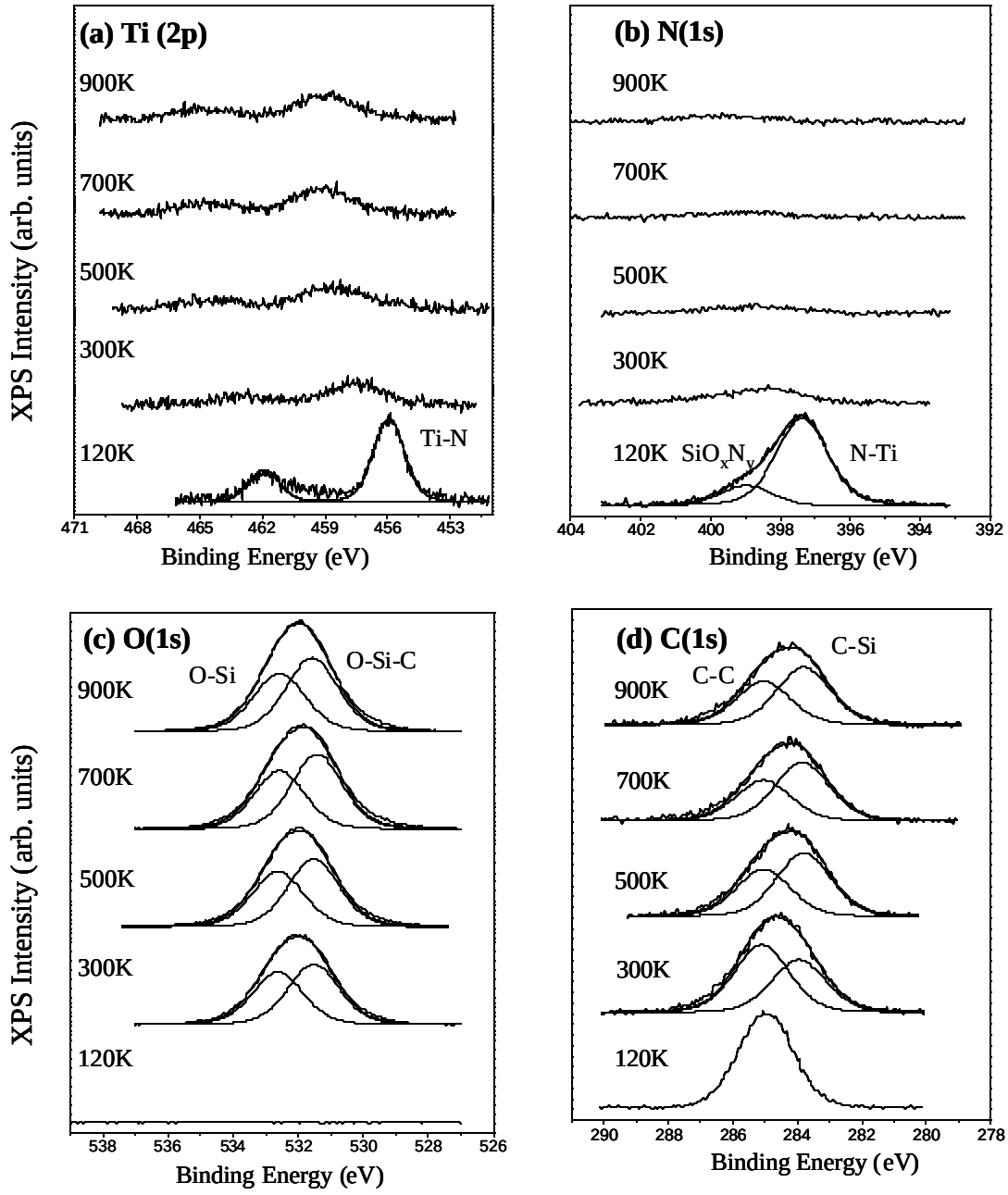

Fig.4.4 XPS spectra for 3 L of TDEAT adsorbed on low *k*-1 surface at 120 K and annealed to higher temperatures. (a)Ti(2p), (b)N(1s), (c)O(1s) and (d)C(1s)

Similar experiments were carried out in the presence of NH_3. Ammonia (~10^{-8} Torr, 10 min, exposure=30L) and TDEAT ($5x10^{-9}$ Torr, 10 min, 3 L) were co-adsorbed on a clean low*k*-1 surface at 120K, followed by progressive annealing to 300 K, 500 K, 700 K and 900 K. The data (not shown here) does not yield any evident difference compared to results obtained in the absence of NH_3.

4.3.2.2 Low k-2 ($SiO_2C_{0.2}$)

TDEAT condensation on low *k*-2 material at 120 K, followed by high temperature annealing was performed in the absence and in the presence of NH_3(10^{-8} Torr, 10 min, 6 L). Ti(2p) and N(1s) XPS spectra in both cases are shown in Fig.4.5(a-b) for comparison. Ti($2p_{3/2}$) spectrum is well fit with three chemical components with the binding energy of 455.5 eV, 457.3 eV, 458.8 eV associated with Ti-N (7), Ti suboxide(12) and Ti oxide (7) formation, respectively. N(1s) spectrum presents the feature at 397 eV, a value characteristic of Ti-N bond formation. TDEAT dissociatively chemisorbs on low *k*-2 substrate at room temperature or above, resulting in Ti-N bond scission, and Ti-O bond formation. C(1s) and O(1s) XPS spectra are shown in Fig. 4.6(a-b). The intensity of carbon decreased significantly at high temperature annealing. No carbide formation is observed from C (1s) spectrum in the absence and in the presence of NH_3. The feature at binging energy of 530.5 eV in O(1s) spectrum is the further verification of Ti oxide formation. In the presence of NH_3, the Ti-N formation was enhanced, which can be observed from the increase of the absolute intensities of the related features in both Ti(2p) and N(1s) core level spectra. This is corroborated by the variations of Ti(455.5 eV)/Ti(2p total) intensity ratios with annealing temperature for both physisorbed TDEAT and co-physisorbed TDEAT + NH_3(Fig.4.7). These results are very similar to the results we obtained from the interaction of TDEAT with SiO_2 substrate, which have been discussed in chapter 3.

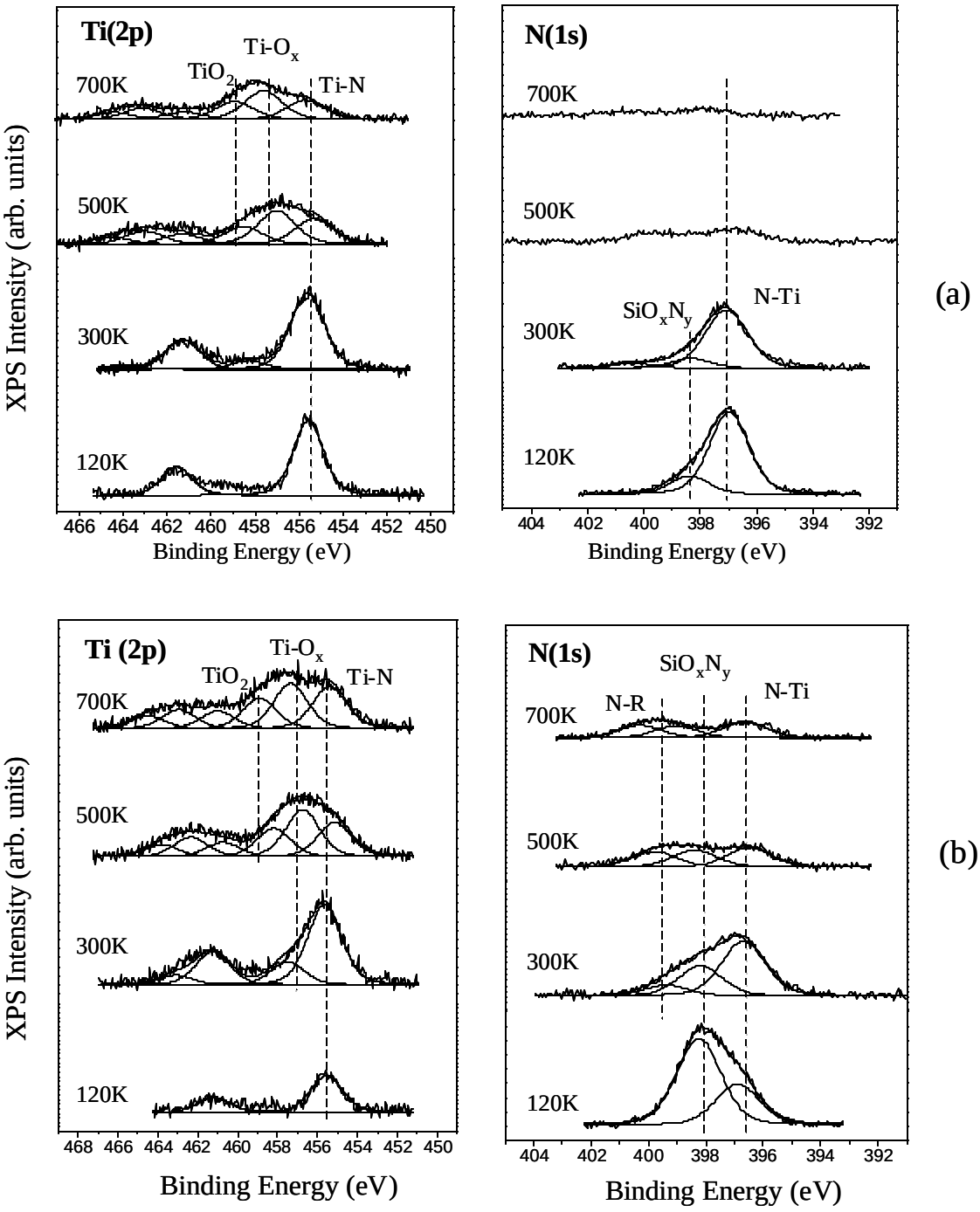

Fig.4.5 Ti(2p) and N(1s) XPS spectra for 3 L of TDEAT adsorbed on low *k*-2 surface at 120 K and annealed to higher temperatures. (a)TDEAT only (b) in the presence of 6 L NH_3

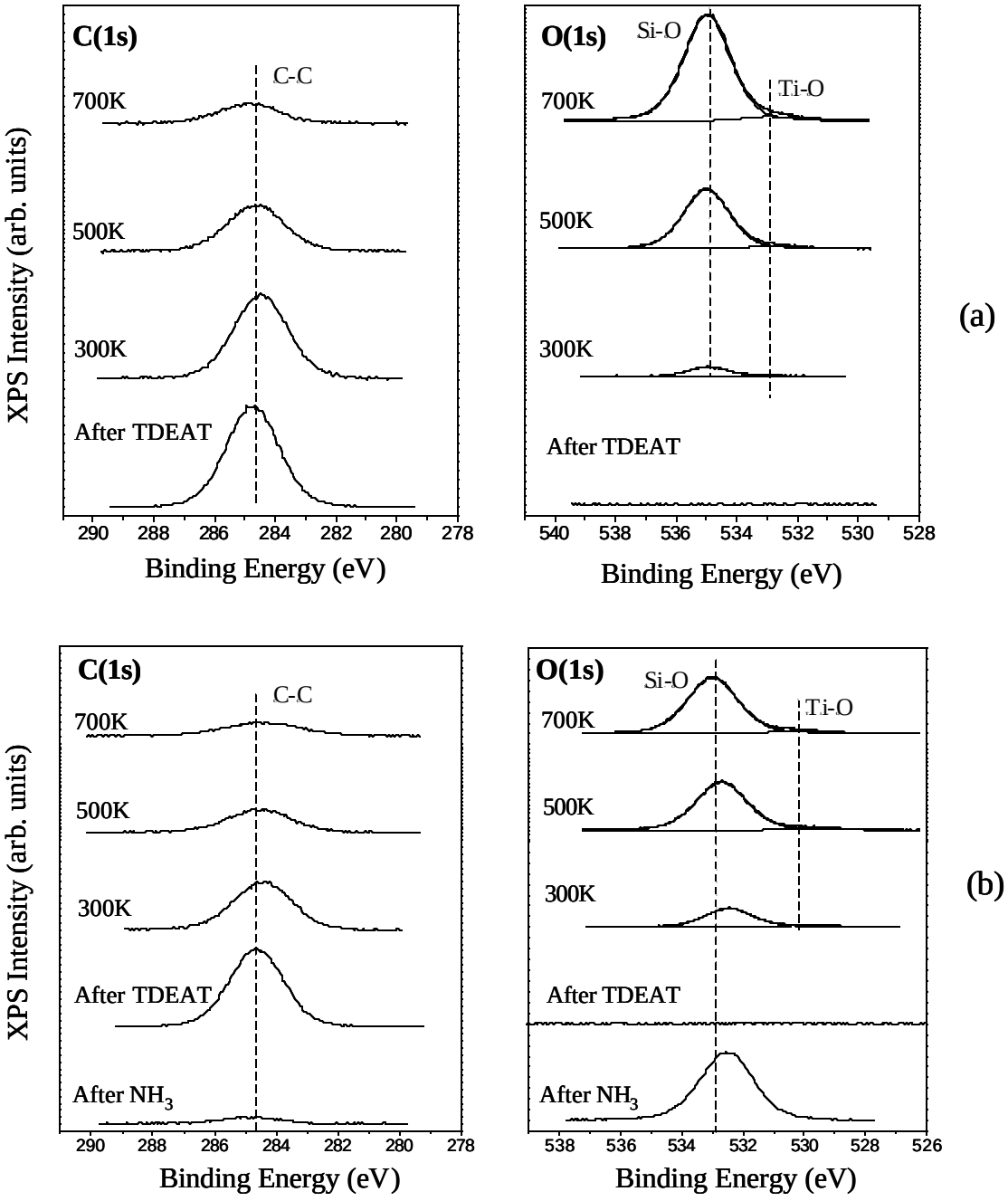

Fig.4.6 C(1s) and O(1s) XPS spectra for 3 L of TDEAT adsorbed on low *k*-2 surface at 120 K and annealed to higher temperatures. (a)TDEAT only (b) in the presence of 6 L NH_3

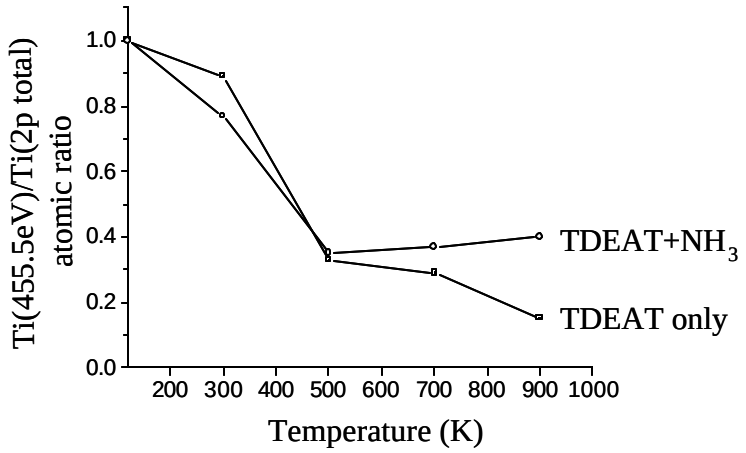

Fig. 4.7 Ti(455.5 eV)/Ti(2p total) XPS intensity ratios for 3 L of TDEAT adsorbed on low *k*-2 surface as a function of annealing temperature in the absence of NH_3 and in the presence of 6 L NH_3

4.3.2.3 Low k-3 (hydrocarbon)

TDEAT condensation on carbon-low *k* at 120 K followed by annealing results in very little Ti-N bonded species due to much less Ti surface coverage; at higher temperature, Ti(2p) spectrum shifted to higher binding energies characteristic of Ti-O bond formation(not shown). Simultaneously, the intensity of nitrogen decreased sharply. A new component appeared at a binding energy of 530.5 eV in the O(1s) spectrum(Fig.4.8), which is associated with the growth of Ti-O formation. Ti oxides become the dominant features even though oxygen concentration is low (2 at. % O) in the hydrocarbon films. The increase of O intensity is also due to the H_2O vapor and O_2 contamination from the reactor chamber during the low temperature condensation. This indicates that the O-containing impurity sites are the most active surface sites for interaction with TDEAT under these conditions. The C(1s) XPS spectrum has only one single peak at 284.5

eV, and exhibits negligible change upon exposure to TDEAT or subsequent annealing, indicating that Ti-C formation is not occurring. The presence of NH_3 does not have apparent effect on the results.

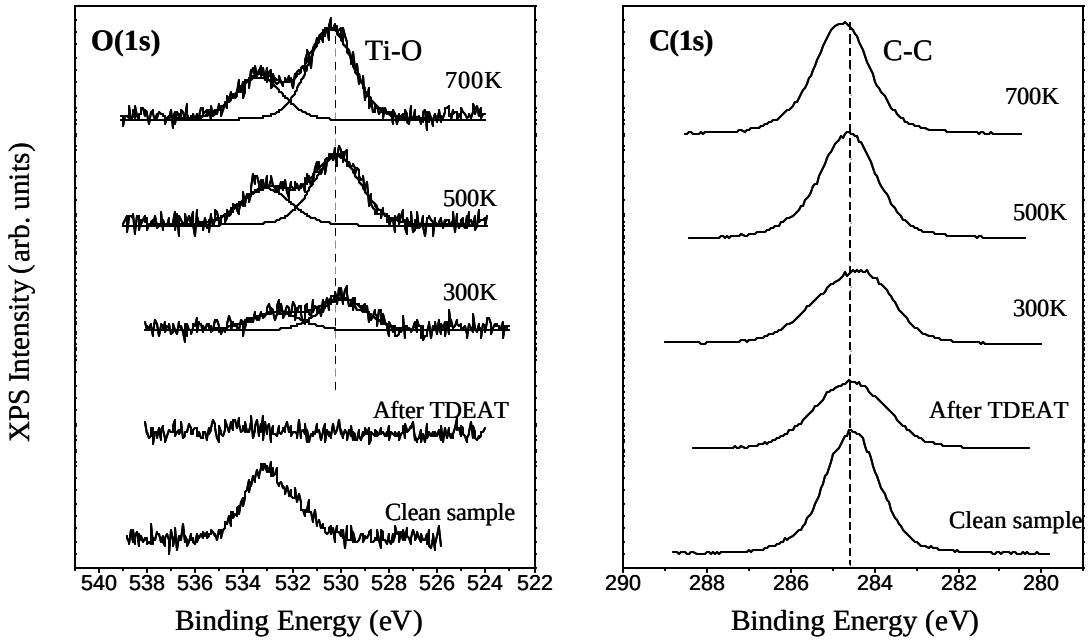

Fig. 4.8 O(1s) and C(1s) XPS spectra for TDEAT condensation on low *k*-3 substrate at 120 K, followed by high temperature annealing

4.3.3. Reactions of TDEAT with Low-*k* Substrates at Fixed Higher Temperature

Successive exposures of TDEAT were performed on a clean low-*k* surface at a constant temperature of 700K in UHV. The pressure of TDEAT was in the range of 5×10^{-8}~10^{-7} Torr. The progressive TDEAT exposures were carried out at a period of 10 min (30~60L) each cycle.

4.3.3.1 Low k-1($SiO_2C_{0.7}$)

Ti(2p), N(1s), C(1s), O(1s) and Si(2p) XPS spectra are displayed in Fig.4.9(a-e). The Ti(2p) spectrum shows the growth of the features at 454.5 eV and 455.5 eV, consistent with Ti-C (13)(454.7 eV) and Ti-N bond formation. Ti sub-oxides and oxides, evidenced by Ti features at

higher binding energies of 457.3 eV and 458.8 eV are also observed during TDEAT exposure. Ti-N bond formation is further evidenced by the appearance of the N(1s) peak at 396.7 eV. In the C(1s) spectrum, a new feature at binding energy of < 282 eV corresponding to carbide formation is observed as the TDEAT exposure increases. The absolute intensities of Si(2p) and O(1s) features decrease somewhat during TDEAT exposure, the intensity of the C(1s) peak (Fig.4.9c), however, increases. The relative changes of Ti(2p), N(1s),O(1s) and C(1s) intensities (normalized to Si(2p) intensity) is plotted as a function of TDEAT exposure (Fig.4.10). The data in figure 4.10 indicate an increase in relative Ti, N, and C core level intensities relative to those of O and Si. This is anomalous behavior, since the uniform formation of TiN on the surface would result in attenuation of C, O and Si core level intensity. Further, the higher kinetic energy of the Si(2p) vs. the O(1s) photoelectron implies a longer inelastic mean free path (and sampling depth) for the Si(2p) vs. O(1s) photoelectron. The growth of a uniform TiC or TiN film over the dielectric surface would lead to the preferential attenuation of O(1s) intensity, and a decrease in the O/Si core level intensity ratio, which is not observed. The data in figure 4.10 therefore indicate the formation of Ti-N or Ti-C film is not uniform; instead, the diffusion of partially dissociated TDEAT precursor ($Ti\text{-}NR_x$) into the film occurs. The calculated Ti(455.5 eV)/N(397 eV) atomic ratios are given in Table 4.2. The Ti/N ratio is around 0.5 as TDEAT exposure increases, which suggests the formation of TiN_2, a partially dissociated Ti-NR species, rather than the true nitride formation with a stoichiomistry of 1:1.

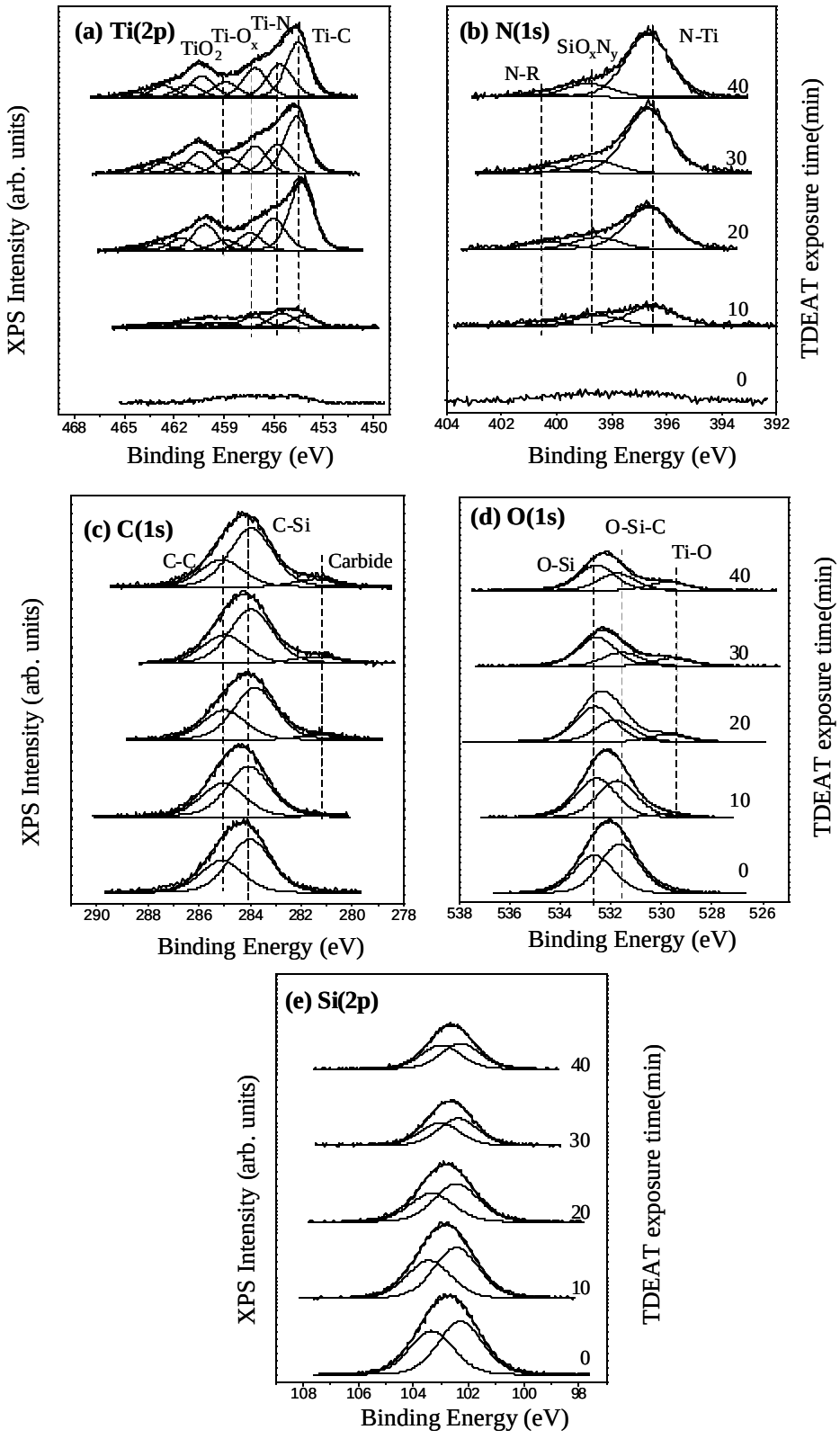

Fig. 4.9 XPS spectra for progressive exposures of TDEAT on low *k*-1 surface held at a constant temperature of 700 K. (Cumulative time of exposure at a background pressure of ~5x10^{-8} Torr) (a) Ti(2p); (b) N(1s); (c) C(1s);(d) O(1s);(e) Si(2p)

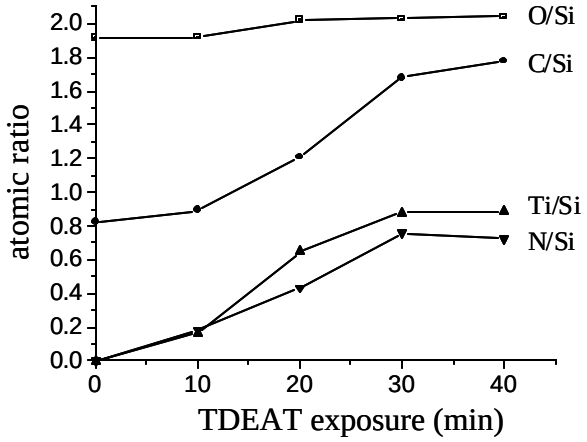

Fig. 4.10 Changes of relative Ti(2p), N(1s), C(1s) and O(1s) intensities (normalized to Si(2p) intensity) as a function of sequential TDEAT exposure($5x10^{-8}$ Torr) on low *k*-1 ($SiO_2C_{0.7}$) at 700K.

Table 4.2. Ti(455 eV)/N(397 eV) atomic ratios of sequential TDEAT dose ($5x10^{-8}$ Torr) on low*k*-1 surface in the absence of NH_3

TDEAT dose time (min)	Ti(455 eV)/N(397 eV)
10	0.53
20	0.57
30	0.36
40	0.41

XPS depth profiling by using Ar^+ (3 kV, 25 mA) was carried out after 40 min TDEAT exposure ($5x10^{-8}$ Torr at 700 K) on low *k*-1 sample. The thickness of the Ti overlayer film can be calibrated by measuring the attenuation of the Si(2p) substrate signal, according to

$$I = I_0 \exp(-d/\lambda) \qquad (4\text{-}2)$$

Where I and I_0 are the measured and initial absolute Si(2p) core level signal intensities, d is the thickness of the attenuating overlayer, and λ is the calculated electron inelastic mean free path (IMFP) for (in this case) a Si(2p) electron through Si:O:C –31.3 Å (14). Absolute, rather than

relative, Si(2p) intensities were measured. The thickness of the Ti overlayer estimated by this method was 21 Å. The estimated sputtering rate is around 1 Å-min^{-1} based on the previous experiments on standard samples. The variations of atomic concentration are plotted as a function of sputtering time in figure 4.11. The intensities of titanium and nitrogen decreased as the sputtering time increased and sputtered completely after 56 minutes deposition. The concentration of carbon decreased and the concentration of O and Si increased at the same time. After 56 minutes sputtering, the concentration of Si, O and C stay relatively constant throughout the film, which is indicative of Si:O:C substrate. The depth profile data reveals that there are excess amount of both Ti and N in the film, since the Ti overlayer thickness is only 21 Å, while at 42 min sputtering (~40 Å), there are still amount of Ti and N signal observed in the film. Therefore, it further verifies the existence of partially dissociated Ti-N bonded species which diffused into the porous Si:O:C low-*k* substrate.

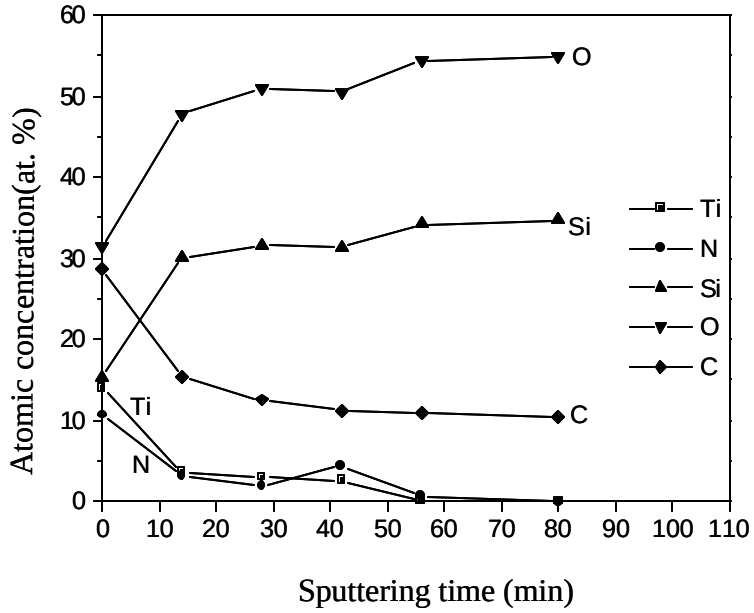

Fig.4.11 XPS depth profile of TDEAT(120 L)/low *k*-1

Experiments that were carried out in the presence of NH_3 (P_{NH3}~5 x10^{-8} Torr, total background pressure~2x10^{-7} Torr) produced almost identical results. Ti-N formation was observed, however, the amount of Ti-N phase was not enhanced by the addition of NH_3. The total amount of C(1s) increased due to the partially dissociated TDEAT precursor or Ti-alkyl, and carbide formation was evident (not shown).

4.3.3.2 Lowk -2($SiO_2C_{0.2}$)

Similar experiments were also performed on low *k*-2 substrates. Fig.4.12 (a-e) displays the XPS spectra of Ti(2p), N(1s), O(1s), C(1s) and Si(2p) after the successive TDEAT exposure at 700 K. The progressive dose of TDEAT results in the predominant product of TiO_x and TiO_2 formation, evident by the peaks at higher binding energies of 457.5 eV and 459 eV. The O(1s) core level presents the Ti-O peak at 531 eV. Very little Ti-N was formed. The C(1s) spectrum didn't show significant changes in both chemical environment and absolute intensity during the exposure, which means that the total intensity of carbon increased very slightly and no carbide formation was observed.

Experiments performed in the presence of NH_3 (~10^{-7} Torr) for TDEAT sequential exposure on low *k*-2 surface at 700 K results in the enhanced Ti-N formation (not shown), similar results as the reaction of TDEAT with SiO_2 sample presented in Chapter 3 (1). The experiment data therefore indicate that the properties of low *k*-2 sample, such as the surface topography, chemical composition and the products of interaction with TDEAT are very similar as SiO_2 sample.

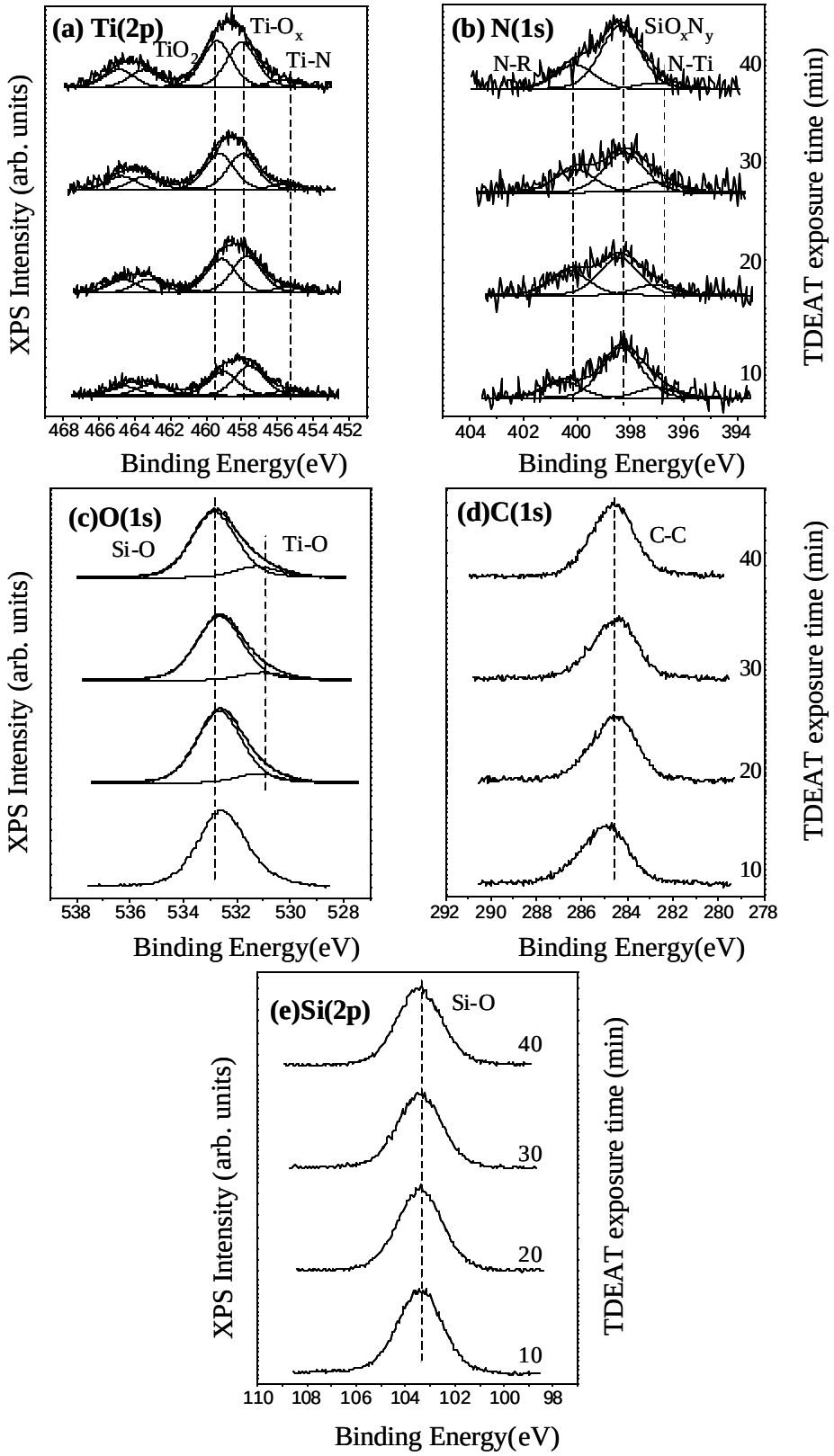

Fig. 4.12 XPS spectra for progressive exposures of TDEAT (~5x10^{-8} Torr) on low *k*-2 surface held at a constant temperature of 700 K (a) Ti(2p); (b) N(1s); (c) O(1s);(d) C(1s);(e) Si(2p)

4.3.3.3 low k-3 (carbon film)

Successive TDEAT exposure was carried on low *k*-3 substrate at the fixed temperature of 700 K and 900 K. No reactions occurred even after a long time period of TDEAT exposure. The presence of NH_3 didn't change the inertness of this carbon film. The surface modification was used to activate the interaction, such as sputtering the low *k* film with N_2 plasma. The low-*k* surface still proved to be inert, indicating a very low sticking coefficient of TDEAT on this inert carbon due to a lack of functional groups in order to initiate the TDEAT/low-*k* surface chemistry.

4.4. DISCUSSION

Low *k*-1 is a carbon-doped oxide with a composition of $Si_wC_xO_yH_z$. In this film, the silicon-oxygen network is occasionally interrupts, in a more or less homogeneous fashion, by the presence of organic, typically methyl (CH_3) groups. Incorporation of methyl or other groups has a significant effect on the key physical, thermal and chemical properties of the resulting film. The possible structure is presented as figure 4.13. `

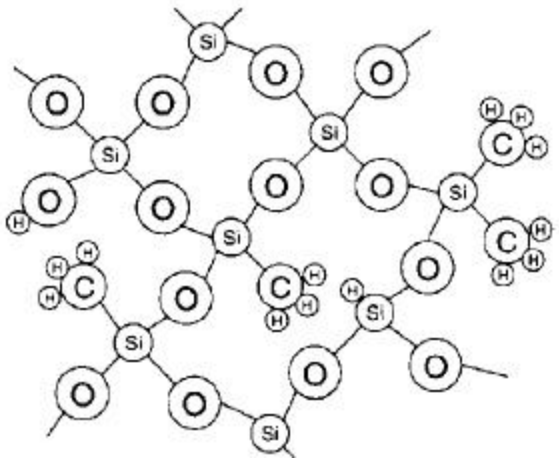

Fig. 4.13 Schematic structure of Si-O-C low-*k* dielectrics (15) (Reprinted with permission from Elsevier)

TDEAT condensation on low *k*-1 ($SiO_2C_{0.7}$) substrate at 120 K, followed by annealing to higher temperature, results in physisorbed precursor desorption from the surface. The amount of TiO_x and TiO_2 formed at higher temperature are negligible and the addition of NH_3 doesn't affect the interaction pathway. This is probably due to the porosity of low *k*-1 dielectric, allowing NH_3 to diffuse into the substrate instead of interaction with TDEAT. The roughness and porosity of this sample can be also observed from AFM image. Direct TDEAT interaction with this low-*k* at 700 K demonstrates undissociated or partly dissociated Ti-NR species trapped in the low-*k* matrix due to its high porosity. In addition, carbide formation is observed from C(1s) XPS spectra. The presence of NH_3 at ~10^{-7} Torr during the reaction has no effect on the film formation.

G. Bayer et al. (16) have studied atomic layer deposition (ALD) of TiN on a hydrogen silsesquioxane (HSQ) film with a pore diameter about 4–5 nm. TEM results show the TiN layer is discontinuous and the contrast of the image inside the film indicates the presence of metal inclusions. Similar observations were made on methyl silsesquioxane (MSQ) and hybrid dielectric materials with both ALD TiN and WCN, leading to the deposition inside dielectric films with an interconnected mesopore structure.

For low *k*-2 dielectric, the major products of the reaction of TDEAT at low temperature of 120 K followed by annealing up to 900 K in UHV are TiO_x and TiO_2 species. The presence of a co-adsorbed NH_3 multilayer at 120 K results in the enhancement of Ti-N formation upon annealing. Reaction of TDEAT with the low *k*-2 sample at 700 K yields very similar results compared to those of the interaction of TDEAT with SiO_2: Ti oxide/sub-oxide formation are dominated by Ti interaction with substrate oxygen sites in the absence of NH_3; Ti-N formation is significantly enhanced with the co-absorption of NH_3 (~10^{-7} Torr), no carbide is observed.

Condensation of TDEAT on low *k*-3 sample (hydrocarbon film) followed by annealing, results in preferential reaction at surface oxygen sites to form Ti oxide species. The interaction of TDEAT and carbon-film at high temperature of 500 K or 700 K, however, results in no observable reaction. The majority (carbon) sites on the film surface are highly unreactive towards TDEAT, in both the presence and absence of NH_3. Other surface treatments of the dielectric film must be implemented to activate TDEAT interaction. S. M. George et al. (17) reported poor nucleation of TiN ALD films on SiLK (polyphenylene polymer, Dow Chemical Company) (Fig. 4.14) due to a lack of functional groups to initiate the TiN surface chemistry. The TDMAT is expected to react with amino (NH) or hydroxyl (OH) surface groups to form a Ti-N or Ti-O chemical bond and displace dimethyl amine. The aromatic hydrocarbon polymer network of SiLK, however, is comprised of primarily phenyl groups and doesn't contain nitrogen. Treatments of the substrate prior to CVD barrier deposition facilitate with the nucleation and growth of the barriers. An O_2 plasma treatment, for example, may provide a strategy for depositing surface hydroxyl groups on the low-*k* polymer dielectric surface (16, 18).

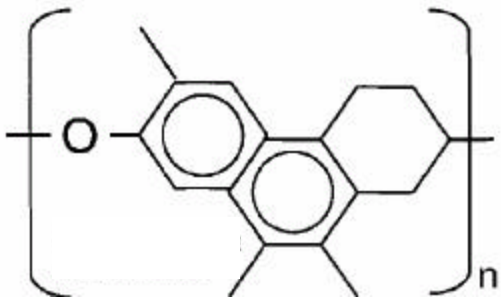

Fig. 4.14 Molecular structure of SiLK(15) (Reprinted with permission from Elsevier)

4.5 SUMMARY AND CONCLUSIONS

The interactions of TDEAT with SiO_2 and various low-k samples are summarized in figure 4.15. Obtaining lower dielectric constant requires the creation of porosity in the dielectric material. Porosity of dielectric materials, however, compromises chemical and mechanical properties. In porous dielectric films one deals not only with the availability of suitable functional groups at the surface but also with the penetration of the CVD precursors through the pore system. The trapped Ti-NR group from TDEAT precursor in porous low-k matrix and carbide formation will cause serious problems in the integration of TiN barrier layer/low-k dielectrics schemes. This stresses the need for pore sealing methods, which have to be integrated into the process flow. Pore sealing of a porous SiOC:H material by plasma has been reported recently (19). Sealing the porous low dielectric material may prevent the precursor diffusion, however, the properties of sealing materials need to be carefully considered since the addition of the new species may increase the substrate dielectric constant.

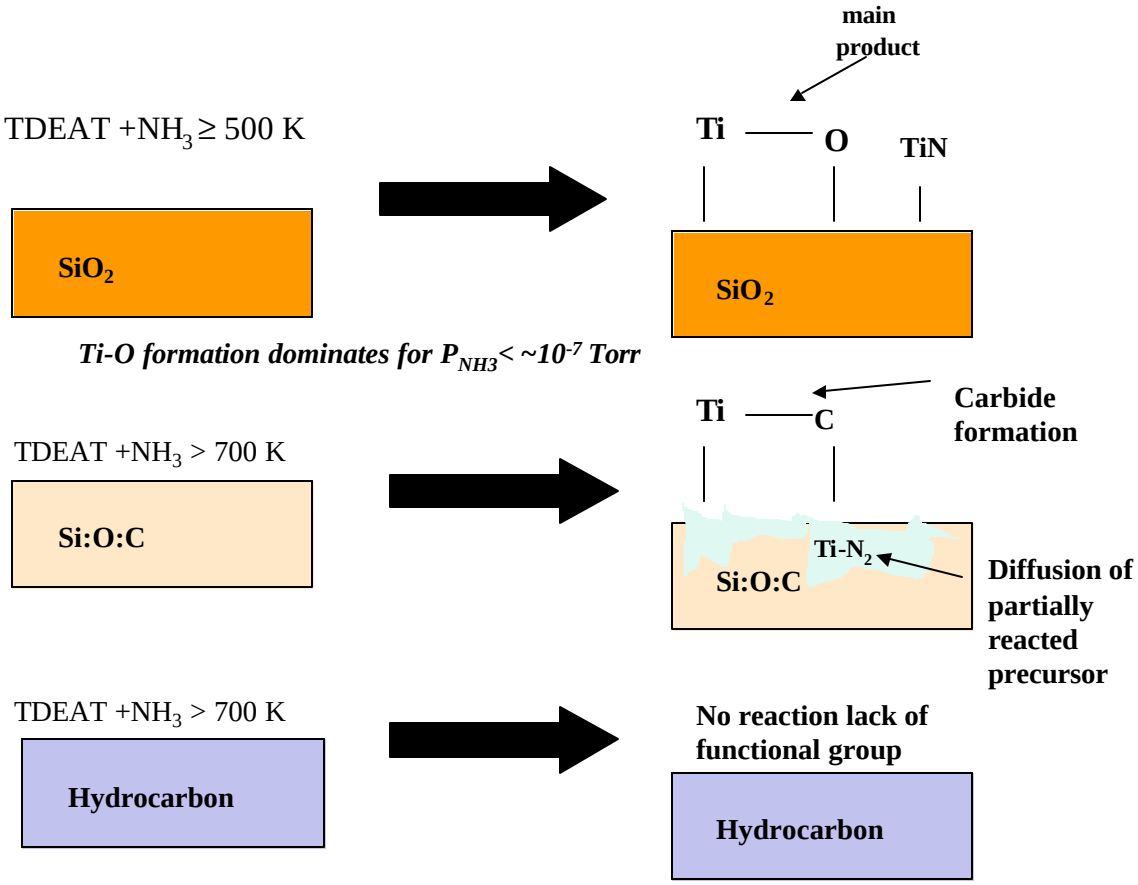

Fig. 4.15 Summary of TDEAT/NH_3 interactions with dielectrics

4.6 CHAPTER REFERENCES

(1) Tong, J.; Magtoto, N.; Kelber, J. *Appl. Surf. Sci.* **2003,** *220*, 203.

(2) Barr, T. L. *J. Vac. Sci. Technol A* **1991,** *9*, 1793.

(3) Bertoti, I.; Toth, A.; Mohai, M.; Revesz, M. *Acta Chimica Hungarica-Models in Chemistry* **1993,** *130*, 837.

(4) Fisher, I.; Kaplan, W. D.; Eizenberg, M.; Nault, M.; Weidman, T. *Mat. Res. Soc. Symp. Proc.* **2002,** *716*, B7.20.1.

(5) Contarini, S.; Howlett, S. P.; Rizzo, C.; Deangelis, B. A. *Appl. Surf. Sci.* **1991,** *51*, 177.

(6) Chourasia, A. R. *Surf. Sci. Spectra* **2001,** *8*, 45.

(7) Moulder, J. F.; Stickle, W. F.; Sobol, P. E.; Bomben, K. D. *Handbook of X-ray Photoelectron Spectroscopy*; Physical Electronics: Eden Prarie, 1992.

(8) Endle, J. P.; Sun, Y.-M.; White, J. M.; Ekerdt, J. G. *J. Vac. Sci. Technol. A* **1998,** *16*, 1262.

(9) Chourasia, A. R.; Chopra, D. R. *Thin Solid Films* **1995,** *266*, 298.

(10) Jouan, P.-Y.; Peignon, M.-C.; Cardinaud, C.; Lemperiere, G. *Appl. Surf. Sci.* **1993,** *68*, 595.

(11) Zhao, J.; Garza, E. G.; Lam, K.; Jones, C. M. *Appl. Surf. Sci.* **2000,** *158*, 246.

(12) Lu, G.; Bernasek, S. L.; Schwartz, J. *Surf. Sci.* **2000,** *458*, 80.

(13) Vandenbulcke, L.; Rats, D.; Barros, M. I. D.; Benoit, R.; Erre, R.; Andreazza, P. *Appl. Phys. Lett.* **1998,** *72*, 501.

(14) Zhao, X.; Magtoto, N. P.; Leavy, M.; Kelber, J. A. *Appl. Surf. Sci.* **2002,** *79*, 3479.

(15) Borst, C. L.; Korthuis, V.; Shinn, G. B.; Luttmer, J. D.; Gutmann, R. J.; Gill, W. N. *Thin Solid Films* **2001,** *385*, 281.

(16) Beyer, G.; Satta, A.; Schuhmacher, J.; Maex, K.; Besling, W.; Kilpela, O.; Sprey, H.; Tempel, T. *Microelectronic Engineering* **2002,** *64*.

(17) Elam, J. W.; Wilson, C. A.; Schuisky, M.; Sechrist, Z. A.; George, S. M. *J. Vac. Sci. Technol. B* **2003,** *21*, 1099.

(18) Satta, A.; Baklanov, M.; Richard, O.; Vantomme, A.; Bender, H.; Conard, T.; Maex, K. *Microelectronic Engineering* **2002,** *60*, 59.

(19) Travaly, Y.; Eykens, B.; L. Carbonell; Toan, L. Q.; Brongersma, S.; Conard, T. *Materials for Advanced Metallization Workshop* **2002**.

BIBLIOGRAPHY

"*http://www.webelements.com*."

Physical Electronics, PC-EXPLORER Software manuals, 1998.

The National Technology Roadmap for Semiconductors; Semiconductor Industry Association: San Jose, CA, 1999.

Atnassova, E.; Spassov, D. *Appl. Surf. Sci.* **1998,** *135,* 76.

Barr, T. L. *J. Vac. Sci. Technol. A* **1991,** *9*, 1793.

Baumer, M.; Freund, H.-J. *Progress in Surface Science* **1999,** *61*, 127.

Bekefi, G.; Barrett, A. H. *Electromagnetic Vibrations, Waves, and Radiation*; MIT Press: Cambridge, MA, 1987.

Bertoti, I.; Toth, A.; Mohai, M.; Revesz, M. *Acta Chimica Hungarica-Models in Chmistry* **1993,** *130.* 837.

Beyer, G.; Satta, A.; Schuhmacher, J.; Maex, K.; Besling, W.; Kilpela, O.; Sprey, H.; Tempel, T. *Microelectronic Engineering* **2002,** *64,* 233.

Bohr, M. T. *Solid State Technol* **1996,** *9,* 105.

Boo, J.-H.; Heo, C. H.; Cho, Y. K.; Han, J.-G. *J. Vac. Sci. Technol. A* **2000,** *18,* 1590.

Borst, C. L.; Korthuis, V.; Shinn, G. B.; Luttmer, J. D.; Gutmann, R. J.; Gill, W. N. *Thin Solid Films* **2001,** *385*, 281.

Briggs, D.; Seah, M. P. *Practical Surface Analysis*, 2nd ed.: Wiley, New York, 1990.

Cerio, F.; Drewery, J.; Huang, E.; Reynolds, G. *J. Vac. Sci. Technol. A* **1998,** *16*, 1863.

Chen, J. G.; Coloanmi, M. L.; Weinberg, W. H.; Yates, J. T. *Surf. Sci.* **1992,** *279*, 223.

Chen, L.; Ekstrom, B.; Kelber, J. *Mat. Res. Soc. Symp. Proc*. **1999**, 511, 287, Materials Research Society, San Francisco, CA, Spring 1999

Chen, L.; Magtoto, N.; Ekstrom, B.; Kelber, J. *Thin Solid Films* **2000,** *376*, 115.

Chourasia, A. R.; Chopra, D. R. *Thin Solid Films* **1995,** *266*, 298.

Chourasia, A. R. *Surf. Sci. Spec.* **2001,** *8*, 45.

Contarini, S.; Howlett, S. P.; Rizzo, C.; Deangelis, B. A. *Appl. Surf. Sci.* **1991,** *51*, 177.

Dubois, L. H. *Polyhedron* **1994,** *13*, 1329.

Ekstrom, B. M.; Lee, S.; Magtoto, N.; Kelber, J. A. *Appl. Surf. Sci.* **2001,** *171*, 275.

Elam, J. W.; Wilson, C. A.; Schuisky, M.; Sechrist, Z. A.; George, S. M. *J. Vac. Sci. Technol. B* **2003,** *21*, 1099.

Endle, J. P.; Sun, Y.-M.; White, J. M.; Ekerdt, J. G. *J. Vac. Sci. Technol. A* **1998,** *16*, 1262.

Faupel, F. *Phys. Stat. Sol. (a)* **1992,** *134*, 9.

Fisher, I.; Kaplan, W. D.; Eizenberg, M.; Nault, M.; Weidman, T. *Mat. Res. Soc. Symp. Proc.* **2002,** *716*, B7.20.1.

Fix, R. M.; Gorden, R. G.; Hoffman, D. M. *Chem. Mater.* **1990,** *2*, 235.

Garza, M.; Magtoto, N. P.; Kelber, J. A. *Surf. Sci.* **2002,** *519*, 259.

Grill, A. *Diamond and Related Materials* **2001,** *10*, 234.

Guimon, C.; Gonbeau, D.; Guillouzo, G. P.; Dugne, O.; Guette, A.; Naslain, R.; Lahaye, M. *Surf. Interface Anal.* **1990,** *16*, 440.

Hedge, R. I.; Fiordalice, R. W.; Travis, E. O.; Tobin, P. J. *J. Vac. Sci. Technol. B* **1993,** *11*, 1287.

Holloway, K.; Fryer, P. M. *Appl.Phys.Lett.* **1990,** *57*, 1736.

Jeng, S.-P.; Havemann, R.; Chang, M. *Mater, Res. Soc. Symp. Proc.* 1994, 337, 25.Material Research Society, Pittsburgh, 1994

Jouan, P.-Y.; Peignon, M.-C.; Cardinaud, C.; Lemperiere, G. *Appl. Surf. Sci.* **1993,** *68*, 595.

Kaloyeros, A. E.; Eisenbraun, E. *Annu. Rev. Mater. Sci.* **2000,** *30*, 363.

Kerr, J. A. *CRC Handbook of Chemistry and Physics 1999-2000: A Ready-Reference Book of Chemical and Physical Data (CRC Handbook of Chemistry and Physics)*, 81st ed.; CRC Press: Boca Raton, Florida, 2000.

Kim, K. S.; Jang, Y. C.; Kim, H. J.; Quan, Y.-C.; Choi, J.; Jung, D.; Lee, N.-E. *Thin Solid Films* **2000,** *377-378*, 122.

Lakshminarayanan, S.; Steigerwald, J.; Price, D. T.; Bourgwois, M.; Chow, T. P.; Gutman, R. J.; Murarka, S. P. *IEEE Electr. Dev. Lett.* **1994,** *15*, 307.

Latt, K. M.; Lee, Y. K.; Osipowicz, T.; Park, H. S. *Materials Science & Engineering B* **2002,** *94*.

Lee, W. W.; Ho, P. *MRS Bulletin* **1997,** *22*, 19.

Lee, Y. K.; Latt, K. M.; JaeHyung, K.; Osipowicz, T.; K.Lee *Mater. Sci. Eng.* **1999,** *B68*, 99.

Li, J.; Mayer, J. W. *MRS Bulletin* **1993,** *18*, 52.

Li, S.; Dong, Z. L.; Latt, K. M.; Park, H. S.; White, T. *Appl. Phys. Lett* **2002,** *80*, 2296.

Lu, G.; Bernasek, S. L.; Schwartz, J. *Surf. Sci.* **2000,** *458*, 80.

Maier, G. *Prog. Polym. Sci.* **2001,** *26*, 3.

Miller, S.; Berning, G. L. P.; Plank, H.; Roth, J. *J. Vac. Sci. Technol. A* **1997,** *15*, 2029.

Morgen, M.; Ryan, E. T.; Zhao, J.-H.; Hu, C.; Cho, T.; Ho, P. S. *Annu. Rev. Mater. Sci.* **2000,** *30*, 645.

Moulder, J. F.; Stickle, W. F.; Sobol, P. E.; Bomben, K. D. *Handbook of X-ray Photoelectron Spectroscopy*; Physical Electronics, Inc.: Eden Prairie, Minnesota, 1995.

Murauka, S. P. *Metallization: Theory and Practice for VLSI and ULSI*; Butterworth-Heinemann: Boston, 1993.

Murarka, S. P. *Materials Science and Engineering* **1997,** R19, 87.

Nefedov, V. I.; Firsov, M. N.; Shaplygin, I. S. *J. Electron Spectrosc. Relat. Phenom.* **1982,** *26*, 65.

Nicolet, M.-A. *Thin Solid Films* **1978,** *52*, 415.

Osiceanu, P. *Revue Roumatine de Chimie* **2002,** *47*, 521.

Ottaviani, G. *Thin Solid Films* **1986,** *140*, 3.

Peters, L. *Semiconductor International* **1998**.

Peto, G.; Zsoldos, E.; Guczi, L.; Schay, Z. *Solid State Commun.* **1986,** *57*, 817.

Pierson, H. O. *Handbook of Refractory Carbides and Nitrides*; Noyes/William Andrew Publishing: NY, 1996.

Powell, C. J.; Jablonski, A.; Tilinin, I. S.; Tanuma, S.; Penn, D. R. *J. Electr. Spectrosc. Relat. Phenom.* **1999,** *98-99*, 1.

Quirk, M.; Serda, J. *Semiconductor Manufacturing Technology*; Prentice-Hall, Inc.: Upper Saddle River, New Jersey; Columbus, Ohio, 2001.

Ramqvist, L.; Hamrin, K.; Johansson, G. *J. Phys. Chem. Solids.* **1970,** *31*, 2669.

Rats, D.; Vandenbulcke, L.; Herbin, R.; Benoit, R.; Erre, R.; Serin, V.; Sevely, J. *Thin Solid Films* **1995,** *270*, 177.

Riviere, J. C.; Myhra, S. *Handbook of Surface and Interface Analysis: Methods for Problem-Solving*; Marcel Dekker: New York, 1998.

Ruhl, G.; Rehmet, R.; Knizova, M.; Merica, R.; Vepek, S. *Chem. Mater.* **1996,** *8*, 2712.

Satta, A.; Baklanov, M.; Richard, O.; Vantomme, A.; Bender, H.; Conard, T.; Maex, K. *Microelectronic Engineering* **2002,** *60*, 59.

Seah, M. P. In *Auger and X-ray Photoelectron Spectroscopy*; Briggs, D., Seah, M. P., Eds.: New York, 1990; Vol. 1, pp 201.

Shacham-Diamand, Y. *AMC 2000* Tutorial

Shepherd, K.; Kelber, J. *Appl. Surf. Sci.* **1999,** *151*, 287.

Sherwood, P. M. A. *J. Vac. Sci. Technol. A* **1995,** *14*, 1424.

Shirley, D. A. *Phys. Rev.* **1972,** *B 5*, 4709.

Siegbahn, K.; Nording, C. N.; Fahlman, A.; Nordberg, R.; Hamrin, K.; Hedman, J.; Johansson, G.; Bermark, T.; Karlsson, S. E.; Lindgren, I.; Linberg, B. *ESCA: Atomic, Molecular and Solid State Structure Studied by Means of Electron Spectroscopy*; Almqvist and Wilksells: Uppsala, 1967.

Simpson, J. O.; St.Clair, A. K. *Thin Solid Films* **1997,** *308-309*, 480.

Slaughter, J. M.; Weber, W.; Guntherodt, G.; Falco, C. M. *MRS Bulletin* **1992,** *December*, 39.

Sprenger, D.; Bach, H.; Meisel, W.; Gutlich, P. *J. Non-cryst. Solids* **1990,** *126*, 111.

Stavrev, M.; Fischer, D.; Preub, A.; Wenzel, C.; Mattern, N. *Microelectronic Eng.* **1997,** *33*, 269.

Subramanian, P. R.; Laughlin, D. E. *Binary Alloy Phase Diagrams, Second Edition*; William W. Scott, Jr.: Materials Park, Ohio, 1990.

Thomas, J. H.; Hammer, L. H. *J. Electrochem. Soc.* **1989,** *136*, 2004.

Ting, C. H.; Seidel, T. E. *Mater. Res. Soc. Symp. Proc.* **1995,** *381*, 3.

Ting, C. Y.; Wittmer, M. *Thin Solid Films* **1982,** *96*, 327.

Tong, J.; Martini, D.; Magototo, N.; Pritchett, M.; Kelber, J. *Appl. Surf. Sci.* **2002,** *187*, 253.

Tong, J.; Martini, D.; Magtoto, N.; Kelber, J. *J. Vac. Sci. Technol. B* **2003,** *21(1)*, 293.

Tong, J.; Magtoto, N.; Kelber, J. *Appl. Surf. Sci.* **2003,** *220*, 203.

Torres, J. *Appl. Surf. Sci.* **1995,** *91*, 112.

Travaly, Y.; Eykens, B.; L. Carbonell; Toan, L. Q.; Brongersma, S.; Conard, T. *Materials for Advanced Metallization Workshop* **2002**.

Treichel, H.; Ruhl, G.; Ansmann, P.; Wurl, R.; Muller, C.; Dietlmeier, M. *Microelectronic Engineering* **1998,** *40*, 1.

Truong, C. M.; Chen, P. J.; Corneille, J. S.; Oh, W. S.; Goodman, D. W. *J. Phys. Chem.* **1995,** *99*, 8831.

Vandenbulcke, L.; Rats, D.; Barros, M. I. D.; Benoit, R.; Erre, R.; Andreazza, P. *Appl. Phys. Lett*. **1998,** *72*, 501.

Venables, J. A.; Spiller, G. D. T.; Hanbucken, M. *Rep. Prog. Phys.* **1984,** *47*, 399.

Wang, S. Q. *Mater. Res. Soc. Bulletin* **1994,** *19*, 30.

Wasa, K.; Hayakawa, S. *Handbook of Sputter Deposition Technology, Principles Technology and Applications*; Noyes Publications: Park Ridge, New Jersy, 1992.

Wittmer, M. *J. Vac. Sci. Technol.A* **1984,** *2*, 273.

Wu, Y.; Garfunkel, E.; Madey, T. E. *J. Vac. Sci. Technol.* **1996,** *A 14*, 1662.

Xiao, S. Q.; Tobe, R.; Suzuki, K.; Xu, X. B.; Sekiguchi, A.; Doi, H.; Okada, O.; Hosokawa, N. *Mat. Res. Soc. Sypm. Proc.* 2000, 295, Advanced Metallization Conference, Orlando, FL, September 28-30, 1999

Yin, K.-M.; Chang, L.; Chen, F.-R.; Kai, J.-J.; Chiang, C.-C. *Thin Solid Films* **2001,** *388*, 27.

Yokoyama, N.; Hinode, K.; Homma, Y. *J. Electrochem. Soc.* **1991,** *138*, 190.

Yun, J.-Y.; Rhee, S.-W. *Thin Solid Films* **1998,** *312*, 24.

Yun, J.-Y.; Park, M.-Y.; Rhee, S.-W. *J. Electrochem.Soc.* **1999,** *146*, 1804.

Zhao, J.; Garza, E. G.; Lam, K.; Jones, C. M. *Appl. Surf. Sci.* **2000,** *158*, 246.

Zhao, X.; Magtoto, N. P.; Leavy, M.; Kelber, J. A. *Thin Solid Films* **2002,** *415*, 308.